Mouse cardiac MRI

Mouse Cardiac MRI

Edwin Heijman

CIP-DATA LIBRARY EINDHOVEN UNIVERSITY OF TECHNOLOGY

Heijman, Edwin

Mouse Cardiac MRI / by Edwin Heijman.
- Eindhoven : Eindhoven University of Technology, 2008. -
Proefschrift. - ISBN 978-90-386-1429-8
NUR 954

Trefwoorden:
muizenhart / MRI / retrospectieve triggering en gating / MR tagging / SSFP
Subject headings:
mouse heart / magnetic resonance imaging / MR tagging / retrospective triggering and gating / steady state free precession

Cover design: Edwin Heijman
Printed by Gildeprint B.V., Enschede, The Netherlands

Mouse Cardiac MRI

PROEFSCHRIFT

ter verkrijging van de graad van doctor aan de
Technische Universiteit Eindhoven, op gezag van
de Rector Magnificus, prof.dr.ir. C.J. van Duijn,
voor een commissie aangewezen door het College
voor Promoties in het openbaar te verdedigen op
dinsdag 11 november 2008 om 16.00 uur

door

Edwin Heijman

geboren te Tegelen

Dit proefschrift is goedgekeurd door de promotor:

prof. dr. K. Nicolay

Copromotor:

dr. ir. G.J. Strijkers

The work described in this thesis has been carried out in the Biomedical NMR group at Eindhoven University of Technology, Department of Biomedical Engineering.

Contents

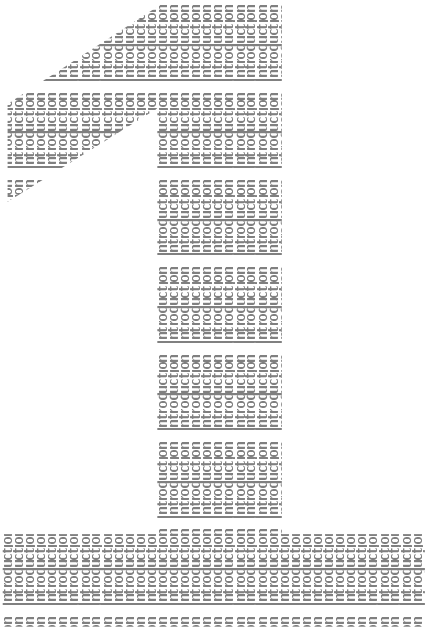

Introduction

The cardiovascular system

The heart is a vital organ for vertebrates like fish, amphibians, reptiles, birds and mammals. The amount of diffusive oxygen transport through the skin or fur is too low to fulfil the oxygen need of cells inside the body. To increase the transport and create a well controllable distribution of oxygen throughout the body, all of these large animals have a cardiovascular system. This closed system consists of blood, vessels and a heart. The heart is the pump for circulating the blood through the vessels. The oxygen is taken up by the blood in lung(s) or gills (fish) from the surrounding air or water.
The human cardiovascular system has three blood circulations; 1) the systemic circulation: transporting the blood from the heart through the whole body and back, 2) the pulmonary circulation: transporting the blood from the heart through the lungs and back to the heart and 3) the coronary circulation: perfusing the heart with oxygenated blood directly from the aorta towards the right atrium. The three circulations as well as the main components of the cardiovascular system are schematically drawn in Figure 1.1.
The systemic and pulmonary circulations are complementary. The blood in the systemic circulation supplies oxygen to the tissue whereas the blood in the pulmonary circulation receives oxygen in both lungs. Both circulations consist of arteries, capillaries and veins, which transport the blood from the high pressure to the low pressure side of the system. The oxygen saturated blood within the systemic circulation is transported from the heart through the arteries towards the capillaries where the blood supplies the surroundings cells with oxygen and takes up the carbon dioxide that is produced by oxidative metabolism. The blood is then further collected by the veins and transported back to the heart. Within the pulmonary circulation the blood is pumped from the heart via the pulmonary artery towards the capillaries of the lungs where it is saturated with oxygen. The oxygen saturated blood flows via the pulmonary veins back to the heart. The function of the heart is to create a pressure gradient between the aorta or pulmonary artery, and the vena cava or pulmonary vein of the systemic and pulmonary circulation, respectively. To do this the heart is divided up in two parts: left and right (within the patients reference frame) to generate two different pressure values in the aorta and pulmonary artery. The pressure within the aorta is higher, because the systemic circulation is longer and larger compared to the pulmonary circulation which only contains the lungs. The left and right part of the heart each consist of an atrium and a ventricle. The function of the atrium is to collect the continuous flow of blood and store it for a short period during the contraction. The atria contract when the ventricles are relaxing enabling a quick filling of the ventricles. The left ventricle pushes the blood into the aorta (systemic circulation), while the right ventricle does the same for the pulmonary artery (pulmonary circulation). Furthermore the heart connects the systemic circulation with the pulmonary circulation and visa versa. This implies that the left atrium receives the blood from the pulmonary circulation and

the right atrium from the systemic circulation. In atria as well as ventricles there are pressure changes during the pump cycle. Heart valves are preventing the flow of blood from the ventricle towards the atria and from the arteries to the ventricles when the pressure between atria and ventricles and, ventricles and arteries becomes negative. These valves are very important to increase the pump efficiency.
The heart is essentially one big muscle. The muscle tissue is responsible for the contraction of the atria and ventricles. When the atrial and ventricular contractions are well coordinated the blood can be pumped very efficiently towards ventricles or circulations. This coordination of contraction is caused by an electric pulse (action potential) which is traveling through the heart muscle from the atria to both ventricles. This electric pulse depolarizes muscle cells and opens Ca^{2+} ion channels within the sarcoplasmic reticulum (a structure within the heart muscle cell). After excitation Ca^{2+}-ions are released from the sarcoplasmic reticulum towards myofibrils within the heart muscle cell. These myofibrils are a chain of sarcomeres which are containing actin and myosin filaments. The Ca^{2+}-ions promote the interaction between an actin and a myosin filament. The coupling between the actin and myosin filaments creates a force and while these filaments can slide along each other the myofibrils contract the whole muscle cell. The electric pulse is powerful enough to be measured outside the human body using high resistance voltage amplifiers. This measurement technique is called electrocardiography (ECG) [1]. With the ECG the different heart phases can be discriminated. The measured potential is proportional to the number of depolarizing muscle cells; depolarization of the ventricles as well as the repolarization of the ventricles are very dominant. The cardiac cycle is defined by the state of the ventricles. The systolic heart phase is defined as the period of ventricle contraction when blood is pumped into the aorta or the pulmonary artery. The period during ventricular relaxation in which the ventricles are filled with blood from the atria is defined as the diastolic heart phase. By detecting the depolarization of the ventricles within the ECG signal the start of the systolic heart phase can be identified. Other cardiac electric activities can also be seen within the ECG. More details can be found in Ref. [2].

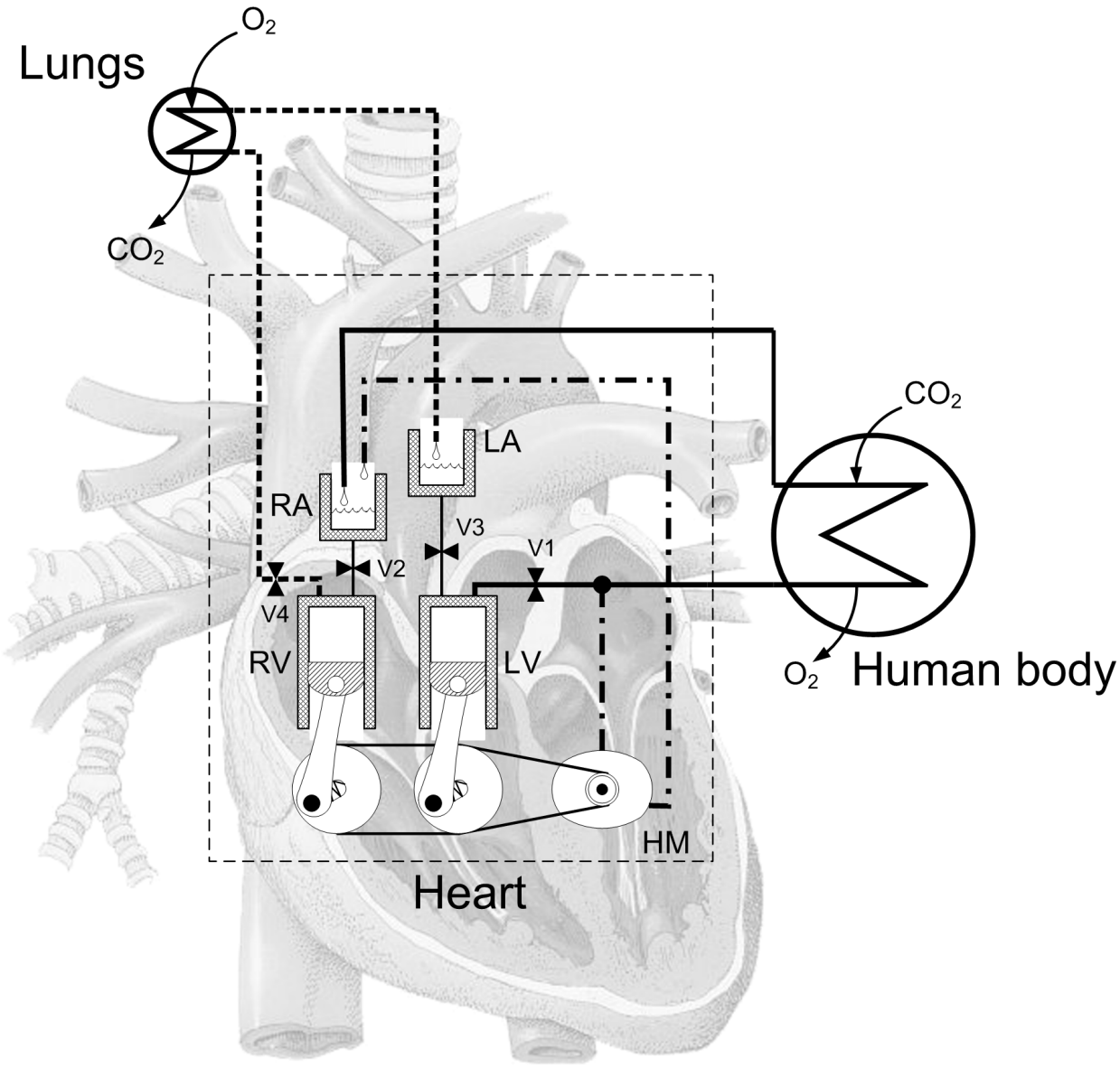

Figure 1.1: Schematical representation of the three main components of the human cardiovascular system (capillaries in the lungs, the heart and capillaries in the human body) and the three circulations: the systemic circulation (solid), the pulmonary circulation (striped), coronary circulation (dotted striped). LV: left ventricles, RV: right ventricle, LA: left atrium, RA: right atrium, HM: heart muscle, V1: Aorta valve, V2: Tricuspid valve, V3: Mitral valve, V4: Pulmonary valve.

The diseased heart

Cardiovascular diseases such as atherosclerosis, stroke and heart failure are one of the leading causes of death in The Netherlands as well as in Europe. In The Netherlands all cardiovascular pathologies showed a declining trend starting at the beginning of the 1990's [3]. Although cardiovascular mortality is declining in the Netherlands the research area of heart failure remains important. This declining trend in mortalitity caused by heart failure in the Netherlands was not consistent with the rest of Europe (data not shown from http://ec.europa.eu/eurostat).

A number of diseases lie at the basis of cardiovascular diseases *e.g.* hypertension [4], diabetes [5] and inflammations [6]. Especially, the number of diabetic patients will increase in future due to the increase of the average age and obesity in the world [7]. This probably will lead to an increase in the number of patients with a heart disease.

Cardiac failure is a symptomatic condition, in which the heart is no longer capable of pumping enough blood through the cardiovascular system. Cardiac failure will directly lead to death when no interventions are undertaken. Different pathologies can lead to cardiac failure. One of them is ischemic heart disease which is responsible for almost 11% of the total mortality in 2005 in the Netherlands. The ischemic heart disease can be fatal in the acute phase or lead to other pathologies like hypertrophy, myocardial wall dilatation or conduction problems like re-entry.

During an ischemic heart disease part of the heart is temporarily or permanently deprived from blood (ischemia). This leads to tissue necrosis or tissue injury of the myocardial wall (the infarct area). A thrombus is often the underlying cause of obstruction of the blood supply to the myocardium by blockage of one of the coronary arteries. Immediately after the start of ischemia a cascade of processes is started in an attempt to maintain the function of the heart. When the acute phase of the cardiac ischemia is not fatal, the ischemic region enters a process of wound healing that roughly can be divided into four phases: 1) cardiomyocyte death, 2) inflammatory response, 3) granulation formation and 4) final phase [8, 9].

The degree and extent of myocardial injury is a strong predictor for patient survival chance. Interventions that reduce the extent of injury can significantly improve the prognosis after a myocardial infarction [10]. A logical step is to reopen the coronary artery removing the ischemia and reducing the infarct size (percutaneous angioplasty). Although this therapy is successful in restoring the blood flow to the previously ischemic myocardium, reperfusion induces a new complex cascade of events that results in extra myocyte damage [11]. The beneficial effect of therapy diminishes also when the period of ischemia was longer. Animal studies showed that when the ischemic period is about 2 hours or more, the infarction size is comparable to that resulting from permanent occlusion [12].

The heart adapts its geometry and function to maintain sufficient cardiac output during and after the cardiac wound healing process. This adaptation is often referred to as remodeling. In humans two remodeling phases can be distinguished: the early phase within 3 days after occlusion and the late phase after 3 days. The early phase involves the expansion of the infarct zone, which may result in early ventricular dilatation or rupture of the infarcted ventricular zone. Ventricle dilatation initiates increased wall stress in the infarcted zone. This can be explained by the Frank-Starling mechanism. The left ventricle volume increases due to the wall dilatation. This leads to a larger force of contraction (higher systolic pressure) and consequently a larger amount of blood that is pumped into the aorta [2]. The increased pressure stretches the infarcted zone more and wall dilatation will increase with all its consequences. Late remodelling involves the left ventricle globally and is associated with time-dependent dilatation, distortion of the ventricular shape and hypertrophy. The hypertrophy is triggered by the increased contraction force caused by the dilatation. This will increase the wall stress in the remote zone. Hypertrophy itself may also lead to the loss of contractile function. The heart becomes more rigid, which induces even more wall stress and more hypertrophy. This can continue until the heart becomes so rigid that it can no longer supply itself with enough blood.
Both dilatation and hypertrophy are geometrically based. The heart is also depending on a synchronized contraction which is steered by an action potential through the heart. The conduction velocity and action potential are different in damaged myocardial tissue and healthy myocardial tissue [13]. The infarcted zone can cause arrhythmias initiated by re-entry or automaticity [14]. Both can lead to repeated uncontrolled contractions of the left ventricle wall (fibrillation). Ventricular fibrillation stops the coordinated contraction of the ventricles and immediately reduces the cardiac output.

Mouse

Humans and mice are both mammalians, but obviously quite distinct in their appearance. The organisation of the cardiovascular system, however, as described in the section 'The cardiovascular system', is almost equal between mice and men. The hearts of men and mice are also similar anatomically and in their function [15]. As an example, Henson *et al.* [16] found a similarity between mouse and human hearts in the left ventricular torsion measured with MRI. The twist angle between apex and base was different, but when torsion was normalized to left ventricular length the values were 1.9 ± 0.2 °/cm and 2.7 ± 2.3 °/cm for the human heart and mouse heart, respectively. Zhou *et al.* found similar twist angles between mouse and man ($\approx 8^\circ$ vs. $\approx 10^\circ$) [17], which was confirmed by Liu *et al.* [18].
The phases of cardiac wound healing are comparable between human and mouse, but the

process of cardiac wound healing is slower in humans than in mice. The coronary architecture variations are much bigger in humans compared to mice and therefore a larger variation in size and location of the ischemic area exists in humans. Therefore, a wider dispersion in the wound healing of the human heart is found, whereas in mice the size and transmurality of the ischemic area are more standardized [9]. On the cellular level several differences can be found. As an example the cross sectional area of the myocytes in humans is larger than in mouse hearts, whereas the capillary density is higher in mice compared to a human heart [19, 20]. Also a different composition of the sarcometric protein in the ventricles was found between mice and man [21, 22]. Humans have a high level of β-myosin heavy chain isoform, whereas mice have a high level of the α-myosin heavy chain isoform compared to the total myofibrillar myosin protein in the ventricles. According to Liu *et al.* [18] this could lead to different mechanical behavior of the myocardium.

Mouse cardiac MRI technology

Magnetic Resonance Imaging is based on the magnetic moment of hydrogen atoms. Since the human body contains a large amount of water, this technique is extremely good at imaging water rich soft tissue. Contrast can be controlled by the so called sequence parameters. The specific tissue relaxation times (defined as T_1 (spin-lattice relaxation time) and T_2 (spin-spin relaxation time)) and local water concentration within the tissue create contrast between and within organs and tissues in the MR image. This is the reason why MRI excells in imaging the anatomy of the human body.

Non-invasive imaging of the anatomy or physiology of the mouse becomes more important due to three different developments in science and society. First the genome of the mouse is well-characterized [23] and genetical engineering of mice is possible because of the stable germline transmission of gene mutations. The short period of gestation as well as rapid sexual maturation make mice suitable for fast multiplication and development [24]. Due to new developments in gene technology the following scientific question becomes very important: "what is the relation between the genotype and the phenotype". Non-invasive imaging techniques can play a significant role to answer this question. Secondly, it is described by law in most Western countries that new medicines or medical interventions first have to be tested on animals before they can be used for or in humans. Mice are less costly in breeding and housing compared to other animals and thus very economic in testing new medicines or interventions. Finally, the influence of social organizations to reduce or even eliminate the need of animal experiments increases within several European countries.

MRI can comply with the above three questions or demands. Longitudinal studies can be

performed with MRI over a long period. An MRI scan is non-invasive and therefore it can play a vital role in reducing the total number of animal experiments. One of the biggest advantages of MRI is the versatility compared to other imaging modalities like X-ray, Computer Tomography (CT), ultrasound, nuclear techniques like Single Photon Emission Computed Tomography (SPECT) and Positron Emission Tomography (PET), or optical imaging techniques. MRI does not need ionizing radiation or radio-active isotopes for generating high quality anatomical or functional images of the heart and MRI has a wide range of image scales from the anatomical to the functional level [25]. Disadvantages of MRI are its difficulties to image on the cellular or molecular level (see section '.. to Molecular Imaging').

The first results of a mouse cardiac MRI study were reported in 1997 by Siri *et al.* [26]. At that time scientists were not very optimistic about using MRI as a tool for imaging the mouse heart. James commented that this technique would not be widely used for murine studies in the near future [27] due to the hardware and software requirements for this relatively new imaging technique for small animals. Some researchers used a human MR scanner to study the mouse heart like Bryant and Franco, who used a 1.5T Philips Gyroscan NT whole body MR scanner [28–30]. It soon became clear that dedicated hardware like high field magnets and specialized gradient systems were required for high quality imaging of the mouse heart [31–33]. Especially the small dimension of a mouse heart (approximately 5 mm in diameter) and the high heart rate (up to 600 beats/min) require specialized high-end MRI systems with dedicated gradient and radiofrequency coils.

Studies at that time were already biased by the developments in human cardiac MRI. The main topics of the first human cardiac MRI studies were to examine the anatomy of the heart and find abnormalities in patient groups. Most mouse cardiac studies between 1997 and today were aimed to measure the global functional parameters of the heart. MRI methods for measuring global functional parameters of the human heart were already developed in the early 1990's [34, 35].

Measurements of global functional indices of the mouse heart have predominantly been used for two main applications. One of these applications was phenotyping genetically modified mice by comparing functional data with their littermates or wildtype controls [30, 30, 36, 37]. The second application concerned characterizing the diseased heart [10, 17, 38–40], sometimes combined with an intervention [41–47].

The group from Prof. Haase at the University of W*ü*rzburg in Germany was one of the pioneers in the area of mouse cardiac MRI and published important articles on global cardiac function in ageing mice [48] as well as on imaging of the coronary arteries of the mouse [49]. They also studied the effect of dobutamine stress on global functional parameters (Wiesmann *et al.* [50]). Dobutamine increases the inotropy of the heart without requiring an exercise [51]. This method was also successfully used by Williams *et*

al. [52] in vascular endothelial growth factor (VEGF) knockout mice showing that the lower capillary density in the hearts of these mice leads to changes in the global functional parameters when mechanically stressed.
A more direct approach in visualizing the inotropy increase of the mouse heart is to inject a $MnCl^2$-solution intravenously. Manganese-enhanced MRI is able to visualize the inotropy increase caused by dobutamine [53] by enhancing the myocardial wall on T_1-weighted scans. According to Hu *et al.* [40], the Mn^{2+}-ion enters the myocytes by the voltage-gated L-type calcium channels. They suggest that this technique could also be used in cardiovascular disease models for investigating the infarct size and tissue viability simultaneously.
Another way to determine local myocardial viability is to use a paramagnetic contrast agent based on the gadolinium ion [54]. This so called contrast-enhanced MRI (CE-MRI) of an infarcted mouse heart was first published by Yang *et al.* [41] from the University of Virginia Health System. These authors used a Gd-DTPA dose of 0.3-0.6 mmol/kg. To verify the location and the dimensions of the infarct a second MRI technique was used. Motion is commonly accepted as a discriminator of viable and non-viable tissue in the myocardial wall [55]. To track the motion in the myocardial wall different measurement techniques were already developed for humans. One of these techniques is MR Tagging where CINE images are made of tag lines of magnetization within the myocardial wall. Two techniques to prepare the tag lines of magnetization were compared by Wu *et al.* [56]. They showed that it was possible to make tag lines within the myocardial wall with a sinc modulated RF pulse train and compared it with a DANTE pulse train [57]. This study showed no analysis of these tag lines from which the strain vectors could be calculated in the mouse heart. A more common technique to make tag lines of magnetization is the Spatial Amplitude Modulation (SPAMM) [58]. With this tagging technique Epstein *et al.* [59] measured contractile dysfunction in adjacent and remote regions of infarcted mouse hearts on the basis of strain analysis. The results of the circumferential strain analysis were compared to CE-MRI using Gd-DTPA as a contrast agent. Zhou *et al.* [17] repeated this SPAMM measurement although they claimed that they were the first to use MR Tagging. Zhou *et al.* measured only healthy mice and the strain analysis was based on triangular elements, a procedure first published by Young *et al.* [60].
An alternative for motion tracking with MR tagging is the complementary displacement encoding with stimulated echoes (DENSE) technique published by Gilson *et al.* [61]. In DENSE, the positions of the pixels are phase encoded at the begin-systolic heart phase and read out at a later time point. This complementary DENSE technique combines the DENSE technique [62] with a suppression technique for decreasing the T_1 artefact [61]. Two echoes are generated, one with T_1 information and a second with the DENSE encoding. This technique was further developed in a multi-slice DENSE technique and tested on infarcted mouse heart by Gilson *et al.* [63]. The regional DENSE information was compared also with CE-MRI of infarcted mouse hearts [10]. Another MR technique for

motion mapping is phase contrast MRI which was applied to mouse hearts by Streif *et al.* [64]. Like DENSE the phase of the magnetization was used, but now the phase was velocity encoded.
The oxygen supply within the mouse heart can also be quantified by measuring the regional blood flow (or perfusion) in the myocardial wall. To increase the sensitivity for the local blood volume Wu *et al.* [65] used iron-oxide nano particles and measured with a T_2^* -weighted gradient echo sequence. With this method they could map the cyclic changes in regional blood volume inside the myocardial wall. Regional blood flow can be measured with the arterial spin labelling technique (ASL) [66]. ASL is based on the effect of T_1 change of the tissue as function of inflow of fresh or not excited blood. Kober *et al.* [67] developed a respiratory-gated spin labelling sequence for mice and evaluated the influence of different anaesthetics (ketamine/xylazine and isoflurane) on the perfusion within the myocardial wall. They showed that the myocardial blood flow is highly sensitive to the isoflurane concentration. Streif *et al.* [68] used the same spin labelling technique, but they tested their measuring protocol by administering the anaesthetic propofol intravenously.
Most research groups in mouse cardiac MRI have high field magnets of 7 Tesla or 9.4 Tesla with a horizontal bore. The consequence of higher field strengths and vertical position were studied by Schneider *et al.* [69] in a vertical bore 11.7 Tesla system. He compared global functional parameters between a 7T horizontal bore magnet and the vertical bore of 11.7 Tesla. No significant differences were found by the change in the position of the mouse and field strength in healthy and infarcted mouse hearts [70] compared to an older study with a comparable mouse group [32].
All mentioned developments are based on imaging the mouse heart. In the mid 80's localized Magnetic Resonance Spectroscopy (MRS) was developed to detect and quantify *in vivo* metabolites on the basis of their specific resonance frequencies. These NMR spectra are not only restricted to the ^{1}H nucleus but also other nuclei with a magnetic moment *e.g.* ^{31}P and ^{13}C [71] can be used. The localization can be made by a surface RF coil which has a small area of detection [72] or by Point RESolved Spectroscopy (PRESS) [73]. Schneider *et al.* [70] used the PRESS sequence and a black blood technique to measure ^{1}H spectra of the septum in creatine kinase deficient mice. Not only localized spectroscopy techniques were used, but also one dimensional and two dimensional spectroscopic imaging techniques were meanwhile developed to get better spatially defined spectra of a part or the whole myocardial wall. The group of Weiss at Johns Hopkins University used a 1 dimensional chemical shift imaging technique (1D-CSI) for measuring phosphocreatine and adenosine triphosphate levels in the myocardium [74, 75]. Two dimensional ^{31}P-spectroscopic imaging techniques (2D-CSI) were used by Flögel *et al.* [76] for measuring the spectra at different positions in the myocardium. This chemical shift imaging sequence was stretched to the limits for imaging the ^{13}Na density in the myocardial wall of a mouse in 3D by Neuberger *et al.* [77]. To compensate for the low measurement sensitivity and

short T_2 of ^{13}Na, these measurements were performed at a high magnetic field strength (17.6 Tesla) and required a long acquisition time of 1.5 hours (voxel size: 1x1x1 mm^3).
In vivo measurements are a challenge for MRI and MRS, but *ex vivo* measurements do also have interesting applications. As an example the visible mouse project [78] and imaging of mouse embryos *ex vivo* [69] make it possible to scan at very high resolutions for studying the morphology of the heart. It is also possible to make an MRI sequence sensitive for the diffusion of water molecules. The diffusion length that is probed with this technique is of the order of 10 to 100 μm, which makes it very hard to measure the water diffusion coefficient in the mouse heart *in vivo* due to compromising effects of the heart motion. When the diffusion is measured in at least 6 directions within the MR image together with a non-diffusion weighted MR image a tensor can be constructed in each pixel [79]. With this technique, called diffusion tensor imaging (DTI), a preferred diffusion direction can be derived from the local eigenspace analyses. The eigenvector with the highest eigenvalue corresponds to the muscle fiber direction. Jiang *et al.* [80] applied a 3D-DTI sequence to fixed mouse hearts to make preliminary reconstructions of the internal fiber structure of the mouse heart.

....To Molecular Imaging

MRI is excellent in imaging the anatomy or measuring the physiology of the heart [25], but is not able to give direct information on the cellular or molecular level *in vivo*. Developments in molecular biology generate a growing need for non-invasive imaging modalities that are able to detect sparse molecular epitopes *in vivo*. To visualize these biological markers, probes are developed that usually consist of three components. The first component is a ligand, which binds to the target with high affinity and specificity. A linker or carrier, the second component, connects the ligand to the third component, a label. The label is needed for detection and is specific for the imaging modality used. The probe should recognize the target with a high specificity [81] and should have favorable pharmacokinetic properties *in vivo* to make detection of low levels of biological markers possible [82].
For MRI, contrast agents are used as label for visualizing the targeted probes. Two major classes of contrast agents can be distinguished: super-paramagnetic contrast agents that generate strong T_2 contrast (often based on FeO nano-particles) and contrast agents based on gadolinium (Gd) chelates that increase the T_1 contrast in MR images [83]. These two major classes of contrast agents are already well established in different clinical applications. New developments are contrast agents based on fluorine [84, 85] and Chemical Exchange Saturation Transfer (CEST) [86, 87].
MRI provides a high spatial resolution for visualizing the distribution of contrast agents,

but has a limited detection sensitivity (in the order of 10-100 micromolar for Gd-based agents), compared to for example positron emission tomography and single-photon emission computed tomography, which can detect probes in the picomolar and nanomolar range, respectively [88]. There are two major options to improve the MRI detection sensitivity of Gd-based contrast agents. First, the number of Gd atoms in the probe can be strongly increased, *e.g.* by the use of paramagnetic liposomes [89]. Secondly, improvements can be made by the use of recently developed MR sequences, which allow a more sensitive detection of Gd-contrast agents [90].
The future of molecular imaging is probably already shown in the "Star Trek: The next generation" TV series. Within this TV series a holographic doctor treats patients with highly advanced microprobes which can detect and repair tissue (*e.g.* DNA) or kill specific viruses. But important is that he can visualize this therapeutic procedure and have possibilities to detect the problem and to decide fast on the therapeutic procedure needed. This view into the future becomes slowly reality. Already developments have started to search for different biological marker detection strategies for identifying diseases before symptoms become anatomically visual or to locally deliver medicines (referred to as microprobes in the Star Trek series).

This thesis

This thesis is the result of the PhD research project "Mouse Cardiac MRI". The goal of the project was to develop an advanced toolbox for measuring functional parameters of the mouse heart with a high field MRI scanner. Global functional parameters, *e.g.* the ejection fraction and cardiac output, are important indicators of the physiological condition of the heart.
However, before the different functional parameters could be determined several technical issues had to be solved. First, MRI is very sensitive to motion. To prevent motion artifacts, synchronization between the MR acquisitions and heart motion is required. The synchronization is normally performed by R-wave detection from the ECG. At that moment a trigger pulse is send to the MR equipment. Several cardiac cycles are required to acquire and reconstruct a MR image of the heart. These acquisitions can be done at a fixed delay after the trigger pulse. To capture the motion of the mouse heart in a time efficient manner, more acquisitions are taken within the cardiac cycle for reconstructing MR images of the different heart phases. The latter method is called CINE (cinematographic) MRI. Cardiac motion is not the only motion to deal with. The mouse heart is located between both lungs, which displace the heart during respiration. Two strategies to deal with these cardiac and respiratory motions were examined in this thesis: a) prospective ECG triggering, combined with a pause in the acquisition during the respi-

ration; b) discard the data acquired during the main respiration motion retrospectively and reconstruct MR images of different heart phases from the remaining data retrospectively, based on a navigator echo. The implications of measuring continuously with the retrospective method were compared with the discontinuous prospective method in Chapter 2. The second challenge is to deal with the time consuming manual segmentation of the myocardial wall of the mouse for the determination of global functional parameters from CINE MR images. In close cooperation with Pie Medical Imaging a study was performed to test an automatic segmentation algorithm as a replacement for the common manual segmentation. The results of this study are described in Chapter 3. In Chapter 4 smoothelin-B knockout mice are phenotyped, as a test for the robustness of the MRI technology for assessing mild functional changes in the cardiovascular system. The global functional parameters of the left ventricle were measured by prospective triggering and the elongation of the thoracic aorta with the retrospective navigator echo method. Local functional information of the myocardial wall is indispensable for studying differences between infarcted tissue and tissue from the remote zone (healthy tissue). Local motion is a good representation of the local function of the myocardial wall. In Chapter 5 a feasibility study is described of a common motion capturing technique developed for human cardiac MRI. As shown by Weissleder *et al.* [25] the image modalities currently used in hospitals and universities are not able to cover the whole spatial range from the anatomy to the molecular level. Due to this, hybrid systems are built (*e.g.* a MRI scanner with Positron Emission Tomography (PET) module) [91, 92] or multi-modality procedures are developed [93, 94] to combine the qualities of MRI at the anatomical level and the strength of PET at the molecular level. To judge the added value of the MRI-PET combination the two modalities were explored in a serial study. In Chapter 6, a comparison is made between global functional parameters (anatomical level) as determined by MRI and PET. Also a comparison was made between contrast enhanced MRI and PET for measuring infarct size (cellular/molecular level). MRI is relatively insensitive for contrast agents compared to a nuclear imaging modality like PET. Increased sensitivity is a hot topic in the development of imaging probes and detection sequences for molecular imaging with MRI. Chapter 7 describes an *in vitro* study of a fast imaging sequence which has a higher sensitivity for Gd-DTPA compared to a traditional sequence. The thesis ends with a general discussion on future perspectives and conclusions.

Comparison between prospective and retrospective triggering for mouse cardiac MRI

Edwin Heijman[1], Wolter de Graaf[1], Petra Niessen[2], Arno Nauerth[3], Guillaume van Eys[2], Larry de Graaf[1], Klaas Nicolay[1] and Gustav J. Strijkers[1]

[1] Biomedical NMR, Department of Biomedical Engineering, Eindhoven University of Technology, Eindhoven, The Netherlands

[2] Department of Molecular Genetics, Cardiovascular Research Institute Maastricht (CARIM), University of Maastricht, Maastricht, The Netherlands

[3] Bruker BioSpin MRI GmbH, Ettlingen, Germany

published: NMR Biomed. 2007 Jun;20(4):439-47.

Abstract

High resolution magnetic resonance imaging (MRI) has evolved into one of the major non invasive tools to study the healthy and diseased mouse heart. This study presents a Cartesian CINE MRI protocol based on a fast low-angle shot sequence with a navigator echo to generate cardiac triggering and respiratory gating signals retrospectively, making the use of ECG leads and respiratory motion sensors obsolete. MRI of the *in vivo* mouse heart using this sequence resulted in CINE images with no detectable cardiac and respiratory motion artifacts. The retrospective method allows for steady state imaging of the mouse heart, which is essential for quantitative contrast-enhanced MRI studies. A comparison was made between prospective and retrospective methods in terms of the signal-to-noise ratio, the contrast-to-noise ratio between blood and myocardial wall as well as global cardiac functional indices end-diastolic volume, end-systolic volume, stroke-volume and ejection fraction. The retrospective method resulted in almost constant left ventricle wall signal intensity throughout the cardiac cycle, at the expense of a decrease in the signal-to-noise ratio and the contrast-to-noise ratio between blood and myocardial wall as compared to the prospective method. Prospective and retrospective sequences yielded comparable global cardiac functional indices. The largest mean relative difference found was 8% for the end-systolic volume.

Introduction

Cardiac MR images without motion artifacts can only be accomplished by synchronizing the image sampling of the MRI scanner with the cardiac cycle (cardiac triggering) [35] and excluding or stopping the image sampling during the respiratory period (respiratory gating) [95]. Several solutions already exist for obtaining the cardiac triggering and respiratory gating signals for cardiac MRI of small laboratory animals, such as rats and mice. The conventional way to measure the triggering and gating signals is using respiratory and electrocardiogram (ECG) sensors [29, 31–33, 59, 69, 96]. The respiratory sensor is positioned on the chest of the animal to determine the respiratory motion and typically two ECG pads are connected to the paws or the tail to measure the ECG signal of the heart. Triggering pulses are derived from the ECG signal by a computer or a dedicated ECG monitoring system. Within these devices the respiratory gating pulses, which are based on the measured respiratory motion, can also be determined and used to suppress the cardiac trigger pulses during respiratory activity [97]. For human cardiac MRI breath holding is often used to prevent displacement of the heart during scanning [98]. This method, however, is not easily applicable to small rodents such as mice, because the anaesthetized animals are usually allowed to breath freely during the experiment. The measured ECG and respiratory signals can be used in two ways. Either the MRI scanner is directly triggered by the cardiac triggering pulses, the prospective way [99], or ECG and respiratory information are stored together with the MRI data, which are then used to sort and reconstruct the cardiac images after the experiment, the so-called list-mode or retrospective triggering method [100].

In addition, there is a convenient way to circumvent these ECG and respiratory motion measurements with sensors. Since any echo or free induction decay signal in an MRI sequence is sensitive to the heart and respiratory motion, which lies obviously at the basis of why synchronization between heart and respiratory motion and the MRI measurement is needed in the first place, time-dependent changes in these signals as a consequence of heart and respiratory motion can be used to generate cardiac triggering and respiratory gating signals in list-mode retrospectively from the MRI measurement itself. For this purpose, the acquisition of a separate navigator echo is incorporated in such a sequence, because the main image echo is used to reconstruct the MR images. This 'wireless' cardiac MRI was first introduced by Spraggins [101, 102] for human studies and recently found renewed interest for human applications [103, 104] as well as for small rodents [90, 105–107]. The retrospective 'wireless' method has some distinct advantages. It circumvents the need for ECG measurements, which are sometimes difficult at high magnetic fields in small rodents, especially in diseased animals [106]. Moreover, since the MRI sequence is not interrupted periodically during the breathing periods of the animal and at the end of every cardiac cycle, the sequence has the advantage of maintaining a steady-state longitudinal

magnetization throughout the cardiac cycle, which is essential for robust image contrast and quantitative studies with contrast agents.
In this chapter we describe a Cartesian CINE MRI sequence based on a fast low-angle shot (FLASH) sequence [108] with an extra navigator echo. Retrospective analyses of this navigator signal generated the cardiac triggering time points and respiratory gating windows, which were checked with the measured respiratory and ECG sensor signal. Using these time points and gating windows the image echo data were reconstructed to mouse cardiac CINE MRI images. A rigorous comparison was made between the prospective respiratory and ECG measurement and the retrospective methods. This comparison included the signal-to-noise ratio (SNR) behavior during the cardiac cycle; the contrast-to-noise ratio (CNR) between the blood and the myocardial wall of the left ventricle as well as several global heart indices: the end-diastolic volume (EDV), the end-systolic-volume (ESV), the ejection fraction (EF) and the stroke volume (SV). *In vitro* measurements were done as well to explain the SNR behavior of the prospective and retrospective methods throughout the cardiac cycle.

Theory

If there is any measurable transversal magnetization present every gradient pair, with a positive and a negative gradient field strength (G), generates a gradient echo if the condition

$$\int_{\zeta}^{t} G(\tau)d\tau = 0 \tag{2.1}$$

becomes true at time t [69]. With ζ the time at which the sequence started. This principal is used for generating an echo during the image acquisition phase within a MRI sequence. But it is also possible to generate extra gradient echoes during other parts of the sequence.

Figure 2.1 shows the MRI sequence used for retrospective triggering. The sequence differs from a regular FLASH sequence in that the slice-selection rephasing gradient does not coincide with the phase-encoding and read-out dephasing gradients. As a consequence the slice-selection rephasing gradient produces the desired navigator echo, indicated with 'nav'. Since this navigator echo in contrast to the image echo is not phase or frequency encoded in the image plane, it contains the integrated signal intensity of the whole slice navigator. The navigator echo is not a pencil beam often used for real-time respiration detection in humans [109]. While the integrated intensity of the image is changing over time by ventricle blood volume, flow artifacts and unsaturated tissue, the maximal signal intensity of the in-slice navigator echo and its phase are fluctuating. Not only the maximal signal intensity value and its corresponding phase of the navigator echo are influenced by

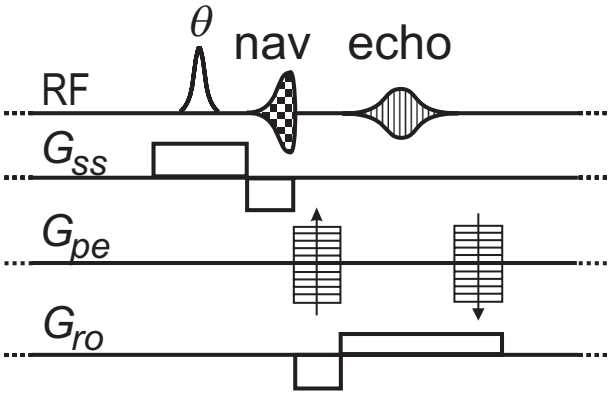

Figure 2.1: Flash sequence with navigator echo (nav). RF : RF-channel (RF pulse with flip angle θ) and image echo (echo) ; G_{ss}: slice-selection gradient; G_{pe}: phase encoding gradient; G_{ro}: readout gradient.)

respiration and cardiac activity, also the derivative of a first order polynomial fit through all points of the navigator echo signal intensity and phase show typical respiratory and cardiac patterns (see Figure 2.2A). Navigator echo analyses on one or two of the four derived signals of the navigator echo can separate the fluctuations caused by respiratory and cardiac activity and generate respiratory gating and cardiac triggering time points. By repeating many times this image sequence asynchronously to the respiratory and cardiac cycle, enough averages are made of individual k-lines to reconstruct CINE MRI images of the mouse heart with the navigator echo analyses.

Methods

MRI protocols

The examinations were performed with a 6.3 T horizontal-bore MR magnet (Oxford Instruments Superconductivity, Eynsham, Oxon, England) interfaced to a Bruker AVANCE (Bruker BioSpin MRI GmbH, Ettlingen, Germany) MR imaging console with ParaVision 3.0.2 software. The scanner was equipped with a custom made Magnex (Magnex Scientific Ltd., Yarnton, UK) gradient system (inner diameter, 12 cm; maximum gradient strength, 400 mT/m). A quadrature driven birdcage coil (Rapid Biomedical, Rimpar, Germany) with an inner diameter of 3.2 cm was used for RF transmission and signal reception. All MR sequences started with a steady-state preparation using dummy acquisitions for at least 5 seconds.

Prospective CINE MRI scans were collected with the use of a CINE FLASH sequence with the following parameters: Gaussian-shaped RF-pulse, 300 μs; flip angle, 15°; repetition time, 7 ms; echo time, 2.3 ms; sample rate, 100 kHz; echo position, 30%; field-of-view, 3x3

cm^2; matrix, 192x192; in-plane resolution, 156x156 μm^2; slice thickness, 1 mm; number of averages, 6 (with respiratory gating) or 12 (without respiratory gating); total acquisition time, approximately 5 min MRI scans started immediately at the up-slope of the ECG trigger pulse. The number of heart frames multiplied by the repetition time amounted to about 90% of the mean heart period as determined prior to the scan corresponding to 13-17 image frames per heart beat.
A modified FLASH sequence with a navigator echo (Fig. 2.1) was used for retrospective CINE MRI with the following parameters: Gaussian-shaped RF pulse, 300 μs; flip angle, 15°; repetition time, 7 ms; echo time, 2.98 ms; sample rate, 150 kHz; echo position, 50%; navigator echo points, 64; field of view, 3x3 cm^2; matrix, 192x192; in-plane resolution, 156x156 μm^2; slice thickness, 1 mm; number of repetitions, 230; total acquisition time, approximately 5 min (equal to the prospective method). The navigator echo analyses were done with a customized program within the ParaVision software using Fourier filtering techniques. Cardiac triggering and respiratory gating could be derived from: the maximum navigator signal intensity, the phase at maximum signal intensity, the derivative of a first order polynomial fit of the navigator signal intensity or the derivative of a first order polynomial fit of the unwrapped navigator phase. An experienced researcher decided which of the four resulted in the best usable signal. Usually this resulted in the same choice for both cardiac triggering and respiratory gating. A frequency selective band filter was used to extract the respiratory and the cardiac cycles. Subsequently, a maximum or minimum detection algorithm defined the trigger time points in the filtered signals, which established the synchronization between the respiratory or the cardiac cycle and the measured k-lines. Retrospectively, the k-lines measured during the inhalation and exhalation respiratory motion were excluded from the reconstruction of the images by defining a gating window around the respiratory trigger time points. The time between successive CINE frames was equal to the repetition time of the prospective method (7 ms) so that a direct comparison could be made between the prospective and retrospective methods. This corresponded to 14-18 image frames per heart beat.

In vivo measurements

Before the MRI examination, the mice were first sedated in an induction chamber by inhalation of 3 vol% isoflurane in medical air at a flow rate of 0.4 l/min When the respiration rate was slowed down to approximately 1 per second and the toe-pinch reflex was absent, the mice were transferred to a home-built cradle. A mask, which consisted of two concentric Perspex tubes, was used to supply anesthesia gas. The inner tube delivered the isoflurane (1.5 vol% in medical air; flow rate, 0.4 l/min), while the outer tube removed the excess gasses. To keep the body temperature constant, the mouse was positioned on

a Perspex pad that was circulated with heated water from a Lauda RE 204 heating bath (Lauda, Lauda Knigshofen, Germany). The mice were positioned supine on the warming pad with their head loosely fixed in the anesthesia mask. For ECG monitoring and cardiac triggering EEG paste (TEN20 from D.O. Weaver and Co., Aurora, CO USA) was put on the front paws to achieve good electric conductivity between the animal and the ECG unit (combined ECG and respiratory unit from Rapid Biomedical, Rimpar, Germany). The paws were then fixed on small copper ECG electrodes with the use of medical tape. During the examination the respiration rate was continuously measured with a balloon pressure sensor connected to the ECG/respiratory unit. The isoflurane concentration was adjusted to keep the respiration rate between 75 and 100 respirations/min. A rectal temperature sensor monitored the body temperature of the mouse and an extra temperature sensor was placed between the mouse and the heating pad (Luxtron M3300 fluoroptic thermometers, Santa Claren, CA USA). The body temperature of the mouse was kept at 37°C during the whole examination. The ECG, respiration and temperature signals were recorded continuously by a PC data acquisition board (National Instruments model PCI-6013, Austin, TX, USA), stored and visualized by an in-house developed LabVIEW program (National Instruments, Austin, TX USA).

Two groups of animals, four male Swiss and eleven male C57Bl6 mice, were measured with the prospective and retrospective CINE MRI methods. At the start of each examination several scout images were made in the transverse plane and the long-axis plane of the left ventricle to determine the orientation of the short axis. The location of the central short-axis slice was planned half way between the apex and base. Central short-axis slices of the four male Swiss mice (age 12 to 16 months; weight 40 to 50 g) were measured for the comparison of the SNR and CNR between the prospective and retrospective methods. Two prospective CINE methods were used, *i.e.* one with respiratory gating and one without, in order to compare the signal behavior of both prospective methods. To investigate possible effects of the order of repetitions, two retrospective CINE methods were used, *i.e.* either by filling the k-space of each frame by first repeating individual k-lines a number of times (referred to as 'repetition of k-lines') or by repeating k-space a number of times (referred to as 'repetition of k-space'). The two repetition methods may give different results when the cardiac and/or respiratory time periods change during the 5 minutes acquisition.

Eleven male C57Bl6 mice (age 7 months; weight 30 $\pm$ 1 g) were scanned to determine global heart parameters by acquiring a whole dataset of short axis CINE images, covering the heart from apex to base. Each slice was measured with the prospective method with respiratory gating directly followed by the 'repetition of k-lines' retrospective method. To enable the comparison with the heart and respiration periods derived from the navigator echo analyses, the externally measured heart and respiration periods, using the ECG/respiratory unit, were stored at 1 Hz frequency. The storage frequency was determined by a

sliding average algorithm within the storage program.

The Animal Care Committee of Maastricht University (Maastricht, the Netherlands) approved the experimental protocol.

In vitro measurements

To get more knowledge about the SNR and CNR characteristics of the sequences used in the absence of motion and blood flow transversal images were made of a phantom containing an aqueous solution of 0.01 mg/l $MnCl^2$, resulting in a T_1 and T_2 of 750 ms and 95 ms, respectively. For the prospective methods the respiratory period and heart period were simulated by two pulse generators. The pulse duration was set to 250 ms with a repetition time of 700 ms (86 cycles/min) for the simulated respiratory signal and for the simulated cardiac signal a pulse duration of 1 ms with a repetition time of 120 ms (500 cycles/min) was used.

Data analysis

For analyzing the SNR of the myocardial wall all CINE images of the four male Swiss mice were segmented manually and analyzed using Matlab 6.1 (The Mathworks, Inc., Natick, MA). The SNR values were calculated by dividing the mean signal intensity of the myocardial wall with the standard deviation of the noise level within a square region-of-interest (ROI) in the same CINE image at a location containing no signal or artifact. The mean SNR of the four mice was calculated for each heart frame and for each of the four acquisition methods. The CNR of each CINE image was determined by subtracting the mean signal value of the blood in the left ventricle from the mean signal value of the myocardial wall divided by the standard deviation of the noise. The mean CNR of the four mice was then calculated for each of the heart frames and the four measurement methods.
The global heart parameters EDV, ESV, CO and EF of the eleven mice were calculated using a semi-automatic segmentation with the CAAS MRV FARM program from Pie Medical Imaging, Maastricht, The Netherlands (see Chapter 3). During the end-systole heart phase the papillary muscles are not clearly separated from the myocardial wall and hence not detected by automatic segmentation. To avoid large errors in volume determination the papillary muscles were segmented manually in the end-diastole phase images. Left ventricle blood volume was subsequently corrected for the papillary muscle volumes. In order to facilitate a comparison between the measured and analyzed respiration and heart periods, the measured ECG and respiratory signals were linearly interpolated to

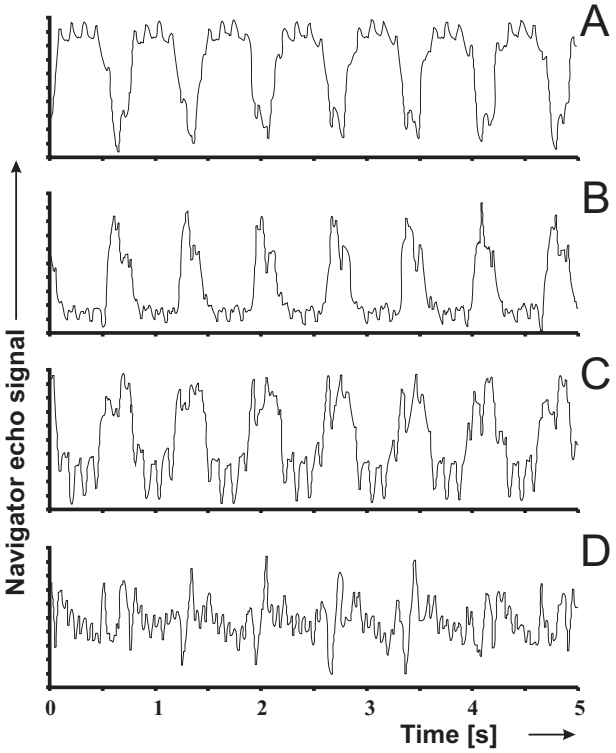

Figure 2.2: Navigator echo signals as function of time used for retrospective cardiac triggering and respiratory gating: A) the maximum navigator signal intensity, B) the phase at maximum signal intensity, C) the derivative of a first order polynomial fit of the navigator signal intensity and D) the derivative of a first order polynomial fit of the unwrapped navigator phase.

match the difference in sampling rate with the navigator analyses. The global heart parameters as well as the respiration and heart periods were analyzed in Bland-Altman plots comparing the prospective and retrospective method.

Results

The intensity and phase of the navigator echo signal were changing over time as a consequence of both the respiratory motion and most importantly the periodically changing 'bright' blood volume in the heart and large arteries. Figure 2.2 shows a typical result for the navigator echo signal intensity, the phase, as well as derivatives of first order polynomial fits of intensity and phase, as a function of time during a typical scan with the navigator echo sequence. During this scan the measured respiratory and heart period were 725 ms (83 respirations/min) and 122 ms (491 beats/min), respectively, which can also be seen as main components in the four signals depicted in Figure 2.2. This was also confirmed in the Bland-Altman plots in Figure 2.3, where a comparison is made between

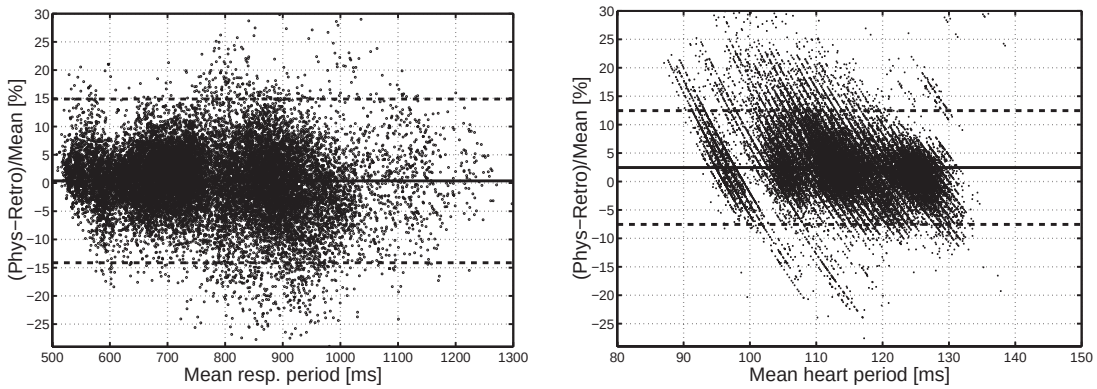

Figure 2.3: Bland-Altman plots for comparison of the respiratory period (n = 20245) and the heart period (n = 61966) between the measured respiratory and ECG signals (Phys) and the periods derived from the retrospective navigator echo analyses (Retro) during the acquisitions. Mean relative difference (solid line); Two times the standard deviation of the relative differences (dotted line).

the measured respiration and heart periods and the ones extracted from the navigator echo analyzed by the retrospective reconstruction program. For the analyses of the navigator signals in most cases frequency selective band filters of 470 to 1000 beats/min and 60 to 300 respirations/min were chosen for the heart and respiratory cycle, respectively. The window width for respiratory gating was set around 40% of the total respiratory period which was also used on the ECG unit for the prospective measurements. The relative differences in Figure 2.3 between the prospective and the retrospective respiratory periods were distributed around zero with a standard deviation of 8%. The relative difference between prospective and retrospective cardiac periods amounted to a SD of 5% and showed a small offset of 3%.

To allow for a detailed analysis of the SNR and CNR behavior during the cardiac cycle of the prospective and retrospective methods, the prospective method was applied with and without respiratory gating. This would clarify what the influences were on the SNR behavior of the respiratory gating and the partial coverage of the heart cycle by the prospective method compared to steady state SNR and CNR of the retrospective method. The four Swiss mice used for assessing SNR and CNR had a relatively low variation in heart rate and respiratory rate throughout the examinations ranging from 490 to 520 beats/min and 80 to 90 respirations/min, respectively. Typical short-axis CINE MR images at end-diastole, end systole and mid-diastole heart phases of the prospective CINE method with and without respiratory gating and the retrospective method with 'repetition of k-space' are shown in Figure 2.4. The retrospective method (Fig. 2.4C) showed a more homogeneous intensity in the left ventricle heart wall compared to the prospective method without respiratory gating (Fig. 2.4B) and smaller changes in signal intensity between the different heart frames compared to the prospective method with

respiratory gating (Fig. 2.4A). The SNR of the retrospective method seems visually less than for the prospective method, which will be quantified further on. Flow artifacts in the left ventricle were less in the retrospective data (Fig. 2.44, C3) compared to the corresponding prospective data (Fig. 2.4, A3 and B3). No observerable differences could be observed between the CINE images of the two retrospective methods 'repetition of k-lines' and 'repetition of k-space' (data not shown).
Figure 2.5A shows the mean SNR of the myocardial wall for four Swiss mice during all heart frames. The prospective methods resulted in an approximately 90% higher SNR. However, the prospective methods displayed a larger difference in SNR between the start and the end of the cardiac cycle compared to the two retrospective methods, which had an almost equal SNR. The retrospective method 'repetition of k-lines' had a small advantage in mean SNR and mean CNR compared to the retrospective method 'repetition of k-space'. To get more insights in the SNR behavior of both methods a phantom study

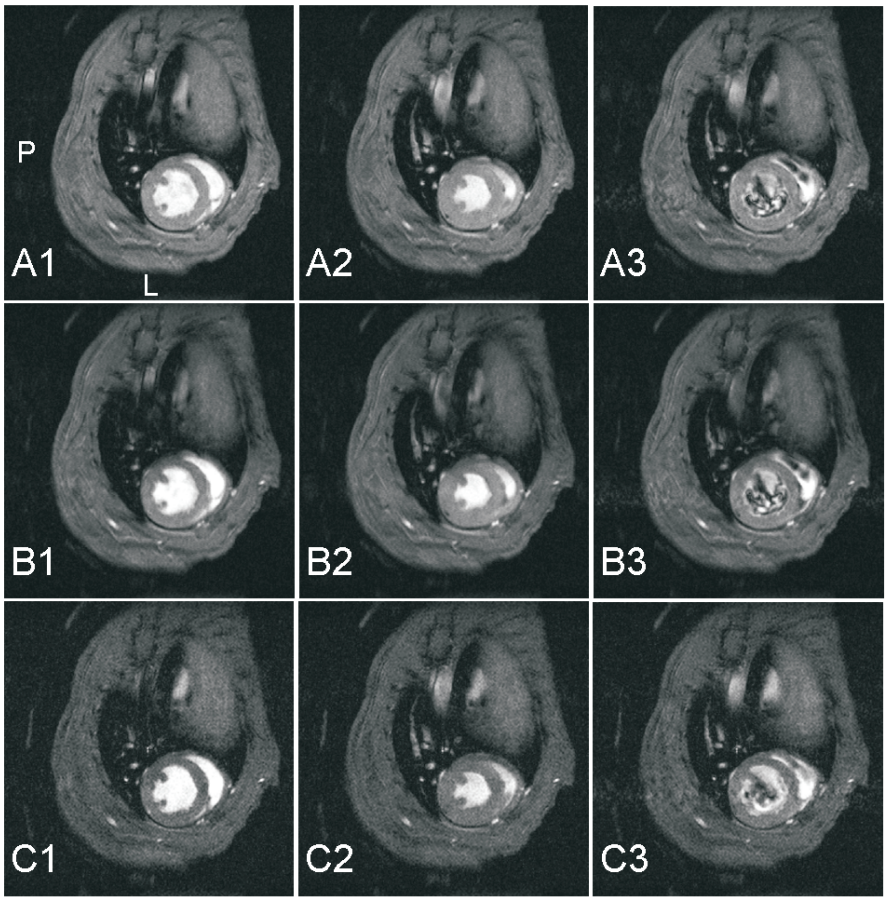

Figure 2.4: Short axis view of a mouse heart acquired with: A) prospective method with respiratory gating; B) prospective method without respiratory gating; C) retrospective method 'repetition of k-space '. Heart phases: 1) end-diastole; 2) end-systole; 3) mid-diastole.

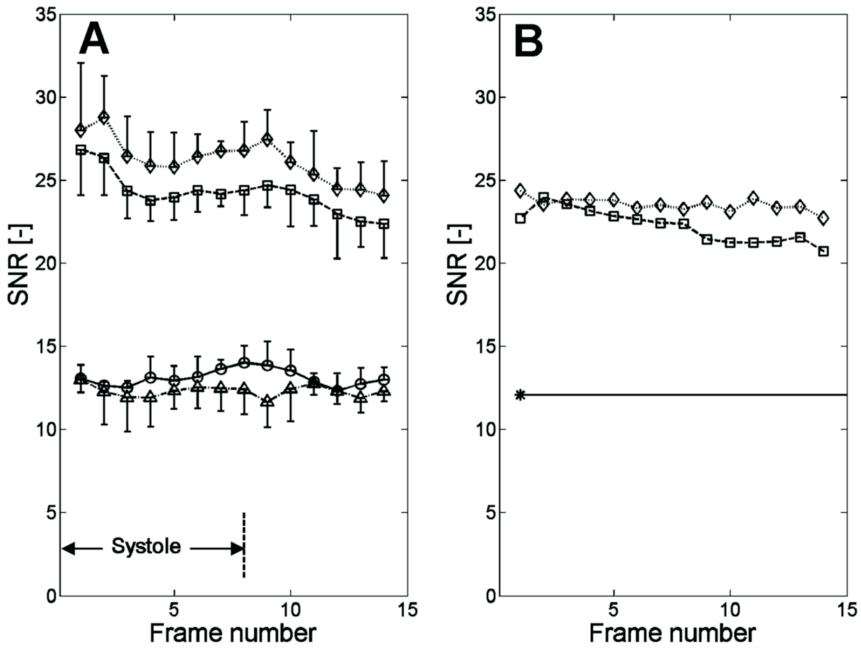

Figure 2.5: A) Mean SNR (mean ± SD) of the myocardial wall of four mice per heart frame measured with the four methods. Prospective method with respiratory gating (◊); prospective method without respiratory gating (□); retrospective method 'repetition of k-space' (△); retrospective method 'repetition of k-lines' (◯). B) SNR of a phantom measured with simulated respiration and heart rate. Prospective method with respiratory gating (◊); prospective method without respiratory gating (□); Retrospective method (∗).

was carried out. This showed the same SNR behavior for the prospective method with respiratory gating and the retrospective method (Fig. 2.5B), although the prospective method without respiratory gating had less change in SNR as for the *in vivo* case (Fig. 2.5A) during the cardiac cycle. Since there are obviously no real cardiac and respiratory variations of the navigator signal in the phantom, the signal intensities in the retrospective images of the phantom were equal for all frame numbers and for both repetition methods. Therefore only a single data point for the retrospective methods is shown in Fig. 2.5B, which had almost the same SNR as both retrospective methods *in vivo*.

The mean CNR between the blood in the left ventricle and the myocardial wall was also higher for the prospective methods as compared to the retrospective methods, as shown in Table 2.1, although the difference was not as high as for the mean SNR. The CNR was approximately equal for both retrospective methods.

A comparison of the global functional indices of the eleven C57Bl6 mice is shown in the Bland-Altman plots in Figure 2.6. No outliners were found in these plots. The EDVs of the prospective method with respiratory gating methods and the retrospective method

Table 2.1: Mean CNR (mean ± SD; n = 4) between the blood in the left ventricle and the myocardial wall measured at the end-diastole and end-systole heart phase with: A) prospective method with respiratory gating; B) prospective method without respiratory gating; C) retrospective method 'repetition of k-space'; D) retrospective method 'repetition of k lines'.

	A	B	C	D
End-diastole	23 ± 2	20 ± 1	14 ± 1	15 ± 3
End-systole	30 ± 2	23 ± 1	16 ± 2	15 ± 2

'repetition of k-lines' were almost equally distributed around the zero axis in the Bland-Altman plot with a small standard deviation (SD = 4.4%). In contrast, the ESV was about 8% smaller for the prospective method as compared to the retrospective method, with a standard deviation of about 11%. Since EDV and ESV combine to the SV and the EF, this offset in ESV resulted also in a small positive offset for the EF and SV. The mean values of the global indices EDV, ESV, SV and EF were comparable with values reported in two previous studies of Franco *et al.* [29] and Kober *et al.* [110], who used mice of comparable age and body weight.

Discussion

We successfully implemented the retrospective method, which produced mouse cardiac CINE MR images (Fig. 2.2) that can compete in image quality with the CINE images of Hiba *et al.* [105] measured with a self-gated radial MRI sequence. The authors used the zero crossing of the radial acquired image echo for detecting the cardiac and respiratory motion. It seems that the navigator echo as employed in the present study is more sensitive to respiratory motion compared to the self-gated radial sequence [105]. However, it is well possible that the use of a surface coil by Hiba *et al.* [105] reduces the respiratory motion sensitivity as compared to the volume coil used in our study. In another study of Bishop *et al.* [100] the retrospective CINE MRI reconstruction was implemented by combining recorded ECG and respiration signal with the MR image data, which were measured at the same time. The advantage of our method as compared to the retrospective method of Bishop *et al.* [100] is that we do not need extra registration of the ECG and respiration and time synchronisation between scanner and registration equipment. In our method the navigator echo and image information are directly coupled.
The Bland-Altman plot of the respiratory periods (Fig. 2.3A) showed a clear statistical spread of data points from which it can be concluded that the used analysis method suc-

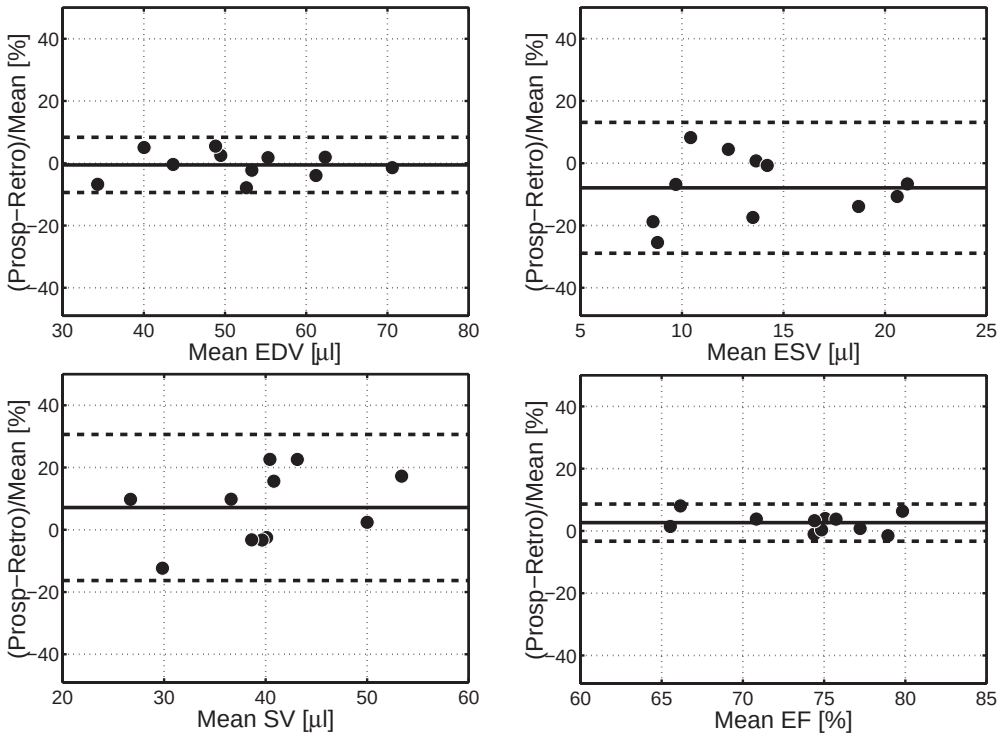

Figure 2.6: Bland-Altman plots of: EDV, ESV, SV and EF, compared between the prospective method with respiratory gating and retrospective method 'repetition of k lines' (n=11). Mean relative differences (solid lines); 2 times the standard deviation of the relative differences (dotted lines).

cessfully extracts the correct respiratory periods. The diagonal lines in the Bland-Altman plot of the heart periods (Fig. 2.3B) arise from the fact that the sampling rate of the ECG signal differed considerably in comparison to the heart rate of a mouse. Small and fast changes in the cardiac period could only be detected by the navigator analyses and were not recorded by our computer program due to discrete sampling and filtering. The small offset on the relative difference of the heart period (Fig. 2.3B) between the two methods was probably due to the fact that for the retrospective method the heart periods close to the respiration were estimated somewhat too short because of some interference with the respiration part of the navigator signals.

The smaller flow artifacts during the mid-diastole heart phase for the retrospective method (Fig. 2.4, C3) compared to the prospective methods (Fig. 2.4, A3 and B3) are probably a result of the fact that k-lines are measured asynchronously with the cardiac and respiratory cycle. This leads to some repetition of k-lines within a small time frame and hence some averaging out of the flow artifacts. In the prospective approach k-lines are always measured at almost the same time points in the cardiac cycle.

The SNR and CNR of the prospective method are significantly better than for the retrospective method. This is mainly caused by the fact that the prospective method never

fully reaches a steady state longitudinal magnetization due to the periodic pauses in the sequence during the breathing period of the mouse. Since the transient signals of the FLASH sequence are stronger, this effectively leads to higher SNR in the images. This also explains the observation that the SNR of the prospective methods decreased during the cardiac cycle. The comparison of the mean SNR (Fig. 2.5) and mean CNR (Table 2.1) between the prospective and retrospective methods is not completely fair, because a different band width and echo position were used for the two methods. We estimated, however, that the difference in sample bandwidth (100 kHz vs. 150 kHz) and echo position (30% vs. 50%) only leads to an approximately 10% higher SNR and CNR of the prospective method as compared to the retrospective method [111].

The SNR of the prospective method without respiratory gating is not constant during the cardiac cycle, which is in contrast to what is expected and observed in the phantom. We infer that this is caused by residual periodic pauses in the sequence during the breathing period of the mouse. In these pauses cardiac triggering signals are sometimes missing because of electrical distortions of the ECG signal by breathing. The result is a comparable transient behavior during the cardiac cycle as for the fully respiratory gated prospective method, be it with shorter periodic pauses.

All four curves of the SNR as function of the frame number in Fig. 2.5 show a small peak or dip at the end of the systolic heart phase. Closer inspection of the CINE images revealed that these are likely caused by artifacts from fast flowing blood at end diastole and begin systole. These artifacts might be suppressed using black blood imaging methods [112]. The difference in mean CNR (Table 2.1) between the two methods could be the reason for the differences found in the ESV (Fig. 2.6B), which is more sensitive to small errors in the correct segmentation of left ventricle cavity and myocardial wall due to its small volume in comparison to the larger EDV (Fig. 2.6A). This also accounts for the larger standard deviation observed in Fig. 2.6B.

Retrospective CINE MRI of the mouse heart as presented in this chapter has the advantage that ECG leads and respiratory sensors become obsolete. This is especially advantageous when measuring diseased animals, for example with a cardiac infarction, from which it is often difficult to extract a usable ECG signal. The retrospective method has the disadvantage of a lower SNR (Fig. 2.5A). However, the SNR could be improved by using non uniform k space filling schemes that favor low k-space lines. More importantly, the retrospective method allows for steady state acquisition, which is essential for quantifying the contrast in CINE MR images especially for molecular MR imaging of the heart using targeted contrast agents. A further advantage of the retrospective method is that it is a general-purpose method which can be used not only for cardiac MRI but also for *e.g.* abdominal imaging in humans [113] or animals.

Conclusion

We have presented a retrospective CINE FLASH sequence for mouse cardiac MRI. The CINE images recorded using this sequence were free of respiration and cardiac movement artifacts. The method makes ECG leads and respiratory sensors redundant and has the distinct advantage that a steady-state longitudinal magnetization is maintained throughout the cardiac cycle. Retrospective triggering results therefore in almost constant left ventricle wall signal intensity throughout the cardiac cycle, however at the expense of a decrease in the overall SNR and the CNR between blood and myocardial wall. Functional heart parameters EDV, ESV, SV, and EF determined using the prospective and retrospective methods were compared. Largest differences were found for the ESV which was about 8% lower for the prospective method. Both methods resulted nonetheless in almost equal EF.

Evaluation of manual and automatic segmentation of the mouse heart from CINE MR images

Edwin Heijman[1], Jean-Paul Aben[2], Cindy Penners[2], Petra Niessen[3], René Guillaume[2], Guillaume van Eys[3], Klaas Nicolay[1] and Gustav J. Strijkers[1]

[1] Biomedical NMR, Department of Biomedical Engineering, Eindhoven University of Technology, Eindhoven, the Netherlands

[2] Pie Medical Imaging BV, Maastricht, the Netherlands

[3] Department of Molecular Genetics, Cardiovascular Research Institute Maastricht (CARIM), University of Maastricht, Maastricht, the Netherlands

Published: J Magn Reson Imaging. 2008 Jan;27(1):86-93.

Abstract

In this study a comparison was made of global functional parameters determined from a stack of cinematographic MR images of mouse heart which were segmented by a manual segmentation and an automatic segmentation algorithm. The automatic segmentation was based on propagation of a minimum cost algorithm in polar space starting from manually drawn contours in one heart phase. Twenty-two mouse hearts were segmented manually and automatically. Intra- and inter-observer variability as well as validity of the automatic segmentation was determined. To test the reproducibility of the algorithm the variability was calculated from the intra- and inter-observer input.

There were no significant differences between the automatic and the manual segmentation except for the end systolic epicardial volume. The automatically derived volumes correlated well with the manually derived volumes ($R^2 = 0.90$); left ventricular mass with and without papillary muscle showed a correlation R^2 of 0.74 and 0.76, respectively. The manual intra-observer variability was superior to the inter-observer and the variability of the automatic segmentation, while the manual inter-observer variability was comparable to the variability of the automatic segmentation. The automatic segmentation algorithm reduced the bias of the intra- and inter-observer variability. The mean time of segmentation for one dataset was around 10 minutes and circa 2.5 hours for automatic and manual segmentation, respectively.

We conclude that automatic segmentation of the mouse heart provides a fast and valid alternative to manual segmentation of the mouse heart.

Introduction

In cardiovascular research *in vivo* imaging studies of mice are indispensable to gain an improved understanding of normal and pathological cardiac function. MRI, as a non-invasive high resolution imaging method, is the leading technique to measure global functional parameters of the mouse heart. The principal global functional parameters of interest are the end-diastolic volume (EDV), the end-systolic volume (ESV), the stroke volume (SV), ejection fraction (EF) [114] and the heart weight [115]. With MRI, these parameters can be determined by measuring a stack of slices, usually oriented parallel to the short-axis plane of the mouse heart between apex and base [48]. These short-axis slices minimize partial volume effects and are largely perpendicular to the direction of wall motion and wall thickening. At each slice position, a series of cinematographic (CINE) MR images is collected, which can be done by ECG triggering [32] or retrospective reconstruction [107]. The myocardial wall and cavity volumes of the left or right ventricle of the heart are found by segmentation of the epicardial and endocardial borders within each slice and time frame. From the resulting myocardial wall and cavity volumes global functional parameters of the mouse heart are calculated.

Global functional parameters of the mouse heart are primarily used for two applications. The first is phenotyping of genetically modified mice and their wild-type controls [29, 30, 36, 37]. The second application is characterizing the diseased heart [10, 17, 38–40], sometimes combined with a study of the effects of a particular intervention [41–47]. To validate the values of the MRI-based global functional parameters several authors compare their findings with *ex vivo* measurements of the weight of the mouse heart [26] or to other volume measurements using *e.g.* Positron Emission Tomography [116] as well as the conductance microcatheter technique [117]. However, it is difficult to estimate the errors within the global functional parameter values caused by the segmentation of the mouse heart from the MR images. To the best of our knowledge only Ruff *et al.* [32] and Schneider *et al.* [69] published intra- and inter-observer variability for their manual segmentation of the mouse left ventricle.

With decreasing MR acquisition times resulting in higher throughputs and developments in multiple mouse MRI [118], automatic segmentation procedures become indispensable for studying large groups of mice. A fully automatic segmentation procedure of MR images is very complicated due to the different image contrasts that are possible with the different MR sequences and MR parameters. The word automatic is therefore not fully correct for most segmentation programs, as some user input, such as starting contours of the segmentation, is required to accomplish the segmentation task. Although strategies for automatic segmentation of the mouse heart already have been reported [119], the performance of automatic segmentation procedures within a large population of mouse hearts has not been addressed so far. The purpose of this study was therefore to evaluate

manual and automatic segmentation of short-axis CINE MR images. Data collected from 22 mouse hearts were used.

Methods

MRI protocol

MRI measurements were performed with a 6.3 T horizontal-bore animal scanner (Bruker BioSpin, Ettlingen, Germany) and a 3 cm diameter birdcage RF coil. The mice were first sedated with isoflurane in medical air at an induction level of 3 vol%. After the absence of the toe-pinch reflex the mice were transferred to a special designed mouse cradle with an anesthesia mask and a warming pad. A sensor was placed on the chest of the mouse to monitor its respiration and for respiratory gating. The mouse was positioned supine and the front paws of the mouse were fixed on copper electrodes for ECG triggering. For ECG monitoring and cardiac triggering EEG paste (TEN20 from D.O. Weaver and Co., Aurora, CO USA) was put on the front paws to achieve good electric conductivity between the animal and the ECG unit (combined ECG and respiratory unit from Rapid Biomedical, Rimpar, Germany). During the experiments the mice were sedated using 1.5 vol% isoflurane in medical air at a flow rate of 0.4 l/min. CINE MRI scans were collected with the use of a FLASH sequence [32] with the following parameters: repetition time, 7 ms; echo time, 2.3 ms; field of view, 3x3 cm^2; matrix, 192x192; reconstruction matrix 256x256; slice thickness, 1 mm; total acquisition time per slice, 5 min. MRI scans started immediately at the up-slope of the ECG trigger pulse. The number of heart frames multiplied by the repetition time amounted to about 90% of the mean heart period as determined prior to the scan, corresponding to 13-17 image frames per heart beat.

In vivo measurements

C57Bl6 mice (age 8 months; n = 22) consisting of two groups of eleven genotype Smtn-$B^{+/+}$ C57Bl6 mice and eleven genotype Smtn-$B^{-/-}$ C57Bl6 mice [120] were scanned to determine global functional parameters of the mouse heart. Smtn-$B^{-/-}$ mice lack smoothelin-B actin binding proteins in vascular smooth muscle, resulting in reduced arterial contractility. As a consequence these mice have mild cardiac hypertrophy with a somewhat higher ejection fraction as compared to their littermates. Functional consequences of Smoothelin-B deficiency will be discussed in Chapter 4. In this chapter we will focus on the evaluation of the manual and automatic segmentation of the left ventricle of all 22 mice.

At the start of each examination several scout images were made in the transverse plane and in two perpendicular long-axis planes of the left-ventricle to determine the orientation of the short axis. To create a multi-slice MR CINE dataset short axis measurements were sequentially performed with the above described MR sequences at different long axis heights. The whole short-axis dataset was planned between the apex and base during the begin-systolic heart phase.

The Animal Care Committee of Maastricht University (Maastricht, the Netherlands) approved the experimental protocol.

Image Analysis

All CINE MR images were transferred to a Microsoft Windows based personal computer for further analysis. The manual as well as the automatic segmentations were performed within the CAAS-MRV FARM software package (version 1v0, Pie Medical Imaging BV, Maastricht, The Netherlands) with an extra procedure for extracting the papillary muscles automatically. The manual segmentation was based on a closed spline curve fitting technique through user defined points. By adding, adjusting or removing points the curve is tailored to the desired shape. Typically seven points are sufficient to indicate the endocardial or epicardial heart wall. Papillary contours were drawn by the observer. To determine inter-observer variability of the manual segmentations, manual contours were drawn by two independent observers (E.H. and P.N.) by tracing the endocardial, epicardial and the papillary muscles on the short-axis slices in the end-diastolic and end-systolic heart phases. One observer (E.H.) repeated the manual segmentation in order to derive the intra-observer variability. Papillary muscles and trabeculations were treated as being part of the blood pool. However, for the left ventricular mass results are presented both with and without papillary muscles.
The automatic segmentation was based on the principle in which a manually defined endocardial and epicardial contour of one heart phase of each slice is required. Propagation was performed through the time series of each slice, hereafter called frames. The algorithm is based on dynamic program techniques and relies heavily on a minimum cost algorithm in polar space [121]. For our purpose the cost function used weighted costs of neighboring frames where the cost was constructed from grey values and their gradients. Papillary muscles were extracted by a threshold technique, where the threshold is defined in each frame separately. We have to stress here that for the current study, no manual corrections were performed following the above automatic segmentation. Several global left ventricle function parameters were derived during post processing. The endocardial and epicardial volumes were computed using Simpson's rule [122], *i.e.* the areas of the endocardial

and epicardial contours were summed over all slices and multiplied by the slice thickness. EDV and ESV were determined by the end-diastolic and end-systolic endocardial volume, respectively. The LVM was calculated by taking the difference between the end-diastolic epicardial volume and the end-diastolic endocardial volume multiplied by 1.04 g/cm^3 [29], the specific density of the myocardial tissue. The LVM was also calculated by adding the papillary muscles as part of the myocardial tissue. Finally, the ejection fraction (EF) was obtained by calculating the stroke volume from the end-diastolic and end-systolic endocardial volumes, divided by the end-diastolic endocardial volume and multiplied by 100%.

Statistical Analysis

To compare the different segmentation methods, absolute and relative differences of the mean were calculated for seven parameters: the endocardial and epicardial volumes at the end-diastolic and end-systolic heart phases, EF, and LVM with and without papillary muscles. To determine the intra-observer variability of the manual segmentations, the mean differences and standard deviations of these parameters were determined between the two manual segmentations of observer E.H. To determine inter-observer variability the mean differences and standard deviations of the mean of the segmentations performed by E.H. were compared to observer P.N.

One of the goals of our evaluation study was to compare the results of the automatically derived contours with the results based on the manual contours. The appropriate term to express the level of agreement between the automatic and manual segmentation is "validity" instead of "accuracy" in view of the fact that no gold standard exists [123]. To assess the validity of the segmentation algorithms, the derived endocardial and epicardial volumes, EF, and the LVM with and without papillary muscles were compared with the manually derived values of the first observer (E.H.). The validity was expressed as the mean and standard deviation of the paired differences in each data set. A two-tailed, paired Student's t test was performed to determine the statistical significance of the observed differences, where $p < 0.05$ was considered to be statistically significant. A linear regression analysis of computed versus manually determined values was applied to quantify the correlation between the automatic and manual segmentations. To put the observed difference in perspective we compared them against the intra- and inter-observer variability as found from the manual segmentation by the two observers.

On the basis of the available three sets of manually drawn contours, an estimate of the true reproducibility of the algorithm was derived. As described, the automatic segmentation was started from manually drawn short axis endocardial and epicardial contours in only one frame of the multi-slice CINE MR datasets. A prerequisite for determining the reproducibility of the segmentation algorithm is that no manual corrections are

made afterwards. To assess the reproducibility of the automatic segmentation algorithm, intra- and inter-observer variability was calculated from the automatic segmentation results derived from the automatic segmentation initiated by the manual starting contours drawn by the two observers. For determining the end-systolic volume automatically, the algorithm was started from the manually drawn end-diastolic contours of both observers and propagated towards the end-systolic heart phase. To determine the end-diastolic volumes automatically, the propagation procedure was repeated in the reversed direction. The difference between the two automatic segmentation results based on the manual contours from observer E.H. resulted in the intra-observer variability of the automatic segmentation algorithm. The corresponding inter-observer variability of the automatic segmentation was derived by taking the mean differences and standard deviation of automatic segmentation results of the first set of observer E.H. versus the second set of E.H., and by comparing the manual segmentation of P.N. versus the second set of E.H. Variability of both these observers is a measure for the reproducibility of the automatic segmentation algorithm.

Results

Short-axis MR images at the end-diastolic and end-systolic heart phase of a genotype Smtn-$B^{+/+}$ C57Bl6 mouse and genotype Smtn-$B^{-/-}$ C57Bl6 mouse are shown in Figure 3.1 in the upper and lower row, respectively. The upper left image contains also the segmentation contours of the epicardial, endocardial borders as well as the papillary muscles as drawn by observer E.H.

We were only interested in the segmentation results and therefore we treated the Smtn-$B^{+/+}$ and Smtn-$B^{-/-}$ mice as one group. The mean global parameters (mean $\pm$ SD) of the two manual segmentations of observer E.H. were; EDV: 51 ± 9 μl, ESV: 15 ± 5 μl, EF: 71 $\pm$ 4 % and LVM: 107 ± 14 mg (without papillary muscles LVM: 101 ± 13 mg). EDV, ESV and EF were comparable with values reported in two previous studies of Franco *et al.* [29] and Kober *et al.* [110], who used mice of comparable age and body weight. The mean time needed for manually segmenting the multi-slice dataset of one heart frame was 9 min for both segmentations of observer E.H. The mean time of segmenting a total multi-slice multi-frame dataset was circa 2.5 hours. For the automatic segmentation, the mean propagation time after manual segmentation for the complete multi-slice multi-frame dataset was about 20 seconds with the use of a 2.4-GHz Intel Pentium IV processor (including 250 images). The mean time of the automatic segmentation including manual segmentation of the first frames, therefore amounted up to approximately 10 minutes for the complete multi-slice multi-frame dataset.

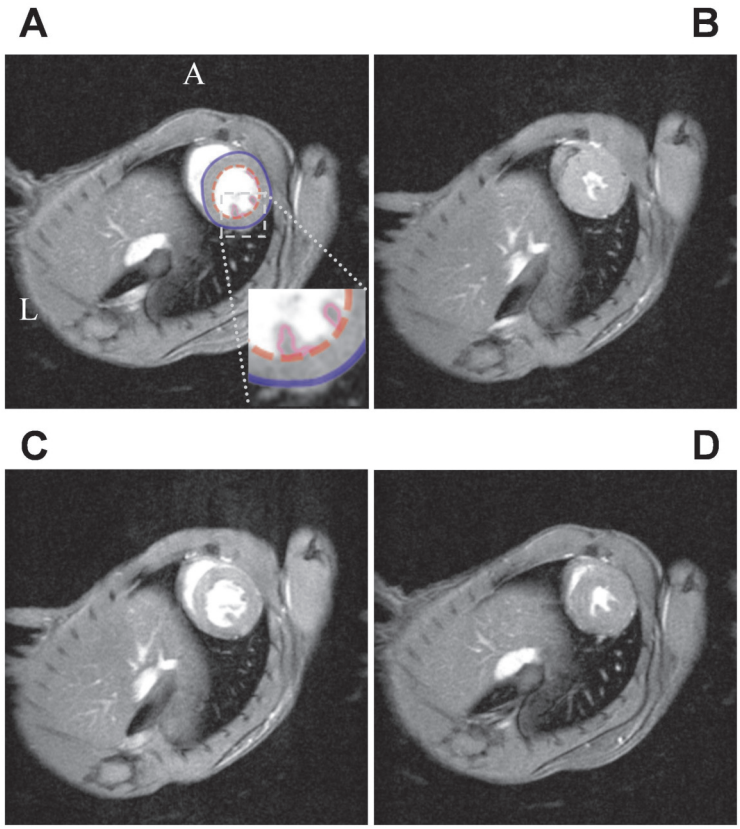

Figure 3.1: Short-axis MR images of a Smtn-B$^{+/+}$ C57Bl6 mouse heart at the end-diastolic (A) and end-systolic (B) heart phase and Smtn-B$^{-/-}$ C57Bl6 mouse heart at the end-diastolic (C) and end-systolic (D) heart phase. As an example, contours drawn by observer E.H. are overlaid in A with; red: endocardial contour, blue: epicardial contour and purple: the papillary muscles.)

Intra- and inter-observer variability of manual segmentations

The intra- and inter-observer variability of the manual segmentation are presented in Table 3.1. Values for intra- and inter-variability were in general small with a few exceptions. There was a large standard deviation for the intra-observer variability (10%) and inter-observer variability (9%) of the end systolic endocardial volume. A statistically significant inter-observer difference also existed for all values except for the EF. An excellent level of agreement was found for the EF intra- and inter-observer variability, which was smaller than 1 percent point with a maximum standard deviation of 4%. As a result of the intra- and inter-observer variability of the endocardial and epicardial volumes the mean difference of the LVM with and without inclusion of papillary muscles increased. The manual segmentation of the papillary muscles resulted in a higher standard deviation, but a decreased mean difference for both the intra- and inter-observer variability.

Table 3.1: Intra- and inter-observer variability of manual segmentation (n = 22).

	intra-observer variability		inter-observer variability	
	value	percentage	value	percentage
endocardial volume [μl]				
end-diastolic	-0.29 ± 1.08	-0.57 ± 2.11	-4.28 ± 2.28*	-8.00 ± 4.26
end-systolic	-0.38 ± 1.49	-2.51 ± 9.84	-1.58 ± 1.45*	-9.80 ± 9.13
epicardial volume [μl]				
end-diastolic	-0.94 ± 2.63	-0.64 ± 1.78	5.54 ± 4.67*	3.82 ± 3.22
end-systolic	-0.38 ± 1.49*	-1.54 ± 2.30	4.74 ± 4.15*	3.85 ± 3.37
EF [%]	0.56 ± 2.52	0.79 ± 3.55	0.64 ± 2.39	0.91 ± 3.39
LVM [mg]	-0.68 ± 2.70	-0.67 ± 2.67	10.32 ± 4.77*	10.74 ± 4.97
LVM (papillary included) [mg]	-0.53 ± 3.84	-0.50 ± 2.91	8.78 ± 5.59*	8.53 ± 5.42

Note. Data are mean difference ± SD
* Statistically significant ($p < 0.05$).

Validity of automatic segmentation

Table 3.2 shows the comparison between the automatic and manual segmentations. There was a good agreement ($R^2 = 0.85$ to 0.93) between the automatic and manual measurements of the endocardial and epicardial volumes. Lower linear correlations were found for the EF and the LVM with R^2 of 0.60 and 0.75, respectively. However, these lower R^2 values could both be explained by the limited range of their values compared to the variability (see Fig. 3.2), in which case a linear regression technique is less applicable.
For all measured global left ventricular functional parameters the mean difference of the automatic segmentation was within 3% of those obtained by manual segmentation. We observed an underestimation of the end-diastolic volumes and an overestimation of the end systolic volumes. The difference was statistically significant only for the end-systolic epicardial volume. All mean difference results were better than the inter-observer mean differences listed in Table 3.1, except for the EF. The standard deviations were comparable with those found for the inter-observer comparisons listed in Table 3.1. Furthermore, the results in Table 3.2 were slightly worse than the intra-observer variability. The results are further detailed in Bland-Altman plots [124] in Figure 3.3. The scatter of the differences did not show any relation with the mean value, indicative of a constant performance over the range of values.

Reproducibility of automatic segmentation algorithm

The reproducibility of the automatic segmentation algorithm is presented in Table 3.3 as the intra- and inter-observer variability. These values were obtained when using the manually drawn contours by the two observers (E.H. and P.N.) as starting condition. As compared to the full manual segmentation, the mean differences of the endocardial volumes were decreased, although the standard deviations were comparable. For the epi-

Table 3.2: Comparison of automatic and manual LV segmentation (n = 22).

	auto-manual[1] (absolute)	auto-manual[1] (relative%)	linear regression	R^2
endocardial volume				
end-diastolic	-1.47 ± 3.75 μl	-2.87 ± 7.30	1.01x - 1.77	0.85
end-systolic	0.46 ± 1.53 μl	3.06 ± 10.13	0.97x + 0.97	0.91
epicardial volume				
end-diastolic	-0.35 ± 5.87 μl	-0.23 ± 3.97	0.98x + 3.18	0.92
end-systolic	3.23 ± 5.02 μl*	2.57 ± 3.99	0.88x + 18.56	0.93
EF	-1.71 ± 3.87 %	-2.40 ± 5.45	0.86x + 8.16	0.60
LVM	1.18 ± 8.02 mg	1.17 ± 7.92	1.07x - 6.04	0.74
LVM (papillary included)	3.17 ± 7.88 mg	2.95 ± 7.34	1.03x - 5.96	0.76

Note: relative difference is taken with respect to manual value
[1] Data are mean difference ± SD of the differences
* Statistically significant ($p < 0.05$).

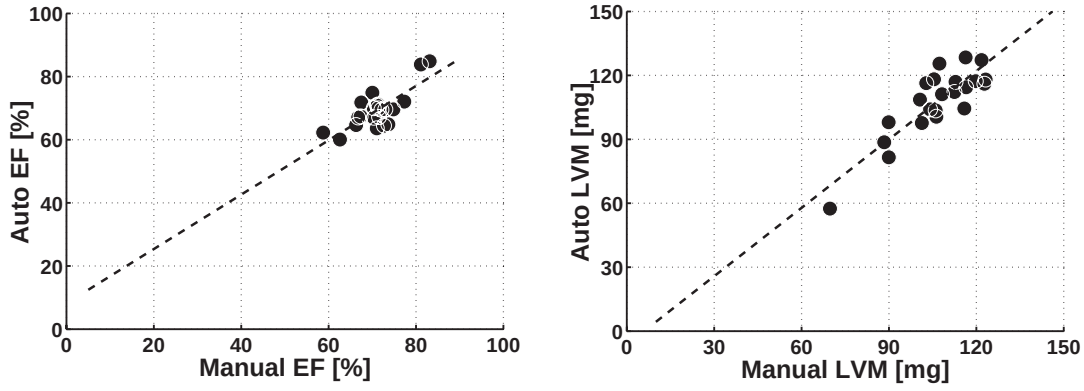

Figure 3.2: Linear regression analyses between the manual segmentation of observer E.H. (x-axis) and the automatic segmentation (y-axis) of two global functional parameters: the ejection fraction (left) and left ventricle mass without papillary muscles (right) with the dotted line according to y = 0.86x + 8.16 (R^2 = 0.60) and y = 1.07x - 6.04 (R^2 = 0.74), respectively.

cardial volumes the standard deviations were reduced with approximately 1 percent point compared to the manual segmentation except for the end-diastolic epicardial volumes of the intra-observer variability. The mean difference as well as the standard deviation of the epicardial end-diastolic volume of the intra-observer variability were increased compared to the values in Table 3.1. This was probably also the cause for the high intra-observer variability of the algorithm for the LVM (both with and without papillary muscles). In contrast the LVM of the inter-observer variability of the algorithm had decreased compared to the manual inter-observer variability. The EF had lower values for the mean difference compared to Table 3.1, but slightly increased standard deviation.
As a summary, Figure 3.4 shows an overview of the variability of four global functional parameters derived from the intra-observer and inter-observer analysis and the reproducibility of the automatic segmentation with the start contours of the intra-observer and inter-observer analyses. It is clear that the EF was the most stable global functional

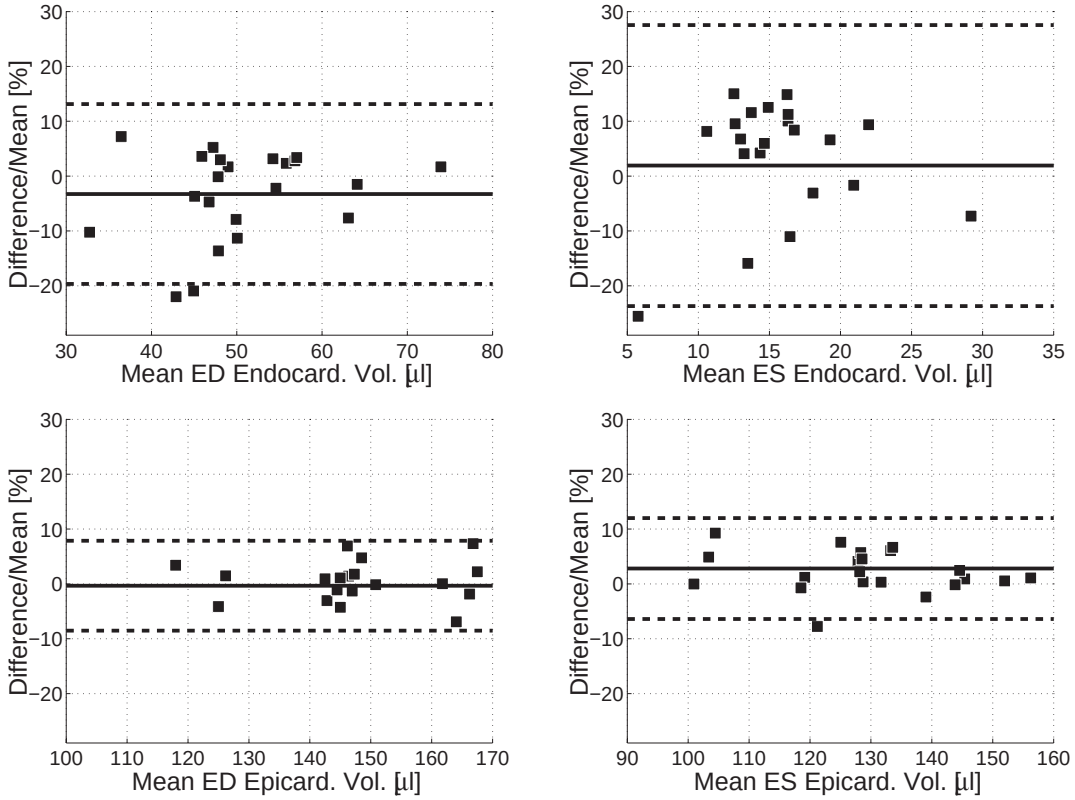

Figure 3.3: Blandt-Altman plots of the comparison between the manual segmentation of observer E.H. and the automatic segmentation for: the end-diastole endocardial volume (upper left), the end-systole endocardial volume (upper right), the end-diastole epicardial volume (lower left) and the end-systole epicardial volume (lower right) of the twenty-two mice (squares). Solid line is the mean difference [%] and the two dotted lines are 2 times the standard deviation.

Table 3.3: Intra- and inter-observer variability of automatic segmentation algorithm (n = 22).

	intra-observer variability		inter-observer variability	
	value	percentage	value	percentage
endocardial volume [μl]				
end-diastolic	-0.08 ± 1.90	0.16 ± 3.81	-0.69 ± 2.40	-1.38 ± 4.77
end-systolic	-0.00 ± 1.55	-0.03 ± 9.81	-0.09 ± 1.46	-0.55 ± 9.18
epicardial volume [μl]				
end-diastolic	-3.18 ± 5.29*	-2.14 ± 3.55	2.52 ± 3.10*	1.70 ± 2.10
end-systolic	-0.02 ± 2.55	-0.02 ± 1.98	0.79 ± 3.08	0.62 ± 2.40
EF [%]	-0.09 ± 3.74	-0.14 ± 5.44	-0.15 ± 3.55	-0.22 ± 5.15
LVM [mg]	-3.42 ± 5.68*	-3.29 ± 5.45	3.37 ± 4.11*	3.29 ± 4.02
LVM (papillary included) [mg]	-3.12 ± 5.33*	-2.93 ± 5.02	3.03 ± 3.98*	2.90 ± 3.80

Note. Data are mean difference ± SD
* Statistically significant ($p < 0.05$).

parameter with in general the lowest mean difference and smallest standard deviation. The end-systolic endocardial volume had the largest standard deviation for all methods making it the parameter that is most sensitive to the segmentation method. The mean differences of the parameters end-diastolic endocardial volume (EDEV) and end-systolic endocardial volume (ESEV) were decreased in the automatic segmentation, while the standard deviation for the intra-observer and inter-observer variability slightly increased. The intra-observer and inter-observer variability of the manually derived EF were already low and the automatic segmentation increased only the standard deviation of its intra-observer and inter-observer variability. For the LVM the mean difference of the inter-observer variability was decreased, whereas the intra-observer variability was increased in mean difference and standard deviation.

Discussion

We compared our results of the intra- and inter-observer variability from the manual segmentation (Table 3.1) with the mean difference values and standard deviations reported in the articles of Schneider *et al.* [69] and Ruff *et al.* [32]. The intra-observer variability of our study showed a lower or equal value for the mean differences of the different global functional parameters. The standard deviations of all the intra-observer variability in our study were higher as compared to Ruff *et al.* and Schneider *et al.* Only the standard deviation of the ESV was significantly different (> 5%) from that in the other studies.

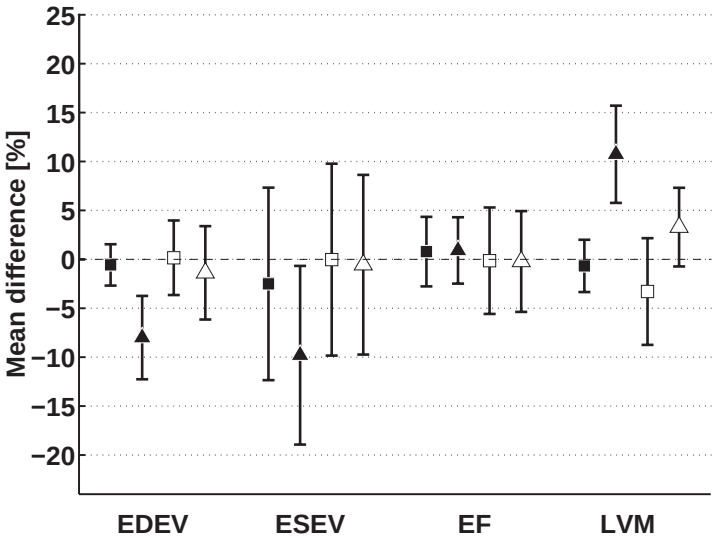

Figure 3.4: Overview of four global functional parameters derived from two manual segmentations: intra-observer variability (black squares), inter-observer variability (black triangles) and the variability of two automatic segmentations (see text) from: intra-observer data (white squares), inter-observer data (white triangles). EDEV: end-diastolic endocardial volume; ESEV: end-systolic endocardial volume; EF: ejection fraction; LVM: left ventricular mass without papillary muscles. (mean difference ± SD [%].)

Our inter-observer variability was equal or higher for the mean difference except for the EF, which was 1 or 2 percent points lower. For the inter-observer variability all standard deviations were larger as compared to Ruff *et al.* and Schneider *et al.* Only large differences ($> 5\%$) in inter-observer variability were found between our study and the study of Schneider *et al.* for the mean difference of the diastolic mass and both endocardial volumes. For the endocardial volumes also a higher standard deviation was found. We have no explanation for the fact that the standard deviation of the intra- and inter-observer variability of the end-systolic endocardial volume and the mean difference of the inter-observer variability of both endocardial volumes were so much different from the values found by Ruff *et al.* and Schneider *et al.* We know from the ratio between the endocardial surface and endocardial volume that this global functional parameter is the most sensitive to small deviations as compared to the other global functional parameters. Our image quality was comparable to the previous two studies, although Schneider *et al.* had a 1.3 lower resolution compared to our study and a higher magnetic field strength. The main difference between the present study and the other two studies was the number of mice measured: 8 and 6, for Ruff *et al.* and Schneider *et al.*, respectively, as compared to 22 in this study.

In comparison with a human study of Geuns *et al.* [125], who used the human version of

the same automatic segmentation software, the intra- and inter-observer variability were almost equal except for a very high variability of the human heart mass. In most cases, the global functional parameters of the mouse heart determined with automatic segmentation had less variability as compared to the automatic segmentation of human hearts. The human data showed a higher linear correlation between the manual and automatic segmentation for the different global functional parameters. This was probably due to the homogeneous group of mice leading to a relatively narrow range of global functional parameter values. The reproducibility of the automatic segmentation algorithm is slightly better in the human study. No explanation could be found why the standard deviations of the reproducibility analysis of the human study is so much different from the their values of the intra- and inter-observer variability while in this study the standard deviation values were comparable (see Table 3.1 and Table 3.3).
Papillary muscles were well visible in most of the CINE MR images from the equator towards the base (see Fig. 3.1). In spite of this we excluded them from the endocardial volume and EF analyses for the reason that a large inter-observer variability ($> 20\%$) for the end-diastolic papillary muscle volume was found. This led to a higher mean difference in EF ($+2.5\%$) of the inter-observer variability which became almost equal to the standard deviation. Only positive effects of including the papillary muscles were found by decreasing the mean difference of the inter-observer variability of the LVM and decreasing the intra-observer variability of the EF (not shown). An explanation for this large difference in inter-observer variability could be the lack of a good definition of the papillary muscle and secondly their high surface to volume ratio, which led to a high sensitivity to differences in the segmentation.

Conclusion

In conclusion, automatic segmentation can be used to determine global functional parameters with almost equal variability as for inter-observer manual segmentation. Nevertheless, intra-observer manual segmentation leads to the least variability in the global functional parameters. Considering the fact that manual segmentation is a time consuming method, we conclude that automatic segmentation of the mouse heart provides a fast and valid alternative to manual segmentation of the mouse heart.

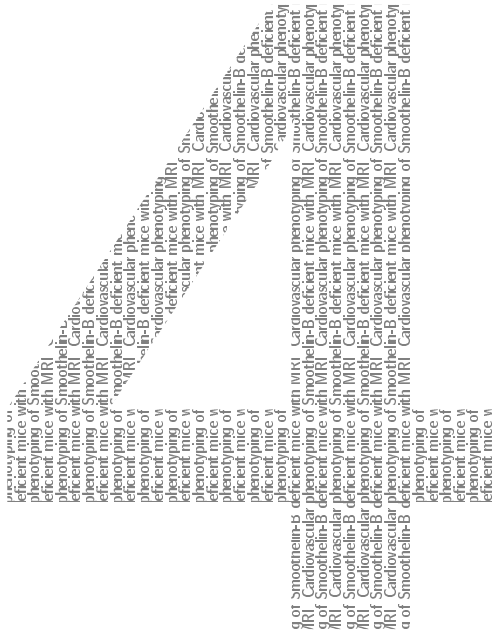

Cardiovascular phenotyping of Smoothelin-B deficient mice with MRI

Edwin Heijman[1], Petra Niessen[2], Ben Janssen[3], Jo De Mey[3], Guillaume van Eys[2], Klaas Nicolay[1] and Gustav J. Strijkers[1]

[1] Department of Biomedical Engineering, Eindhoven University of Technology, Eindhoven, The Netherlands

[2] Department of Genetics and Cell Biology, CARIM, University of Maastricht, Maastricht, The Netherlands

[3] Department of Pharmacology and Toxicology, CARIM, University of Maastricht, Maastricht, The Netherlands

Part of: Circulation. 2008 Aug 4.

Abstract

Smoothelins are actin-binding proteins that are abundantly expressed in healthy visceral (smoothelin-A) and vascular (smoothelin-B) smooth muscle. Their expression typically recedes when smooth muscle cell contractility is lost. In this study we have used a prospective CINE MRI sequence to phenotype small differences in the cardiovascular system of smoothelin-B knockout mice compared to wild-type mice (n = 11 each). The ejection fraction and the left ventricular mass of the smoothelin knockout mouse hearts were significantly different ($p < 0.02$) compared to their littermates.

Next to measurements of global functional heart parameters, we have used a retrospective CINE MRI sequence to measure circumferential stretch of the thoracic aorta, which was almost two times higher for smoothelin-B knockout mice compared with their littermates. We infer that the higher mean circumferential stretch is due to a higher systolic pressure causing a mild cardiac hypertrophy. The hypertrophy of the heart was confirmed in the smoothelin-B knockout mice by MRI and by elevated levels of atrial natriuretic factor in the myocardium. Mouse cardiac MRI showed its value for phenotyping small differences brought about by genetic engineering.

Introduction

Hypertension is common among the elderly in the Western World [126] and it gives rise to several life threatening diseases, *e.g.* stroke [127], coronary heart disease [128, 129] and heart hypertrophy [130]. Abnormal smooth muscle contractility or the humoral mechanism could be two major factors in creating hypertension. The underlying molecular regulation of smooth muscle cell contraction is poorly understood. Smoothelins are α-smooth muscle actin-binding proteins that are specifically and abundantly expressed in contractile smooth muscle cells [131–134]. They are encoded by a single copy gene that generates two major isoforms, of which smoothelin-A is most prominently expressed in visceral smooth muscle cells and smoothelin-B only in vascular smooth muscle cells [120]. A previous study of Niessen *et al.* [135] showed that smoothelin-A plays a vital role in the intestinal smooth muscle cell contraction.

Functional studies on smoothelins have been hampered by the rapid down regulation of their expression *in vitro* [131]. Therefore, mice lacking either only smoothelin-B (Smtn-$B^{-/-}$) or both smoothelin isoforms (Smtn-$A/B^{-/-}$) were generated to investigate the relevance of both isoforms for vascular smooth muscle contraction.

Measurements of the arteries of young Smtn-$B^{-/-}$ mice showed a reduced arterial contractility and relaxation and a higher mean arterial pressure (MAP) for fully-grown Smtn-$B^{-/-}$ mice compared to Smtn-$B^{+/+}$ mice.

According to literature hypertensive mice generate hypertrophy and an increased expression of atrial natriuretic factor (ANF) [136–138]. In most studies the transverse aortic constriction [139] or drugs [140] are used for creating hypertension in mice. Hypertensive knockout mice studies show also adaptations of the arteries *e.g.* the aorta [141, 142]. In this study we hypothesize that fully-grown mice deficient in smoothelin-B are adapted in the cardiovascular system compared to their littermates (Smtn-$B^{+/+}$). To test this hypothesis, the hearts as well as the lumen of the descending thoracic aorta of both groups were scanned with an MRI scanner at high field. Here we report that Smtn-$B^{-/-}$ mice hearts showed a higher ejection fraction, mild cardiac hypertrophy and a higher degree of circumferential elongation of the descending thoracic aorta during the cardiac cycle compared to Smtn-$B^{+/+}$ mice.

Methods

Generation of Smtn-$B^{-/-}$ mice

To generate Smtn-$B^{-/-}$ mice, exons 3 through 7 were targeted with a neomycin gene under the control of the thymidine kinase promoter in reverse orientation. For negative selec-

tion the targeting vector contained a thymidine kinase gene. After electroporation of the PνuII-linearized constructs into mouse L129/Sv embryonic stem (ES) cells, we selected neomycin-resistant clones with G418 (Invitrogen, Carlsbad, California) and 1-[2-Deoxy]2-fluoro-β-D-arabinofurasonyl (Invitrogen). DNA from resistant clones was screened by Southern blotting after SacI restriction digestion using 3' or 5' probes. ES cells from targeted clones were injected into C57Bl6 blastocysts and implanted into pseudopregnant C57Bl6 females. Mating of the resulting chimeric males to C57Bl6 females led to germline transmission of the targeted alleles as detected by Southern blotting. The mice were further backcrossed 4 times on C57Bl6 background prior to initiation of experiments. Since the mice had a mixed background (L129/Sv and C57Bl6), we used littermates for experimentation. Generation of Smtn-A/B$^{-/-}$ mice has been described previously [135].

MRI protocols

The examinations were performed with a 6.3 T horizontal-bore MR magnet (Oxford Instruments Superconductivity, Eynsham, Oxon, England) interfaced to a Bruker AVANCE (Bruker BioSpin MRI GmbH, Ettlingen, Germany) MR imaging console with ParaVision 3.0.2 software. The scanner was equipped with a custom made Magnex (Magnex Scientific Ltd., Yarnton, UK) gradient system (inner diameter, 12 cm; maximum gradient strength, 400 mT/m). A quadrature driven birdcage coil (Rapid Biomedical, Wrzburg, Germany) with an inner diameter of 3.2 cm was used for radio frequency (RF) transmission and signal reception. All MR sequences started with a steady-state preparation using dummy acquisitions for at least 5 seconds.

Global heart parameters were determined by acquiring short axis CINE MR images, covering the heart from apex to base. The short axis CINE MRI scans were collected with the use of a CINE FLASH [48] sequence with the following parameters: Gaussian-shaped RF-pulse, 300 μs; flip angle, 15°; repetition time, 7 ms; echo time, 2.3 ms; sample rate, 100 kHz; echo position, 30%; field-of-view, 3x3 cm^2; matrix, 192x192; in-plane resolution, 156x156 μm^2; slice thickness, 1 mm; number of averages, 6; total acquisition time, approximately 5 min. MRI scans started immediately at the up-slope of the ECG trigger pulse. The number of heart frames multiplied by the repetition time amounted to about 90% of the mean heart period as determined prior to the scan corresponding to 13-17 image frames per heart beat.

To capture the whole aortic motion during the cardiac cycle a retrospective CINE MRA sequence was chosen. A modified FLASH sequence with a navigator echo [107, 143] was used with the following parameters: Gaussian-shaped RF pulse, 300 μs; flip angle, 30°; repetition time, 5.4 ms; echo time, 2.98 ms; sample rate, 150 kHz; echo position, 40%; navigator echo points, 96; field of view, 2.5x3 cm^2; matrix, 256x192; in-plane resolution,

100x156 μm^2; slice thickness, 2 mm; number of repetitions, 700; total acquisition time, approximately 12 min. Each navigator echo contributes to the navigator signal from which cardiac triggering points and respiratory gating periods were calculated (see Chapter 2). The navigator echo and signal analyses were done with a customized program IntraGate within the ParaVision 3.0.2. software using Fourier filtering techniques [107]. Twenty CINE MRA images of the aorta motion were retrospective reconstructed equally distributed over the whole cardiac cycle.

In vivo measurements

Before the MRI examination, the mice were first weighed and then sedated in an induction chamber by inhalation of 3 vol% isoflurane in medical air at a flow rate of 0.4 l/min. When the respiration rate was slowed down to approximately 1 per second and the toe-pinch reflex was absent, the mice were transferred to a home-built cradle. A mask, which consisted of two concentric Perspex tubes, was used to supply anesthesia gas. The inner tube delivered the isoflurane (1.5 vol% in medical air; flow rate, 0.4 l/min), while the outer tube removed the excess gasses. To keep the body temperature constant, the mouse was positioned on a Perspex pad that was circulated with heated water from a Lauda RE 204 heating bath (Lauda, Lauda Knigshofen, Germany). The mice were positioned supine on the warming pad with their head loosely fixed in the anaesthesia mask. For ECG monitoring and cardiac triggering EEG paste (TEN20 from D.O. Weaver and Co., Aurora, CO USA) was put on the front paws to achieve good electric conductivity between the animal and the ECG unit (combined ECG and respiratory unit from Rapid Biomedical, Rimpar, Germany). The paws were then fixed on small copper ECG electrodes with the use of medical tape. During the examination the respiration rate was continuously measured with a balloon pressure sensor connected to the ECG/respiratory unit. The isoflurane concentration was adjusted to keep the respiration rate between 75 and 100 respirations/min. A rectal temperature sensor monitored the body temperature of the mouse and an extra temperature sensor was placed between the mouse and the heating pad (Luxtron M3300 fluoroptic thermometers, Santa Claren, CA USA). The body temperature of the mouse was kept at 37°C during the whole examination. The ECG, respiration and temperature signals were recorded continuously by a PC data acquisition board (National Instruments model PCI-6013, Austin, TX USA), stored and visualized by an in-house developed LabView program (National Instruments, Austin, TX USA).
C57Bl6 mice (age 8 months) divided in two groups of 11 genotype Smtn-$B^{+/+}$ mice and 11 genotype Smtn-$B^{-/-}$ mice were scanned to determine global heart parameters. At the start of each examination several scout images were made in the transverse plane and the long-axis plane of the left ventricle to determine the orientation of the short axis.

The location of the whole dataset was planned between the apex and base during the begin-diastole heart phase.
From seven Smtn-$B^{+/+}$ mice and five Smtn-$B^{-/-}$ mice their thoracic aortic arch were also scanned from the ascending aorta to the descending aorta. The orientation and position of the aortic arch during the cardiac cycle was found by using the above scout images and an extra set of multi-slice gradient echo images for finding the top of the arch and its transversal rotation. The slice was planned in such a way that during the cardiac cycle the aorta stayed within the image slice. A prospective CINE MRA acquisition with almost equal MR parameters as the retrospective MRA method was acquired to test the orientation parameters and to determine the in-plane rotation for setting the readout direction orthogonal to the descending thoracic aorta. This orientation of the readout direction was chosen to reduce potential image artefacts perpendicular to the aorta caused by phase errors of the flowing blood. With the tested orientation parameters a retrospective MRA was acquired.
Each mouse was actively euthanatized by O_2/CO_2 within one week after the measurements. The hearts were dissected and cleaned with physiological salt solution. The hearts were then weighed on a micro balance and frozen.

The Animal Care Committee of Maastricht University (Maastricht, the Netherlands) approved the experimental protocol.

Quantitative real-time PCR

Total RNA was extracted from the mouse hearts with Tri reagent (Sigma-Aldrich, Zwijndrecht, The Netherlands). Expression of atrial natriuretic factor (ANF) [136] and brain natriuretic peptide (BNP) [144] was investigated by quantitative real-time PCR (qRT-PCR) using the ABI Prism 7700 System (Perkin Elmer, Norwalk, Connecticut). Applied primers for ANF, BNP and cyclophillinA are listed in Table 4.1. The transcript was used to normalize the amount and quality of the extracted RNA (Table 4.1). Smtn-$B^{+/+}$ expression levels were set at 1.

Table 4.1: Oligonucleotide sequence of primers used for qRT-PCR.

Gene	Forward Primer 5'-3'
ANF	CATCATGGGCTCCTTCTCCAT
BNP	AGGACCAAGGCCTCACAAAA
CyclophillinA	TTCCTCCTTTCACAGAATTATTCCA

Image analysis

Global left ventricular parameters end-diastolic volume (EDV), end-systolic volume (ESV), stroke volume (SV), end-diastolic left ventricle mass (LVM), cardiac output (CO) and ejection fraction (EF) of the 22 mice were calculated by manual segmentation performed in the program FARM MRV CAAS provided by Pie Medical Imaging (Maastricht, The Netherlands). Left ventricle blood volume was not corrected for the papillary muscle volumes to minimize the manual segmentation error (see Chapter 3 "Discussion"). The left ventricular mass was obtained by multiplying the left ventricular wall volume with 1.04 g/cm^3 [29]. The LVM was calculated by taking the mean of the left ventricle volume at the end-diastolic and end-systolic heart phases. To determine the lumen diameter of the descending thoracic aorta the retrospective CINE MRA images were first zero-filled to a matrix of 512x512 pixels for decreased pixel dimensions and increased contrast by interpolation [145, 146]. From the enhanced CINE MRA images the lumen diameter of the descending thoracic aorta was measured at every heart phase at a fixed height (*e.g.* the white bar in Fig. 4.4). The circumferential stretch per heart phase was determined by:

$$S_c = \frac{d_l - min(d_l)}{min(d_l)} 100\% \tag{4.1}$$

With $min(d_l)$: minimum lumen diameter [mm],
(d_l) : actual lumen diameter [mm].

Also the maximum circumferential elongation ($E_{C,max}$ [mm]) of the aorta in each mouse group was determined by subtracting the minimal diameter from the maximal lumen diameter.

Statistical analysis

Statistical significance was calculated by two-tailed paired Student's t-tests using Microsoft Excel 2003 software. Groups were considered significantly different for $p < 0.05$. Physiological data and global functional parameters were expressed as mean ± standard deviation and aorta values as mean ± standard deviation (SD).

Results

All mice were successfully measured. During the MRI acquisitions the respiratory rate and heart rate of the mice were kept between 75 to 100 respirations/min and between 460 and 600 beats/min, respectively. Figure 4.1 and 4.2 show two examples of CINE MR images of a short-axis slice through the equator of a Smtn-$B^{+/+}$ and Smtn-$B^{-/-}$ mouse heart, respectively. The different heart phases in both image series are starting at begin-systole in image 1 and ending with almost end-diastole in image 16. The transition from end-systole to begin-diastole is probably between the images 6 and 7 in both series. It seems that the Smtn-$B^{-/-}$ mouse (Fig. 4.2) has a mild hypertrophied heart compared to the Smtn-$B^{+/+}$ mouse (Fig. 4.1).

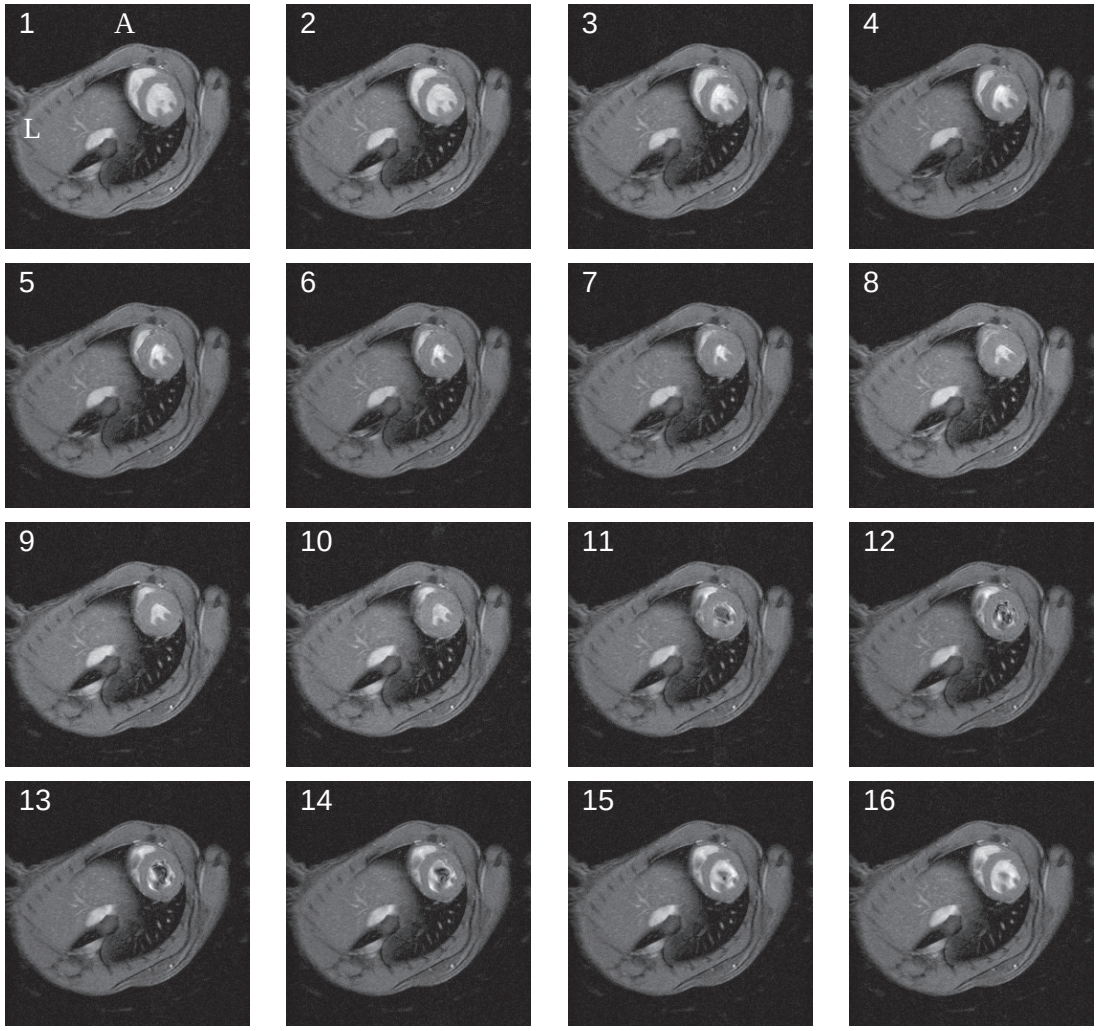

Figure 4.1: CINE short-axis MR images of a Smtn-$B^{+/+}$ mouse heart at the equator of the heart from begin-systole (1) to end-diastole (16).

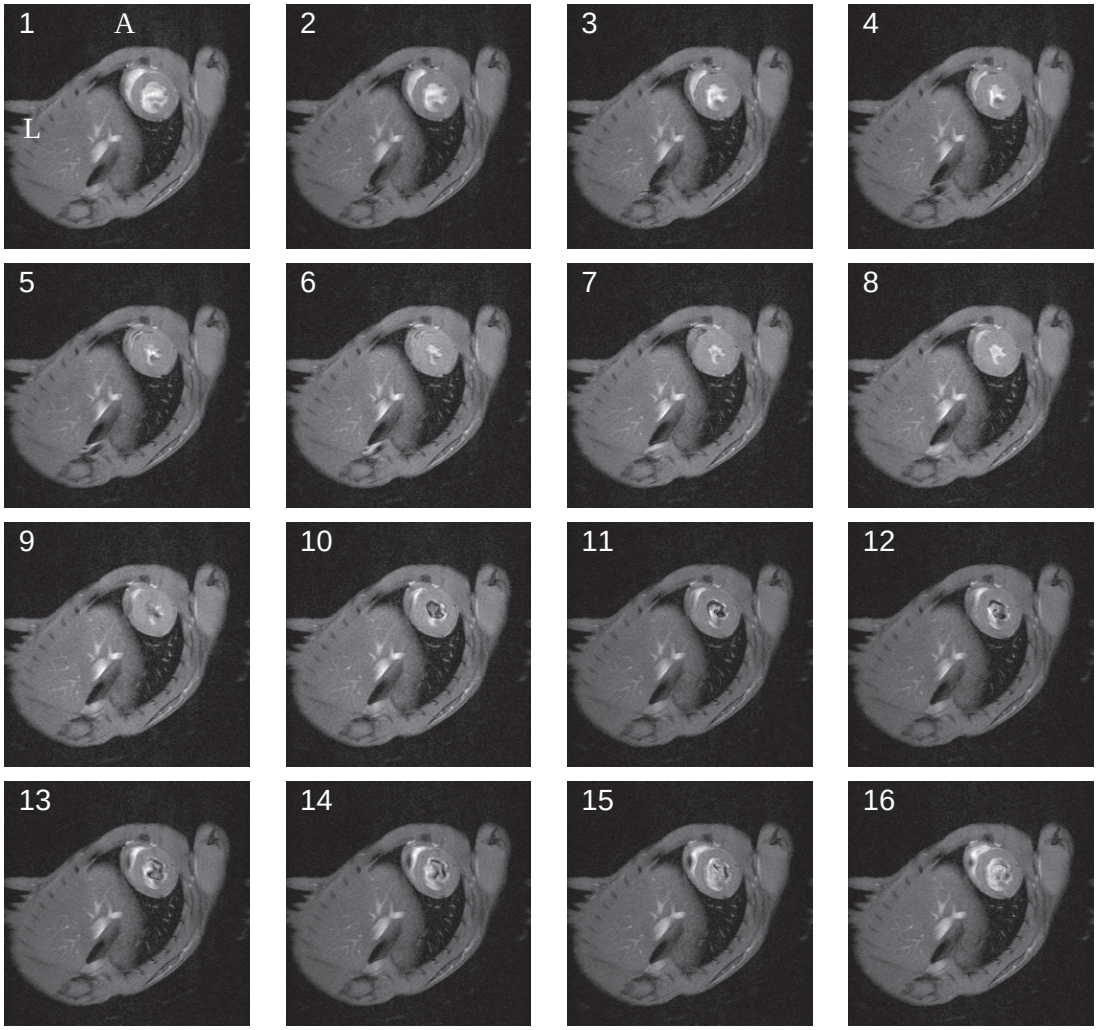

Figure 4.2: CINE short-axis MR images of a Smtn-B$^{-/-}$ mouse heart at the equator of the heart from begin-systole (1) to end-diastole (16).

Physiological data and global functional parameters are summarized in Figure 4.3. Body weight ($p = 0.82$), heart rate ($p = 0.65$), SV ($p = 0.94$) and CO ($p = 0.76$) were not significantly different between the Smtn-B$^{+/+}$ and Smtn-B$^{-/-}$ mice. Almost significant differences were found for the EDV ($p = 0.39$) and ESV ($p = 0.071$). Significantly different were the ED LVM ($p = 0.02$) and EF ($p = 0.02$). The significant difference in the ED LVM was confirmed by the total heart weight: 0.14 ± 0.01 g and 0.16 ± 0.01 g for the Smtn-B$^{+/+}$ and Smtn-B$^{-/-}$ mice ($p = 0.045$), respectively. The mean values of the global indices EDV, ESV, SV and EF were comparable with values reported in two previous studies of Franco *et al.* [29] and Kober *et al.* [110], who used mice of comparable age and body weight.

Figure 4.4 shows a retrospectively reconstructed MRA image of the aorta at the end-diastolic heart phase of a Smtn-B$^{+/+}$ mouse. For the analyses of the navigator echo the

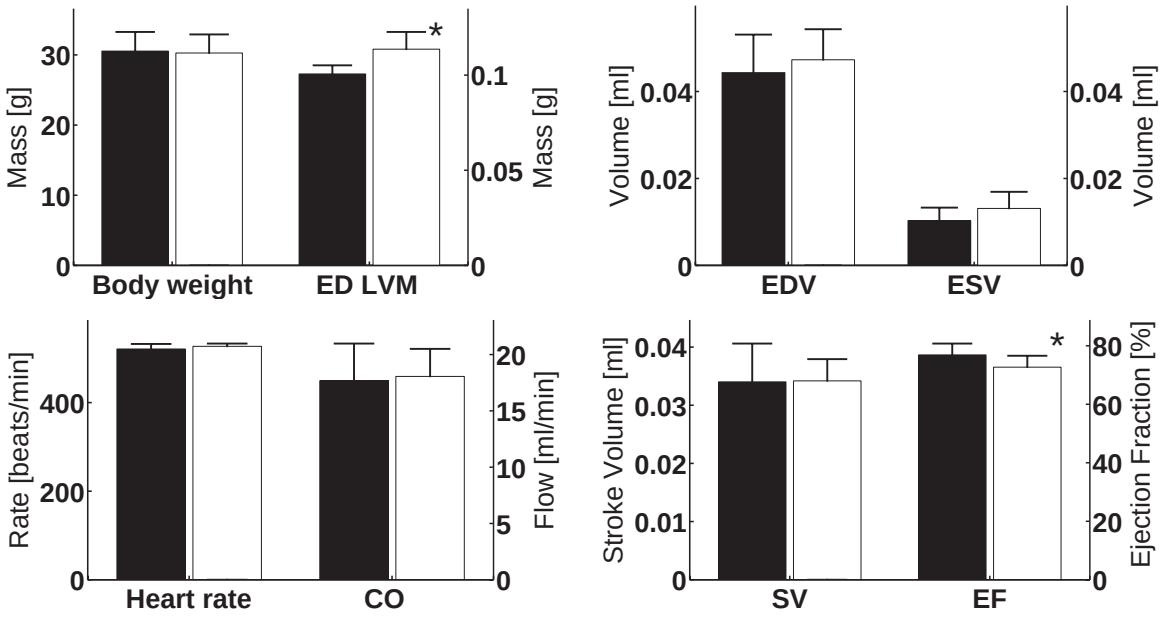

Figure 4.3: A comparison (mean ± SD) of physiological data and global functional parameters of the left ventricle between Smtn-$B^{+/+}$ (black bar) and Smtn-$B^{-/-}$ mice (white bar). Upper left: body weight and end-diastolic left ventriclar mass (ED LVM) based on CINE MR images. Upper right: EDV and ESV both based on CINE MR images. Lower left: mean heart rate during the MRI measurements and CO based on CINE MR images. Lower right: SV and EF both based CINE MR images. (* $p < 0.05$).

best navigator signal [107] was chosen by an expert. The navigator signal was frequency selective filtered with values of 450 to 1000 beats/min and 30 to 50 respirations/min for the heart and respiratory cycle, respectively. The window width for respiratory gating was set around 40% of the total respiratory period which was also used on the ECG unit for the prospective measurements. All twenty CINE MRA images were synchronized by shifting the MRA image at begin-systole to the first position in the CINE series. The MRA image at begin-systole could be found as the first image where the blood was pushed from the heart into the ascending aorta causing a flow artefact. The white line in Figure 4.4 shows the position where the lumen diameter was measured during the whole cardiac cycle. The end-diastolic phase of the lumen diameter was determined as the point in the cardiac cycle at which the lumen diameter was at its minimum. The end-diastolic phase of the aorta was found in the first image of the synchronized CINE MRA series in 8 cases and in the last image of the CINE MRA series in 4 cases.

The lumen diameter of the thoracic aorta at the end-diastolic (ED) heart phase was 1.15 ± 0.15 mm and 1.05 ± 0.17 mm for the Smtn-$B^{-/-}$ and Smtn-$B^{+/+}$ mice, respectively. In Figure 4.5, the mean circumferential stretch of the thoracic aorta of both mouse groups is plotted after normalization to the minimal lumen diameter in every time frame. It

Figure 4.4: MR angiography of the aorta of a Smtn-$B^{+/+}$ mouse at the end-diastole heart phase. The white line indicates the position where the diameter measurement of the descending thoracic aorta was performed.

is clearly visible that the mean circumferential stretch was higher for the Smtn-$B^{-/-}$ mice compared to the Smtn-$B^{+/+}$ mice. Maximum circumferential stretch was reached at approximately the same phase of the cardiac cycle. The maximal elongation of the lumen diameter of the thoracic aorta was higher for the Smtn-$B^{-/-}$ mice compared with the Smtn-$B^{+/+}$ mice (see Figure 4.5). Division of the maximal elongation of the lumen diameter by the ED lumen diameter resulted in a maximal circumferential stretch of 39.8 $\pm$ 6.3% for Smtn-$B^{-/-}$ mice and 19.8 $\pm$ 6.3% for Smtn-$B^{+/+}$ mice ($p = 0.014$).
In view of the elevated MAP and possibility of hypertrophy, RNA levels of the cardiac hypertrophy markers ANF and BNP were measured. The relative expressions of both natriuretic peptides were elevated (ANF: 1.39 $\pm$ 0.16 ($p = 0.05$), BNP: 1.22 $\pm$ 0.07 ($p = 0.08$)) in Smtn-$B^{-/-}$ mice compared with Smtn-$B^{+/+}$ littermates (ANF: 1.00 $\pm$ 0.15, BNP: 1.00 $\pm$ 0.13).

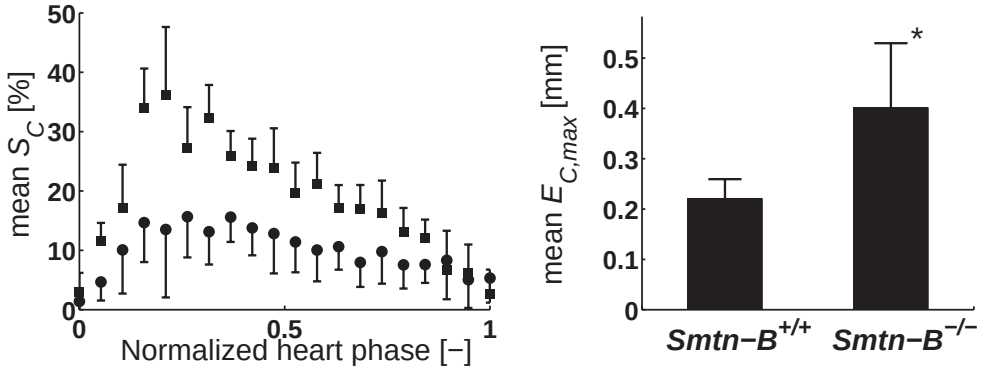

Figure 4.5: Left: Mean circumferential stretch (mean ± SD) of Smtn-B$^{+/+}$ (dots) and Smtn-B$^{-/-}$ mice (squares) during the normalized cardiac cycle with 0 at the begin-systolic heart phase and 1 at the end-diastolic heart phase. Right: Comparison of the maximal circumferential elongation (mean ± SD) of the descending thoracic aorta of Smtn-B$^{+/+}$ and Smtn-B$^{-/-}$ mice during the cardiac cycle. ($*$ p $<$ 0.05).

Discussion

This study demonstrates that prospective and retrospective CINE MRI methods can be used for detecting small differences in the cardiovascular system of smoothelin-B knock-out mice. The quality of the prospective CINE MR images of the heart is comparable to that in studies of Franco, Brede and Wilding [29, 30, 36, 37] who also used MRI to phenotype mice. The measured values for the EDV, ESV and EF were comparable with values reported in two previous studies of Franco *et al.* [29] and Kober *et al.* [110], who used mice of comparable age and body weight.

The major limitation of measuring dimensions or volumes of soft tissues *in vivo* is the lack of a gold standard from which the accuracy can be determined. Only statistical compa - risons can be made for determining the real value or validity of the measurement method and image analysis procedures. The problem is that the standard deviations or standard errors of means of global functional parameters are a combination of differences between individuals and the measurement uncertainty/error. Performing a manual segmentation by one observer is the most valid method of determining global functional parameters and the EF was determined to be the global functional parameter with the smallest mean variability of the interobserver and intraobserver variability (see Chapter 3). This explains why a significant difference is more easily detected for the EF than for EDV and ESV.

The difference in elongation of the lumen of the thoracic aorta between Smtn-B$^{-/-}$ mice and Smtn-B$^{+/+}$ mice was significant. However, the temporal resolution of the measurement method is limited as evident in the left figure of Figure 4.5 from the high standard deviation at the maximum circumferential stretch and the non zero values of the circumferential stretch at the beginning and end of the normalized cardiac cycle. The number of

retrospectively reconstructed time frames could be increased to solve the latter issue, but this would decrease the contrast to noise ratio (CNR) and increase the standard deviation due to a less accurate reading of the lumen edge by the observer. To compensate this, more averages would be needed which increases the acquisition time. Nevertheless, the balance between CNR and temporal resolution can be further optimized.
The elevated ANF levels as well as the higher ED LVM of Smtn-$B^{-/-}$ mice indicated a higher mean arterial pressure compared to the Smtn-$B^{+/+}$ mice. This would imply that Smtn-$B^{-/-}$ mice have a higher systolic blood pressure, which could explain the observed increase in mean circumferential stretch of thoracic aorta. One could argue that the control of the blood pressure is lost when isoflurane is used as anesthetic [147, 148], but this would probably have resulted in large differences (and thus high standard deviations) in the circumferential stretch among the 7 Smtn-$B^{+/+}$ mice. This was clearly not the case (see Figure 4.5). Tight control of the respiration rate, which is an indicator of the depth of the anesthesia, and of body temperature can probably decrease the influence of the isoflurane on the blood pressure [148, 149]. It was confirmed by additional pulse wave velocity measurements, using a pressure sensor in the aorta at two different positions, that the stiffness of the aorta was not significantly different between Smtn-$B^{-/-}$ mice and Smtn-$B^{+/+}$ (data not shown in this chapter). The latter findings strengthen the thought that the end-systolic pressure in the aorta is higher in Smtn-$B^{-/-}$ than in Smtn-$B^{+/+}$, leading to a higher dilatation of the aorta. This will increase the mean arterial pressure leading to the mild increase in the expression of ANF.

Conclusions

We conclude that smoothelin-B deficiency in mice results in an increased mean circumferential stretch of the thoracic aorta, increased ED LVM and decreased EF compared to the wild-type situation. In this study, mouse cardiac MRI showed its value for phenotyping small functional differences between genetically engineered mice.

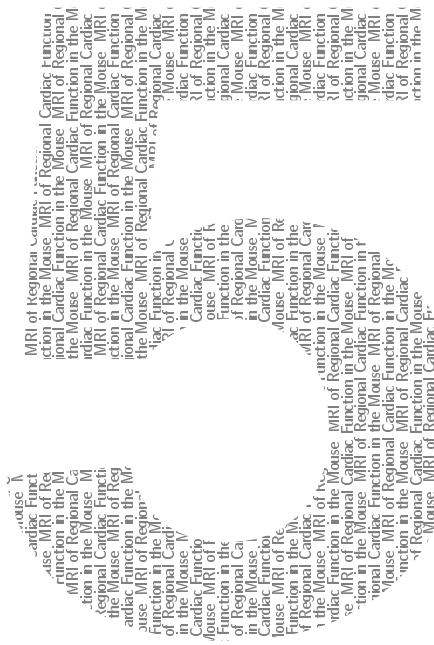

MRI of Regional Cardiac Function in the Mouse

Edwin Heijman[1], Gustav J. Strijkers[1], Jo Habets[1], Ben Janssen[2] and Klaas Nicolay[1]

[1] Biomedical NMR, Department of Biomedical Engineering, Eindhoven University of Technology, Eindhoven, the Netherlands

[2] Department of Pharmacology and Toxicology, Cardiovascular Research Institute Maastricht, Maastricht University, Maastricht, the Netherlands

Published: MAGMA. 2004 Dec;17(3-6):170-8

Abstract

In this chapter we introduce an improved HARP analysis of CSPAMM tagging data of the mouse left ventricular wall, which enables the determination of regional displacement fields with the same resolution as the corresponding CINE anatomical images. CINE MRI was used to measure the global function, such as the ejection fraction. The method was tested on two healthy mice and two mice with a myocardial infarction, which was induced by a ligation of the left anterior descending coronary artery. We show that the regional displacement fields can be determined. The mean circumferential strain for the left ventricular wall of one of the healthy mice was 0.09 ± 0.04 (mean SD), while for one of the infarcted mouse hearts strains of 0.02 ± 0.02 and 0.10 ± 0.03 were found in the infarcted and remote regions, respectively.

Introduction

Myocardial infarction following cardiovascular disease is one of the major causes of death in western societies [150, 151]. To improve the diagnostics and the evaluation of treatment of these diseases there is a great need for non-invasive, high-resolution imaging techniques. Magnetic Resonance Imaging (MRI) offers an extensive set of tools to assess both the global and local morphology and function of the heart in a non-invasive manner [152] and therefore plays an increasingly important role in the clinical management of cardiovascular disease and in basic research on disease etiology and therapeutic options. Global functional indices of the heart, *e.g.* myocardial mass, end-diastolic volume, end systolic volume and ejection fraction, can be measured using CINE MRI [153–156]. Regional tissue viability can be assessed with perfusion MR, *e.g.* using arterial spin labeling techniques [157], or from the delayed enhancement effect following gadolinium diethylenetriamine penta-acetic acid (Gd-DTPA) injection [158]. Phase velocity [64] and tagging techniques [16, 17, 59, 159] are able to measure local wall motion and muscle fiber shortening, which provide important insights in local tissue function. The metabolic state of the heart tissue can be determined using ^{31}P-, ^{13}C-, or ^{13}Na-Magnetic Resonance Spectroscopy (MRS) [74, 160, 161], or by MRI measurements of the local influx of Mn^{2+}, which acts as a MRI contrast agent and can be considered a calcium analogue [53].
In vivo studies in animal models are indispensable to gain an improved understanding of the pathophysiological processes leading to myocardial infarction and to develop diagnostic tools as well as therapeutic interventions. In recent years the mouse has become the animal of choice in studies of many aspects of cardiovascular diseases, which is largely due to the large number of transgenic and knock-out mice that has become available. The significant added value of MRI for studying murine models of cardiovascular disease processes, including atherosclerosis [162–166], cardiac hypertrophy [29], and myocardial infarction [38, 96, 167–169](25-30) is well established.
In this chapter we will present global and regional MRI measurements of left ventricle (LV) cardiac function of healthy mice and mice with a left anterior descending (LAD) coronary artery occlusion, using CINE imaging and MRI tagging. In a number of previous studies it was argued that velocity encoding is more suitable for determining regional contractility of the mouse heart than MRI tagging, because of superior resolution and the possibility to measure three-dimensional displacements [61, 64, 170–172]. 3D CSPAMM [173] is already tested in humans. However, in this chapter we demonstrate that the use of MRI tagging based on the 2D CSPAMM technique, in combination with the harmonic phase (HARP) analysis method [173, 174], yields accurate information on regional mouse cardiac function with the same spatial resolution as the parent magnitude images.

Methods

Mouse preparation

Four FVB mice (age, 18-20 wks; weight, 20-23 g) were examined. In 2 mice myocardial infarction was induced by ligating the left anterior descending (LAD) coronary artery four days before the examination, using published procedures [175].
For MRI studies, the mice were first sedated in an induction chamber by exposure to 3 vol% isoflurane in medical air at a flow rate of 0.4 l/min. When the respiration rate was slowed down to approximately 1.4 per second and the toe-pinch reflex was absent, the mice were transferred to a home-built support unit. A mask, which consisted of two concentric Perspex tubes, was used to supply anesthesia gas. The inner tube delivered the isoflurane (1.5 vol% in medical air; flow rate, 0.4 l/min), while the outer tube removed the excess gasses. To keep the body temperature constant, the mouse was positioned on a Perspex pad that was circulated with heated water. The mice were positioned supine on the warming pad with their head loosely fixed in the inner anesthesia tube. For electrocardiogram (ECG) monitoring and triggering ultrasound gel (Parker Laboratories, Fairfield, NJ) was put on the front paws to achieve a good electric conductivity between the animal and the ECG unit (combined ECG, respiration, and temperature monitoring unit from Rapid Biomedical, Wrzburg, Germany). The paws were then fixed on copper ECG electrodes with the use of medical tape.
During the examination the respiration rate was continuously measured with a balloon pressure sensor connected to the ECG unit. The isoflurane concentration was adjusted to maintain the respiration rate within the range of 1.0 to 1.6 s^{-1}. A rectal temperature sensor (Pt100) was connected to the ECG unit and used to monitor the core temperature. The ECG, respiratory and temperature signals were continuously recorded from the ECG unit by a data acquisition PC board (National Instruments model PCI-6013, Austin, TX).

The Animal Care Committee of Maastricht University (Maastricht, the Netherlands) approved the experimental protocol.

MRI protocols

The examinations were performed with a 6.3 Tesla horizontal-bore MR magnet (Oxford Instruments Superconductivity, Eynsham, Oxon, England) interfaced to a Varian (Varian Palo Alto, CA) VXR-S MR Imaging console (VNMR software 6.1B). The scanner was equipped with a Magnex gradient system (inner diameter, 9.5 cm; maximal gradient strength, 380 mT/m; rise time to full amplitude, 150 μs). A quadrature driven birdcage

coil (Rapid Biomedical, Rimpar, Germany) with an inner diameter of 3.2 cm was used for RF transmission and signal reception.
All MRI scans were collected with the use of a CINE gradient-spoiled gradient echo sequence with the following parameters: Gaussian-shaped RF-pulse, 400μs; flip angle, 30°; repetition time, 10 ms; echo time, 1.3 ms; acquisition window, 1.28 ms; field-of-view, 2.56x2.56 cm^2; matrix, 128x128; in-plane resolution, 200x200 μm^2; slice thickness, 1 mm; number of averages, 16. MRI scans started immediately at the up-slope of the ECG trigger pulse. The heart cycle was sampled with 10 to 12 images.
At the start of each examination several scout images were made in the transverse plane and the long-axis plane of the left ventricle to determine the orientation of the short-axis. The location of the central short-axis slice was planned half way between the apex and base. Global cardiac function was next measured with a single-slice short-axis CINE sequence. By alternatingly scanning a slice above and below the central slice, the whole heart was covered within 7 slices.
Tagged MR images were measured to determine the circumferential strain as a regional cardiac function parameter. For tagging, the imaging sequence described above was preceded by a Complementary SPAtial Modulation of Magnetization (CSPAMM) [176] preparation (Fig. 5.1). The CSPAMM consisted of two Gaussian RF pulses, with a flip angle of 45° each and pulse width of 200 μs. A maximum total flip angle of 90° was chosen to simplify the analyses of the CSPAMM images. The transversal phase of the last RF pulse was either 0° or 180°, which inverted the longitudinal modulation of the tag lines. The wavelength and the orientation of the tag lines were defined by a 200 μs gradient blip between the two RF pulses. After the second RF pulse the transversal magnetization was dephased by a crusher gradient. The total duration of the CSPAMM tagging preparation was 1 ms. The wavelength of the taglines was 6 pixels. The tag lines were imaged with a reduced matrix of 32 k-lines in the phase-encoding direction to reduce scan time. This can be done at no cost to the resolution, since for the tagging the resolution is determined by the number of points in the read-out direction. The read-out direction was sampled with 128 points and was positioned perpendicular to the tag lines. The total MR tagging acquisition consisted of 5 different image acquisitions. First an anatomical image was made, which was used for segmentation of the left ventricular wall. This was followed by two CSPAMM measurements with horizontal and vertical tag lines, respectively. Each CSPAMM acquisition comprised two acquisitions, in which the transversal phase of the second RF pulse in the CSPAMM preparation was either 0° or 180° (Fig. 5.1). The total MR tagging acquisition time, for one slice, was one hour. Three short-axis slices were measured.

Analysis of the CINE images

The global myocardial functional parameters end-diastolic (EDV) and end-systolic volumes (ESV) were determined by counting the pixels within the left ventricular cavity for all slices in the same cardiac phase. These numbers were tabulated and multiplied by the voxel area (4×10^{-2} mm^2). Summation of all the slices in the same cardiac phase and multiplication by 1 mm slice thickness resulted in the heart volume through the cardiac cycle. The end-diastolic and end-systolic heart phases were assumed to correspond to the CINE frames with the maximal and minimal left ventricular cavity volume, respectively. A threshold algorithm was used to create a binary image of the left ventricular cavity after the left ventricular wall was first selected as a region of interest. Because of the inhomogeneities of the RF coil and the transient state of the longitudinal magnetization, the signal intensities of the blood and myocardial wall varied for different slice positions and heart phases. All the images were therefore normalized to the intensity of the dorsal muscle to be able to apply the same threshold value for all slices. Pixels in the normalized images that were located within the left ventricular cavity or adjacent to the ventricular wall and that had a low intensity due to fast flowing blood were included in the binary. The left ventricular wall volume was determined according to the method of Franco *et al.* [29]. The circumference of the left ventricular cavity, the endocardial border, was automatically determined using the threshold algorithm described above. Because of the

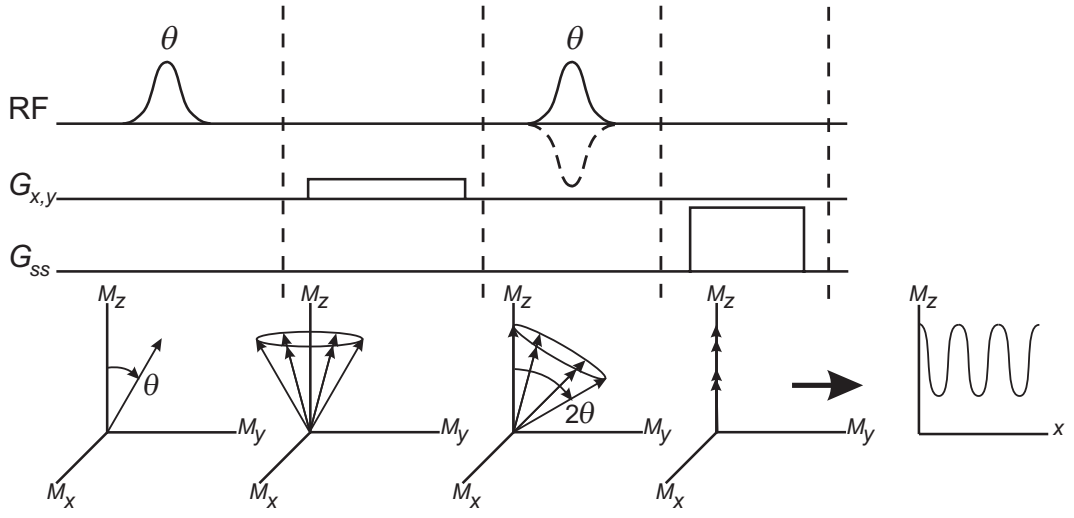

Figure 5.1: The Complementary SPAtial Modulation of Magnetization (CSPAMM) tagging sequence. For tagging in the x- or y-direction, a pair of RF pulses (flip angle θ) separated by a tagging gradient (G_x or G_y, respectively) generates a modulation of the longitudinal magnetization (M_z) along the x-axis or y-axis. A crusher gradient (G_{ss}) is added to spoil the transversal magnetization (M_x, M_y). To obtain two complementary tagging grids, the transversal phase of the second RF pulse is either 0° or 180°.

low contrast between the myocardial wall and the chest wall, the epicardial border was segmented manually. Multiplying the left ventricular wall volume with 1.04 g/cm^3 [29] gave the left ventricular mass. The left ventricular mass was calculated for all heart phases. The following parameters were calculated from the above measured EDV, ESV and left ventricular wall volume: stroke volume, ejection fraction, cardiac output [2] and left ventricular mass [29]. The functional parameters EDV and ESV were also determined using a manual segmentation of the left ventricular cavity. The papillary muscles were not included in the analysis.

HARP analysis

The HARmonic Phase (HARP) analysis was based on the method described by Osman *et al.* [177]. First the two k-space data sets of the CSPAMM acquisitions with horizontal tag lines were subtracted from each other. The same was done for the acquisitions with tag lines in the vertical direction. The resulting data sets were multiplied by a bandpass filter to isolate the CSPAMM convoluted image information. The bandpass filter had a cylindrical shape with its axis on the CSPAMM frequency. The filter was rotated 90 degrees around the centre of k-space for the vertically tagged images. To prevent ringing or loss of tag information, the bandwidth of the filter was chosen to be 20 pixels. Once the CSPAMM frequencies were determined for the first horizontally and vertically tagged images, the same filters were used for all the successive time frames. From these filtered k-space data, HARP images were obtained by inverse Fourier transformation after which the phase in every pixel was calculated.

All pixels in the left ventricular wall that had been manually selected in the first CINE anatomical image were tracked throughout the cardiac cycle. The starting coordinates of the tracked points were the pixel positions in the anatomical image. Two HARP values were obtained from the first horizontal and vertical HARP images for each tracked point. In the next time frame the HARP images were locally unwrapped in an area 1.5 times the CSPAMM wavelength. The pixel quadrant with the new point position was readily identified by matching the horizontal and vertical HARP values. Next, the new point coordinates in the new pixel quadrant were locally interpolated by fitting two surfaces, through the four points of the quadrant with the horizontal and vertical HARP values. From all the tracked points, only those which remained within the left ventricular wall, based on a segmentation of the anatomical images, were included in the analysis of the circumferential strain (E_{cc}).

The local strain in a tracked point was determined by taking the filtered displacement derivative in Cartesian coordinates. With these derivatives the Lagrange strain [177] was calculated. A cylindrical coordinate system of the left ventricle was defined by determin-

ing the midpoint of the left ventricular wall in the first CINE anatomical image. The circumferential strain was extracted from the transformation of the Lagrange strain from the Cartesian to the cylindrical coordinate system. The CINE analyses, the HARP analyses and the calculation of the strains were done using Matlab 6.1 (The Mathworks, Inc., Natick, MA).

Results

In the first part of the study it was found that the mouse heart rate was sensitive to the body temperature. The heart rate became also unstable over time, when the body temperature was not maintained around 37°C. Because of this, the mice had a relative large variation in heart rate throughout the examination: for the control animal the heart rate ranged from 520 to 600 beats/min, and for the infarct mouse from 428 to 492 beats/min. To decrease the examination time, we only used ECG triggering and turned the respiratory gating off. The results are shown in Figure 5.2. Almost no artifacts due to respiratory motion were observed in the noise of the images. The total acquisition time now became 7 min for a single-slice CINE series, while amounting to circa 13 min with respiratory gating on. The global myocardial functional parameters for the healthy mouse and infarcted mouse are shown in Table 5.1. The comparison of the above values is indicative of the compromised cardiac function induced by the focal infarction and corresponds to data measured in conscious mice using direct flow measurements at the ascending aorta [147].

Table 5.1: Global myocardial functional parameters from control and infarcted mouse heart as determined from short axis CINE images. EDV: end-diastole volume; ESV: end-systole volume; SV: stroke volume; EF: ejection fraction; CO: cardiac output; LV: left ventricular.

	EDV [μl]	ESV [μl]	SV [μl]	EF [%]	CO [ml/min]	LV mass [mg]†
Control	63	21	42	66	23	112 ± 9*
Infarcted	64	38	27	41	12.2	149 ± 6**

† Shown as mean ± SD, for: *n = 10 heart phases; **n = 12 heart phases.

Next, MRI tagging experiments were performed to determine regional cardiac function. To reduce the heart rate fluctuations caused by the body temperature variation during the experiments, both mice were kept at a body temperature of 37.4°C ± 0.5°C. The heart rate for the healthy mouse was ranging from 467 to 477 beats/min during the whole acquisition. The infarcted mouse had a larger heart rate fluctuation of 500 to 590 beats/min.

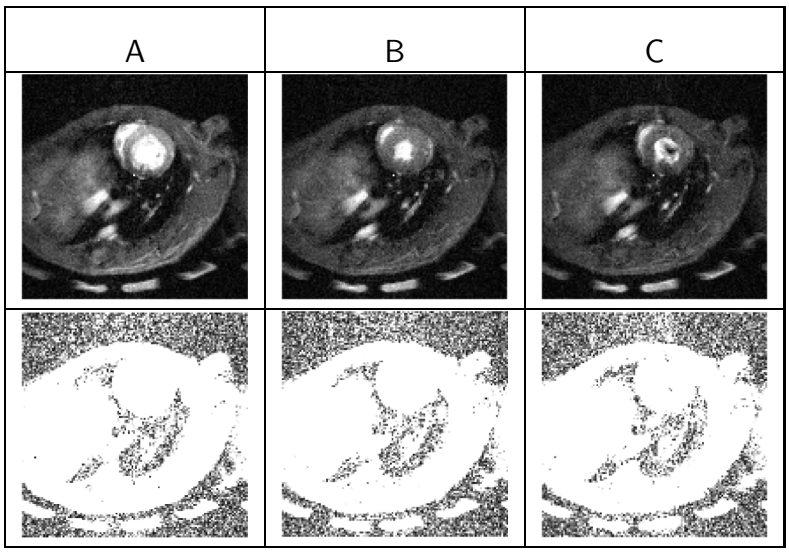

Figure 5.2: (Top) Short-axis images of the left ventricle of healthy mouse heart at end-diastole (A), end-systole (B) and during rapid filling (C). (Bottom) The same images as the top row with decreased maximum value of the intensity range to reveal potential low-level artifacts. The phase-encoding gradient was applied in the vertical direction.

In Figure 5.3 the data of the tagging procedure is shown. In the top row the subtracted horizontal tagged CSPAMM images are represented. The image of the healthy mouse (Fig. 5.3A) was rotated 45 degrees counter clockwise to have approximately the same anatomical orientation as the other two images. For the infarcted mouse heart two slices were acquired for comparison, one within the infarcted region (Fig. 5.3B) and one above these region (Fig. 5.3C). Both regions were planned on the basis of the CINE MRI images. Histology (data not shown) showed that the regions were correctly chosen, retrospectively. The bottom row of Fig. 5.3 shows the calculated circumferential strains overlaid on top of the anatomical CINE images. A large difference in circumferential strain was found between the healthy (Fig. 5.3A) and the infarcted mouse heart (Fig. 5.3B), where the latter had a high circumferential strain gradient in the apical inferoseptal region. This atypical contraction pattern in this part of the myocardium was also evident from the assessment of the CINE CSPAMM images. The circumferential strain in the slice above the infarction (Fig. 5.3C) was higher than the values observed at a similar slice position in the healthy mouse.

Figure 5.4 shows a more global analysis of the strain data by separating the left ventricular wall in octants. The resulting mean circumferential strain of each octant is plotted as function of time for healthy (dotted lines), infarcted (solid lines) and remote (dashed lines) regions. For the infarcted heart octants 3 to 6 in the left ventricular free wall appeared hypokinetic compared to the healthy heart, while remote regions in the septum

were hyperkinetic. The mean circumferential strain of the total slice through the left ventricular wall of the healthy mouse heart and the infarct slice and remote slice for the case of the infarcted mouse heart, are presented in Table 5.2.

Table 5.2: Mean circumferential strain of the left ventricular wall for different regions from control and infarcted mouse heart.

Region		Mean circumferential strain[†]
Control		$0.09 \pm 0.04^{*}$
Infarcted:		
	Infarct slice	$0.02 \pm 0.02^{**}$
	Remote slice	$0.10 \pm 0.03^{***}$

[†] Shown as mean ± SD, , for tracked points: *n = 274; **n = 350; ***n = 337 (n = number of pixels).

Discussion

The primary goal of this study was to show that MRI tagging, combined with HARP analysis, enables the detailed analysis of the regional function of the mouse heart. This was demonstrated for healthy and infarcted mouse hearts. MRI tagging was combined

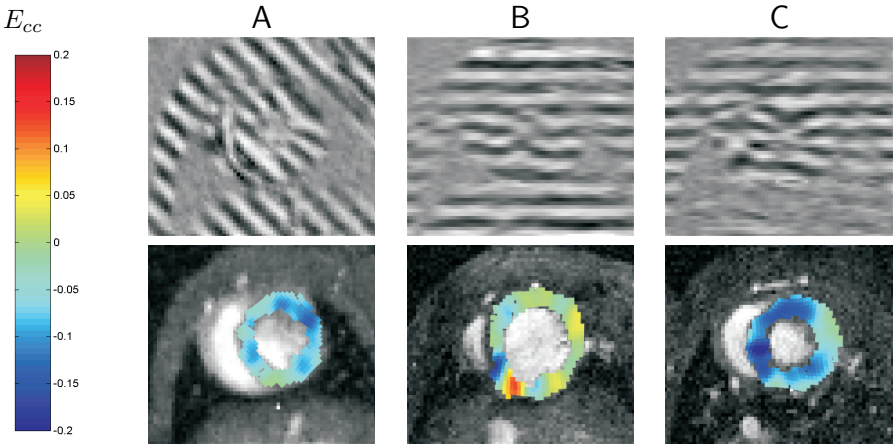

Figure 5.3: The top row shows horizontally tagged CSPAMM images of a healthy mouse heart (A) and an infarcted mouse heart (B, C) at end-systole. Slice B was positioned through the infarct region, while slice C was located remote above the infarction. The bottom row represents the calculated circumferential strain (E_{cc}) in every tracked point at end-systole. The E_{cc} is color coded according to the colorbar on the left. The data from the healthy mouse is rotated with 45 degrees to obtain approximately the same anatomical orientation as the other data.

with CINE MRI for the assessment of global myocardial function.
For the CINE measurements respiratory gating was omitted, resulting in a major reduction of the scan time. This is favorable because it is difficult to keep the heart rate of the mouse stable over longer periods of time, especially for those mice with a myocardial infarction. Nevertheless, as can be seen in the bottom row of Figure 5.2, no severe respiratory movement artifacts were introduced in comparison with for example those reported in Ref. [97]. However, the through and in-plane motion of the blood resulted in small artifacts in the phase-encoding direction. These artifacts can be reduced by using flow compensated gradients [178]. We have chosen not to use additional flow compensation because this increases the echo time, which results in loss of signal in the CINE images due to the short T_2^* of the myocardium and therefore a lower signal to noise ratio. Moreover, the MRI tagging technique is not very sensitive to phase errors, in contrast to the

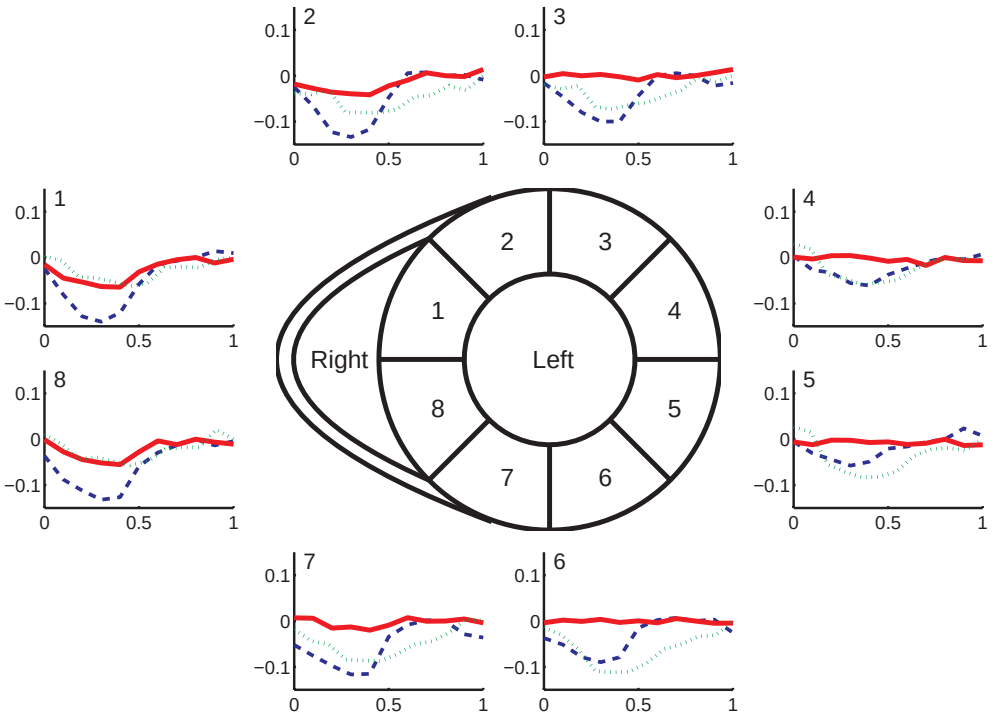

Figure 5.4: Analysis of the circumferential strain (E_{cc}) in eight zones of the left ventricular wall as function of time in a healthy mouse (dotted line), and for a mouse with infarction. The solid line represents a slice positioned through the infarct region, while the dashed line represents a slice remote above the infarction. Septum, zone 1 and 8; anterior, zone 2 and 3; lateral, zone 4 and 5; posterior, zone 6 and 7. The x-axis denotes the time through the cardiac cycle going from 0, begin-systole, to 1, end-diastole.

velocity-encoding technique, and therefore the small artifacts introduced by the flowing blood will not compromise the tagging analysis.
Because of this reduction in acquisition time it was possible to measure the left ventricular volume, using the multi-slice sequence, within a reasonable amount of time (approximately 2 hours). At the location of the infarction, apical anterior, the relative difference between end-diastolic and end systolic ventricular areas was considerably less for the mouse with myocardial infarction. This is a consequence of the impaired contractility of the myocardial wall introduced by the infarction and can also be observed in the tagging images (Fig. 5.3) discussed further on.
Since the in-plane spatial resolution of 200 μm is still rather coarse, the position and volume taken by the papillary muscles could not be determined with high accuracy automatically. Furthermore, the automatic segmentation method introduces some errors because of partial volume effects at the myocardial wall and the closing of the trabeculae at the end-systolic period. To assess the errors introduced in the determination of the ventricular volumes, we have compared the automatic segmentation with an expert manual segmentation. In general, the manual segmentation resulted in a 15% lower ESV and EDV, because of more accurate exclusion of papillary muscles and trabeculae. The ejection fraction however remained the same for both methods. The ejection fraction values found (Table 5.1) are comparable with other studies of mouse ventricular function [38, 39, 48, 74].
The CSPAMM tagging images were measured with the same resolution in the read-out direction as the CINE images. A major advantage of the CSPAMM technique is that the zero-order image information in k-space is filtered out efficiently and automatically. This will lead to a lower error in the strain and fewer artifacts [174].
A modified HARP analysis was used to track the material points on the left ventricular wall. This method has the advantage that we obtain comparable resolutions for the CINE and the displacement images, in contrast to the method described by Atalar [179], which results in a resolution decrease of at least a factor 4. The distance between material points is even decreased between begin-systole to end-systole, because material points are allowed to move towards each other as the heart contracts. The smaller distance is calculated by interpolation between the fixed image pixels. This is valid until, the wavelength of the CSPAMM tagging waveform is reduced to less then 2 pixels (Nyquist criteria).
There are several alternative MRI methods to measure regional displacements and strains in the myocardial wall, such a velocity encoding and Displacement ENcoding with Stimulated Echo (DENSE). However, velocity encoding is extremely sensitive to phase errors and needs time consuming velocity encoding and compensation of the MRI sequence. Furthermore, this method measures velocities rather than displacements, which makes it significantly more difficult to determine regional strains. Velocity encoding has the advantage that it can be used more easily in a three-dimensional manner. DENSE [61] can also

accurately measure displacements and strains with high spatial and temporal resolution. It is confirmed by Kuijer *et al.* [180] that DENSE is almost equal to tagging sequences. The main drawback of DENSE is a longer acquisition time due to the intrinsically lower signal to noise ratio.

The circumferential strains in Figures 5.3 and 5.4 show that there was no uniform distribution of strain values over the left ventricular wall of the infarcted mouse heart. The measured mean circumferential strain of the healthy mouse heart is lower than reported in the literature [59, 61], which might be explained by differences in mouse strain. Although a detailed analysis of the regional strains in relation to the induced infarction is beyond the scope of this chapter, it is noteworthy that the circumferential strain in the slice above the infarction (Fig. 5.3C and 5.4) was higher than that in the healthy myocardial wall. This might be explained by the fact that different regions of the mouse heart are going through a process of differential remodeling and adaptation such as also observed in humans [181, 182] and canines [183]. In contrast, Epstein *et al.* [59] have found impairment of the remote myocardium in mice. Their study, however, differs from our study by a difference in the adaptation time following infarction, 4 days versus 1 day, and a difference in the mouse model, reperfusion versus permanent occlusion. The mean circumferential strains in the infarcted region were lower than found in other studies [59, 61]. These differences might be caused by differences in the measuring position and differences in the extent of the induced infarction. The infarcted slice (Fig. 5.3B) showed an area with a high strain gradient in the apical inferoseptal region. Analysis of the CINE CSPAMM images in this region showed a small compression in the upper part and a small stretching in the lower part consistent with the strain analysis. From this we conclude that the area is still active and not infarcted but has an atypical contraction pattern. The circumferential strain outside the infarcted region is within the range of previously reported values [59, 61].

Conclusions

This study demonstrates the feasibility of MRI methods to measure and quantify global and regional function of mouse hearts with myocardial infarction, using CINE and CSPAMM tagging with HARP analysis. The ejection fraction can be measured with sufficient accuracy to distinguish between healthy and infarcted mouse hearts. We have shown that MRI tagging, combined with an improved HARP analysis enables the detailed determination of regional displacements within the ventricular wall. From these displacements the circumferential strain can be calculated, providing information on local function in healthy and infarcted hearts, with a comparable resolution as the anatomical images.

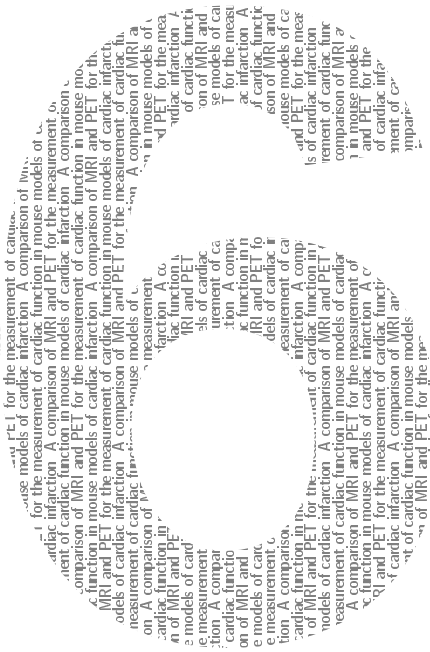

A comparison of MRI and PET for the measurement of cardiac function in mouse models of cardiac infarction

Edwin Heijman[1], Lars Stegger[2], Peter Leenders[3], Dirk Bürger[4], Christine Bätza[2], Klaus Schäfers[2], Michael Schäfers[2], Klaas Nicolay[1] and Gustav J. Strijkers[1]

[1] Biomedical NMR, Department of Biomedical Engineering, Eindhoven University of Technology, Eindhoven, the Netherlands.

[2] Department of Nuclear Medicine, University Hospital of Münster, Münster, Germany.

[3] Department of Pharmacology and Toxicology, Cardiovascular Research Institute Maastricht, Maastricht University, Maastricht, the Netherlands.

[4] Institute of Anatomy, University of Münster, Münster, Germany

Reviewed: Journal of Nuclear Medicine

Abstract

In biomedical research, there is a growing need for multi-modality imaging to cover the whole range from the anatomical to the molecular level. To truthfully judge these new developments it is necessary to explore the value of combining different modalities. In this study we compared global functional parameters measured by MRI and PET in a group of control mice (n = 12) and in a group of infarcted mice (n = 11). Infarct size was determined by: a) contrast enhanced MRI with the contrast agent Gd-DTPA; b) ^{18}F-FDG PET. The different MRI infarct size measures were compared to the PET infarct size values and the MRI determined ejection fraction.

The global functional parameters end-diastolic volume, end-systolic volume and ejection fraction determined by MRI and PET had a high correlation. PET overestimated the end-diastolic volume and end-systolic volume compared to MRI. The left myocardial wall volume was systematically lower for PET than for MRI. No significant correlation was found between the PET infarct size and several MRI infarct size measures. MRI global functional parameters closely correlated to the MRI based infarct sizes.

Introduction

In the scientific, medical and pharmaceutical community the effects of therapy and intervention are often studied in pre-clinical rodent models of human pathology. Non-invasive imaging is an important tool in this respect because it offers the possibility to do longitudinal studies, in which animals serve as their own controls. Although translation of the pre-clinical situation to humans is not straightforward, the broad applicability of imaging, its versatility and the high information density that can be obtained from the images, makes its worthwhile to heavily invest in new pre-clinical imaging modalities and applications.

Most imaging modalities used in a modern hospital have a pre-clinical version. The following pre-clinical small animal modalities are commercially available: computed tomography (CT), echocardiography, position emission tomography (PET), single photon emission computed tomography (SPECT) and Magnetic Resonance Imaging (MRI). Another trend is to merge different imaging modalities physically into one scanner, *e.g.* PET/CT, SPECT/CT, PET/MRI, to combine the strength of different modalities for obtaining anatomical, functional and metabolic information within a single imaging session [184, 185]. For small animals PET/CT [186] and SPECT/CT systems [187] are already commercially available and hybrid SPECT/MRI [188] or PET/MRI scanners [91, 189] are now under development. Future will tell us if this trend becomes common practice or that software is the key to combine the image information of the different modalities. Nevertheless, particularly in the case of PET and MRI, the combined scanner is not yet commercially available to imaging laboratories, and therefore researchers will still have to rely for some time on combining the images and information from separate PET and MRI scans.

More specifically, in studies of left ventricular function of the mouse heart a number of different techniques have been applied, among which are CT [190–192], echocardiography [193–195], PET [116, 196], SPECT [197] and pressure-volume conductance microcatheter [117, 198, 199]. MRI is often considered the gold standard for functional assessment by other specific modalities [116, 117, 190, 195, 199, 200]. The added value of combining different imaging modalities is that the images can be fused and compared in a useful way. Global functional parameters and infarct size measured by MRI and PET were previously compared in humans [201, 202]. For the mouse heart a comparison between MRI and PET has been made of dilated hearts in survivin knockout mice [116], but not for infarcted mouse models. Thomas *et al.* [203] studied with MRI, SPECT and PET the infarcted rat heart with the same scientific question.

The main goal of this study was to compare global functional parameters as well as infarct size derived from separate MRI and PET measurements in a mouse model of myocardial infarction.

Methods

Mouse preparation

C57Bl6 mice (male, age, 3 months; weight, 25-30 g) were subjected either to permanent occlusion of the left anterior coronary artery (O; n = 6) or temporal occlusion of 30 min, followed by reperfusion (IR; n = 5) according to described procedures [175]. These 11 mice recovered over a period of two weeks before MRI and PET measurements were performed. After this period the infarct healing is not expected to change the global functional parameters [38] as well as infarct size much [175]. The infarct healing at the cellular level is still in progress [9]. Healthy C57Bl6 mice (n = 12) were used as controls (controls). In order to avoid age-related effects these control mice were measured after a period of 2 weeks upon arrival at the institute when they reached the same age as the mice with prior surgery. Global functional parameters of the left ventricle were first determined with MRI. The MRI scan protocol consisted of multi-slice CINE measurements to determine global functional parameters and delayed-enhancement multi-slice MRI for delineation of the infarct area. For the latter measurements the 4 O, 4 IR and 8 control mice received a bolus injection of Gd-DTPA (0.2 mmol/kg) in the tail vein. Within four days after the MRI examination the mice were transferred to the PET facility for an ^{18}F-PET scan. Both global functional parameters as well as infarct size were determined from the PET scan.
For the MRI and PET scans, the mice were first sedated in an induction chamber by exposure to 3 vol% isoflurane in medical air at a flow rate of 0.4 l/min. During the experiments the mice inhaled approximately 1.5 vol% isoflurane in medical air (0.3 l/min) from a dedicated anesthesia mask. The isoflurane concentration was adjusted during the experiments to maintain the respiration rate within the range of 1.0 to 1.6 s^{-1}. The respiration of the mouse and electric activity of the heart (ECG) were continuously recorded and filtered by specialized physiological monitoring equipment (MRI: Rapid Biomedical, Rimpar, Germany; PET: BioVet, Spin Systems, Brisbane, Australia). The signals from the physiological monitoring equipment were used either for ECG triggering and respiratory gating of the MRI scanner or registered for retrospective list-mode reconstruction of the PET data [204]. The respiratory motion was measured with a balloon connected to a pressure sensor and positioned on the abdomen of the mouse. The ECG leads were fixed to the front paws for MRI and to the front paw and hind leg for PET, respectively. The body temperature of the mouse was kept at approximately 37°C with a heating pad controlled by a rectal temperature sensor. All measured physiological parameters were stored in a computer during the MRI experiments.

The Animal Care Committee of Maastricht University (Maastricht, the Netherlands) ap-

proved the experimental protocol. The PET scans were approved by the responsible local authorities (Bezirksregierung) in Münster, Germany.

MRI protocol

The MRI examinations were performed with a 6.3 T horizontal-bore small-animal MRI scanner (Bruker, BioSpin MRI GmbH, Ettlingen, Germany) equipped with 400 mT/m gradients using Paravision 3.0.2 software. A quadrature driven birdcage coil (Rapid Biomedical, Rimpar, Germany) with an inner diameter of 3.2 cm was used for transmission and reception. After induction of anesthesia the mice were placed supine in a dedicated mouse cradle, which contained the anesthesia mask, the ECG leads, the respiratory sensor and a heating pad.
To determine the global functional parameters, a stack of short-axis slices covering the heart from apex to base and two orthogonal long-axis slices were acquired with an ECG triggered and respiratory gated CINE FLASH sequence [32] with the following parameters: Gaussian-shaped RF-pulse, 300 μs; flip angle, 15°; repetition time, 7 ms; echo time, 2.3 ms; sample rate, 100 kHz; echo position, 30%; field-of-view, 3x3 cm^2; matrix, 192x192; in-plane pixel dimension, 156x156 μm^2; slice thickness, 1 mm; number of averages, 6; total acquisition time per slice, approximately 5 min.
The contrast-enhanced MRI acquisition was performed with a multi-slice ECG triggered

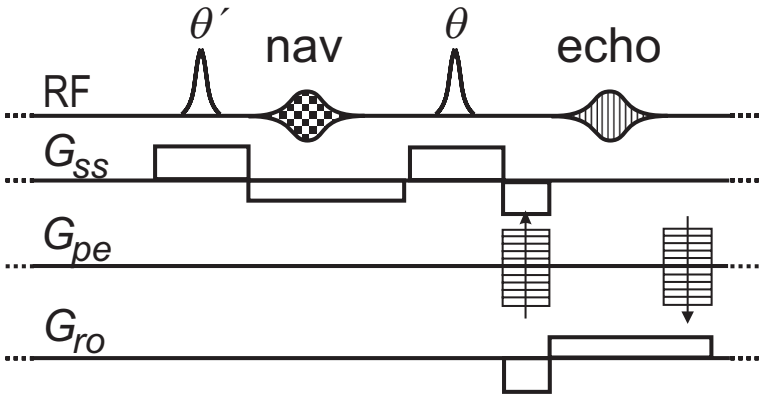

Figure 6.1: Diagram of the ECG triggered FLASH sequence with the extra navigator slice for retrospective respiratory gating of the contrast enhanced MRI acquisitions with: RF: the radio frequency channel; G_{ss}: the slice selective gradient; G_{pe}: the phase encoding gradient; G_{ro}: the readout gradient. The direction of each gradient can be freely chosen. We used different orientations and positions for the navigator slice and the image slice (see text). Nav: navigator echo; echo: the encoded image echo; θ': flip angle to excite the navigator slice and θ : flip angle to excite the image slice.

FLASH sequence with the following parameters: Gaussian-shaped RF pulse, 300 μs; flip angle, 50°; repetition time, 78 ms; echo time, 2.2 ms; sample rate, 100 kHz; echo position, 40%; navigator echo points, 256; field of view, 3x3 cm^2; matrix, 256x256; in-plane pixel dimension, 117x117 μm^2; slice thickness, 1 mm; number of short-axis slices, 10; number of averages, 6; total acquisition time for 1 repetition, 3 min. Two pre-injection acquisitions were made followed by at least 6 post-injection acquisitions. The time between the different acquisitions and the injection was recorded and stored in a computer. To reduce blood-flow artifacts a specific temporal slice order scheme was used: [5 3 6 4 7 9 2 0 8 1] with slice 7 placed at the apex in the end-systolic phase of the CINE MRI acquisition and slice 0 at the base of the mouse heart. Slice 8 and 9 could be used to monitor the enhancement of the blood without having a risk of motion artifacts. The sequence used is schematically depicted in Figure 6.1. The sequence included a navigator signal to retrospectively remove artifacts from breathing motion [107, 205]. The navigator slice was placed perpendicular to the diaphragm at a position of large respiratory motion while not slicing the heart. The sequence parameters for the navigator slice were: Gaussian-shaped RF pulse, 300 μs; flip angle, 5°; slice thickness, 3 mm.

PET protocol

Mice were scanned in a near-millimeter-resolution (volumetric resolution $\approx 1\mu$l) dedicated small-animal PET system. The quadHIDAC (Oxford Positron Systems, Weston-on-the-Green, UK) PET system utilizes 4 stacks of 8 stacked wire chamber detectors placed perpendicularly to each other creating a cubic field of view. This detector configuration offers an almost uniform resolution within the measurement area [206]. To further improve the homogeneity the whole detector setup rotates 180 degrees around the axial direction within 6 s and in the reversed direction thereafter for also 6 s.
The anaesthesia protocol was identical to that used for the MRI scans. One hour before the measurement ^{18}F-FDG (15 MBq) in 100μl 0.9% saline was injected intravenously. List-mode emission data were acquired for 30 min, while simultaneously the ECG and the respiratory motion were recorded and co-registered to the PET data. Subsequently, the list-mode data were retrospectively sorted into 16 equidistant frames on the basis of the ECG signal with dedicated in-house software [207]. All frames were reconstructed into a 3D image of 110x60x60 mm^3, voxel size of 0.4x0.4x0.4 mm^3 using an iterative resolution recovery reconstruction algorithm, achieving an effective resolution of 0.7 mm [208]. For infarct size determination an additional 3D image was reconstructed without ECG sorting.

Data analyses

MRI data

The CINE MR images were analyzed in a manually supported semi-automatic segmentation software program CAAS MRV FARM (Pie Medical Imaging, Maastricht, Netherlands). The following global functional parameters: end-diastolic (EDV) and end-systolic (ESV) endocardial volumes, left-ventricular ejection fraction (EF), stroke volume (SV), cardiac output (CO) as well as end-diastolic myocardial mass (LVM) (without papillary muscles) were calculated on a slice-by-slice basis with and without long-axis correction to account for systolic long-axis shortening of the left ventricle [209]. For completeness also the epicardial volumes at end-diastole and end-systole were determined as well as the papillary volumes.

The Bruker Paravision software was used to extract the navigator echo from the contrast-enhanced MRI data. The navigator echo intensity as function of time was convoluted by a step function for detecting the periodic respiratory motion (Fig. 6.2). To avoid respiratory motion artifacts, k-lines collected during the breaths were discarded. Subsequently, the remaining k-lines were sorted and images were reconstructed. For comparison the images were also reconstructed without respiratory motion correction. To test the decrease in signal-to-noise (SNR) due to retrospective respiratory gating, the SNR of the myocardial wall was determined. The SNR was calculated in one short-axis slice around the mouse heart equator in the first post injection MR image of 8 CE MRI datasets from the control group.

From the MRI measurements, the infarct sizes were determined in three different ways. For the first method, the infarct volume was determined manually by applying a threshold in the contrast-enhanced MR images to distinguish bright infarct tissue from darker viable tissue. Only those parts of the infarcted myocardium with a transmurality of more than 50% were added to the infarct volume. The infarct size volume ratio (ISV) was then calculated according to ISV = IV/LVV, where IV is the infarct volume and LVV the total left ventricle volume. For the second method the left ventricle epicardial and endocardial contours obtained from the contrast-enhanced MRI were used to determine the mid-wall of the left ventricle. The mid-wall contours in all the short-axis slices were then combined into a left ventricle mid-wall surface. The surface of the infarct was defined as the area where the infarct had at least 50% transmurality. The infarct size surface ratio (ISS) was then calculated according to ISS = IS/LVS, where IS is the infarct mid-wall surface and LVS the total left ventricle mid-wall surface. For the third method the CINE MR images were analyzed. The left-ventricle mid-wall surface was calculated from epicardial and endocardial contours at end-diastole. Infarct tissue was segmented by thresholding the parts of the left-ventricle, which had a change in transmural wall thickness between end-systole and end-diastole of less than 30%, indicating that the tissue is not viable

and not contracting [10, 38]. The infarct size surface ratio based on this wall thickening (ISWT) as observed in the CINE images was defined as ISWT = IS/LVS, where IS is the infarct mid-wall surface (based on wall thickening) and LVS the total left-ventricle mid-wall surface. The navigator analyses and infarct surface calculations were performed in Matlab 6.1 (The Mathworks, Natick, MA).

PET data
For automated assessment of the global functional parameters from the PET data a left-ventricular 3D model was fitted to the reconstructed gated emission data. The endo- and epicardial borders within the different frames of the cardiac cycle were deduced [210] from the model. From these borders the different global functional parameters: EDV, ESV, EF, SV and LVM were calculated as well as the epicardial volumes at end-diastole and end-systole.
The 3D fitting model was also applied to the non-gated PET data for mid-wall surface calculations. The PET infarct size was determined by setting a threshold of 50% of maximum myocardial activity as described in [211]. The PET infarct size was defined as ISP/LVSP, where ISP is the infarct surface and LVSP the total left-ventricle surface.

Comparison of MRI and PET
The variability and correlation of the global functional parameters: EDV, ESV, EF, LVM and SV obtained by MRI and PET were calculated. To check for linearity of the comparison an orthogonal regression was applied to the different mouse groups and global functional parameters. Infarct sizes determined by PET as myocardium surface ratios were compared to MRI measurements of ISV, ISS and ISWT. To test the predictability of the infarct size on the EF, a linear regression was applied between the different infarct size measurements (MRI and PET) and the EF. Statistical correlations were tested for significance by a paired student t-test. Values were considered to be significantly different when $p < 0.05$.

Results

The mean bodyweight of the mice, measured before the MRI acquisition, was: 28.4 ± 1.3 g, 26.8 ± 1.7 g and 26.0 ± 0.9 g (mean ± SD) for the control, occlusion (O) and ischemia reperfusion (IR) mice group, respectively. The mean heart rate, during the MRI experiments, was: 509.2 ± 49.3 beats/min (control), 528 ± 48 beats/min (O), 536 ± 29 beats/min (IR) (mean ± SD). The heart rates resulted in a range of 14 to 20 frames per cardiac cycle for the short-axis and long-axis CINE acquisitions. Due to retrospective respiratory gating of the CE MRI acquisition the mean SNR of the myocardial wall was

reduced in the first post injection scan from 20 ± 4 to 15 ± 4 in the control group (n = 8) for the non-gated ($SNR_{non-gated}$) and gated (SNR_{gated}) images, respectively. Using the formula [111]

$$N_{gated} = \left(\frac{SNR_{gated}\sqrt{N_{non-gated}}}{SNR_{non-gated}} \right)^2, \tag{6.1}$$

we can calculate that we reduce the number of mean averages from 6 ($N_{non-gated}$) to 3.4 (N_{gated}) which agrees with Figure 6.2 as well as with our previous study (see Chapter 2). Four different mouse hearts visualized by CE MRI and ^{18}F-FDG PET are shown in Figure 6.3. The locations of the images were around the equator of the mouse heart and to correct for the slice thickness difference between MRI and PET, 5 PET slices were added. In the first column of Figure 6.3 the non-gated CE MR images are shown, in the second column the retrospective respiratory gated CE MR images and in the last column the corresponding PET images.

The main improvements in the images in case of the retrospective respiratory gating were: in 6 datasets more homogeneous signal within the left-ventricle anterior wall which touches the liver (*e.g.* Figure 6.3 A2, B2, C2); in 4 datasets better defined texture of the pulmonary vessels was found (*e.g.* Figure 6.3 B2); and in 2 datasets better defined endocardial wall or visibility of the blood pool was found. In 7 datasets more than 4 images suffered from unbalanced noise behavior of the filtered k-lines in k-space leading to extra striping artifacts (*e.g.* Figure 6.3 C2).

MRI and PET measurements could not be performed simultaneously. Within the four days between MRI and PET acquisition the mice gained some weight, the mean differ-

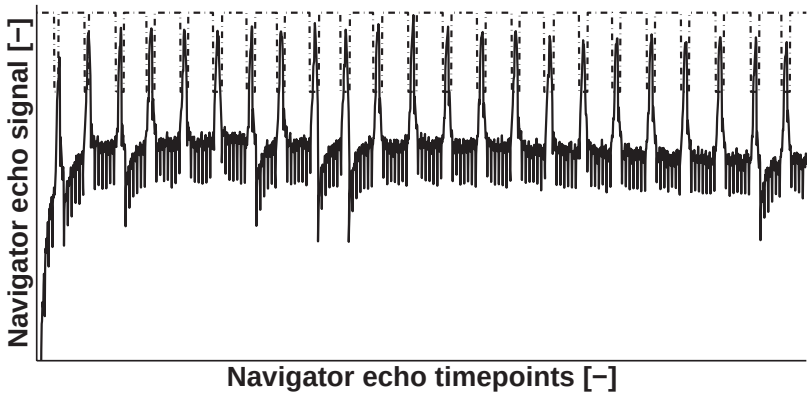

Figure 6.2: Typical navigator echo signal as function of time at the beginning of an ECG triggered contrast enhanced MRI acquisition (solid line). The large spikes were identified as the respiratory periods and the small spikes represent cardiovascular activity. The striped-dotted line is the retrospective respiratory gated signal. This signal is then used to remove the MRI data which were acquired during respiration. Number of points = 2000; time interval = approximately 20 s.

Table 6.1: Mean global functional parameters determined by MRI.

Group	Control		Occlusion		IR	
Long-axis volume correction	no	yes	no	yes	no	yes
Epicard ED [μl]	142.6 ± 15.2	151.3 ± 6.5	215.3 ± 69.8	229.1 ± 64.7	188.3 ± 63.4	194.1 ± 60.5
EDV [μl]	56.3 ± 7.6	60.4 ± 5.6	121.7 ± 65.2	126.3 ± 62.1	97.0 ± 54.6	97.7 ± 53.0
Epicard ES [μl]	117.9 ± 10.6	115.1 ± 7.7	205.1 ± 73.2	206.6 ± 72.2	175.1 ± 60.5	170.3 ± 57.9
ESV [μl]	19.4 ± 4.0	18.0 ± 2.9	93.9 ± 67.1	92.9 ± 68.3	69.8 ± 55.8	67.1 ± 54.0
EF [%])	65.7 ± 4.0	70.2 ± 3.9	30.6 ± 16.5	34.5 ± 20.3	35.4 ± 16.5	38.8 ± 17.7
LVM [μg]	90.5 ± 11.9	95.4 ± 7.2	99.5 ± 9.7	108.0 ± 7.1	95.9 ± 13.5	101.2 ± 10.5
SV [μl]	37.0 ± 4.9	42.4 ± 4.8	28.9 ± 7.4	33.4 ± 12.1	27.1 ± 3.0	30.6 ± 3.3
CO [ml/min]	18.9 ± 2.6	21.7 ± 2.8	15.3 ± 3.3	17.5 ± 5.5	14.6 ± 1.5	16.5 ± 1.8
Papillaries [μl]	4.5 ± 0.7	4.5 ± 0.7	3.7 ± 1.6	3.7 ± 1.6	4.5 ± 1.2	4.5 ± 1.2

Data are mean ± SD

ences were: 0.9 ± 0.8 g (control), 0.6 ± 0.8 g (O), 0.7 ± 1.0 g (IR) (mean ± SD), compared to the weight just before the MRI measurement. The P-value of the weight comparison of all mice before MRI and PET acquisition was 0.00019, which makes the gain in weight significant.

The global functional parameters in Table 6.1 were determined after segmenting the CINE MR images of the three groups. We excluded the papillary muscle volume from the global functional parameters (EDV, ESV, EF, LVM and SV). Also an extra long-axis correction was applied on the MRI global functional parameters to bridge the 2-dimensional MRI acquisition with the 3-dimensional PET acquisition (see Table 6.1). The non-corrected global functional MRI parameters of the control group were in accordance with an early study of smoothelin-B mice (see Chapter 4). These values were also comparable with other previous studies [69, 110, 212], which reported global functional parameters of mice of comparable weight, gender and strain. Comparing the global functional parameters of both groups with prior surgery is very difficult due to the large variation of the infarct size.

The long-axis corrections applied to the three groups in Table 6.1 resulted in an increase of the mean value of the following parameters: EDV, EF, LVM, SV and CO compared to the non-corrected data. Mean ESV values were decreased in all groups after the long-axis correction. No pattern was found in the changes of the standard deviations caused by the long-axis corrected data. Although measured with a different PET method as used in this study (time-activity curve method), the cardiac output and stroke volume reported by Kreissl *et al.* [213] were comparable with the MRI values of the long-axis corrected

control group.
PET global functional parameters of the different mouse groups are listed in Table 6.2. To the best of our knowledge, the global functional parameters EDV, ESV, EF and LVM are the first PET imaging data collected for a relatively large group size. Yang *et al.* [214] measured the EDV and ESV of only two mice, but their findings did not correspond with values obtained within this study. The standard deviations of the global functional parameters of the control group measured with PET were slightly higher compared to corresponding MRI-derived values when using long-axis correction. When comparing the two mice groups with prior intervention a smaller standard deviation was found for the EDV and ESV values obtained by PET. Only the PET EF of the occlusion group was smaller than the corresponding MRI EF value in Table 6.1.
To generate two mice groups of comparable size, all infarcted mouse hearts (O and IR) were combined to a single infarction group and combined with the control group in Table 6.3. Significant differences between the MRI and PET global functional parameters were found in the control group for the following parameters: EDV, ESV and LVM. The long-axis correction increased by all comparisons the P-value of the student t-test (data not shown). To test the relation between MRI and PET determined global functional parameters, the variability and correlation were calculated within both mice groups. The linearity was tested by an orthogonal regression. The orthogonal regression does not distinguish between predictor and response; both are measured with comparable error (standard deviation). The results of the variabilities, correlations and orthogonal regressions are given in Table 6.3. All three were determined for the MRI-based global functional parameters without and with long-axis correction. The variabilities are larger than the inter-variability in the MRI study of Chapter 3, which used the manual segmentation. PET overestimates the global functional parameters EDS, ESV, EF and SV and underestimates the LVM compared to MRI without long-axis correction. For the EF this

Table 6.2: Mean global functional parameters determined by PET.

Group	Control	Occlusion	IR
Epicard ED [μl]	115.7 ± 16.1	223.3 ± 85.3	146.0 ± 91.5
EDV [μl]	71.7 ± 11.7	132.2 ± 60.3	108.1 ± 58.3
Epicard ES [μl]	66.4 ± 13.6	183.4 ± 74.7	180.0 ± 90.6
ESV [μl]	23.3 ± 8.3	91.9 ± 48.2	74.8 ± 59.1
EF [%]	68.2 ± 6.1	32.3 ± 8.4	38.4 ± 23.5
LVM [mg]	46.3 ± 5.6	95.7 ± 35.1	39.8 ± 39.3
SV [μl]	68.2 ± 6.1	40.4 ± 14.2	33.4 ± 17.2

Data are mean ± SD

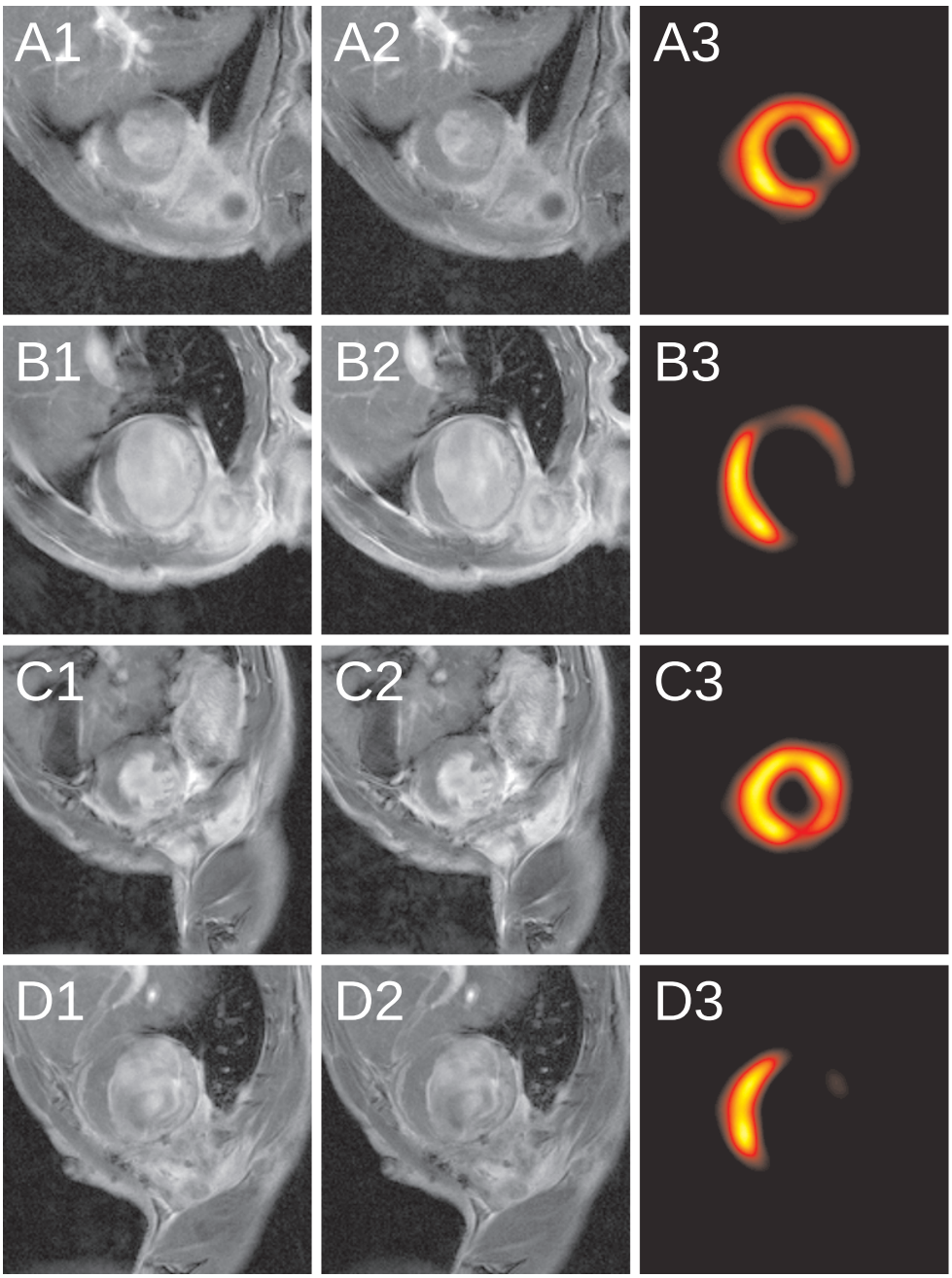

Figure 6.3: Short-axis slices of four different infarcted mouse hearts (A,B,C,D) around the equator. Left column: contrast-enhanced MRI without respiratory gating; middle column: contrast-enhanced with retrospective respiratory gating; right column: reconstruction and non-gated PET reconstruction.

changed to a slight underestimation when the MRI with long-axis correction was applied. There is no clear pattern in the variabilities data between the MRI data without and with long-axis correction. The correlations of the global functional parameters EDV, ESV and EF are high. The LVM and SV values showed very poor correlations between PET and MRI. The orthogonal regression findings are almost equal to the correlation findings. The long-axis correction showed no significant improvement in the orthogonal regression of all the global functional parameters. Only the offset term was decreased for the EDV and EF. Orthogonal regressions are visualized in Figure 6.4.
Blandt-Altman plots in Figure 6.5 show that only one outlier was found in the EF of the infarcted group when using an error range of two times the standard deviation. The ESV had a large spread of the data points in both groups, which was also found for the EF of the infarcted group. The small overestimation of PET values compared to MRI for the EDV and ESV is almost absent in the EF values. The mice with prior surgery had a smaller offset of the variabilities of all three global functional parameters and had a lower deviation of the EDV.
The CE LVM of the infarcted mice were 110 ± 9 mg as determined by the ISV analysis, which was overestimated compared to the non-corrected CINE LVM (99.4 ± 13.0 mg) ($p = 0.03$).

Table 6.3: Global functional parameter of all mice compared between MRI and PET, expressed in variability, correlation and orthogonal regression (n = 23).

	Variability		Correlation	Orthogonal
	Value	Percentage		Regression
Without long-axis correction				
EDV [μl]	-13.1 ± 10.3	-14.8 ± 11.6	0.98*	0.97x+15.90
ESV [μl]	-2.6 ± 14.2	-5.0 ± 27.7	0.96	0.90x+7.77
EF [%]	-2.6 ± 9.2	-5.0 ± 18.1	0.90	1.01x+2.06
LVM [mg]	35.9 ± 31.6	47.5 ± 41.7	0.32*	8.00x-691.53
SV [μl]	-10.6 ±-11.2	-28.1 ± 32.3	0.32*	3.91x-83.92
With long-axis correction				
EDV [μl]	-9.7 ± 10.4	-10.7 ± 11.5	0.98*	1.00x+9.87
ESV [μl]	-4.1 ± 14.8	-8.3 ± 29.3	0.96	0.90x+9.17
EF [%]	1.7 ± 10.0	3.2 ± 18.8	0.89	0.96x+0.44
LVM [mg]	42.2 ± 29.7	53.5 ± 37.7	0.51*	6.59x-600.84
SV [μl]	-5.5 ± 13.5	-13.7 ± 33.5	0.22	3.60x-91.83

Variabilities are mean difference ± standard deviation
*: $p < 0.05$

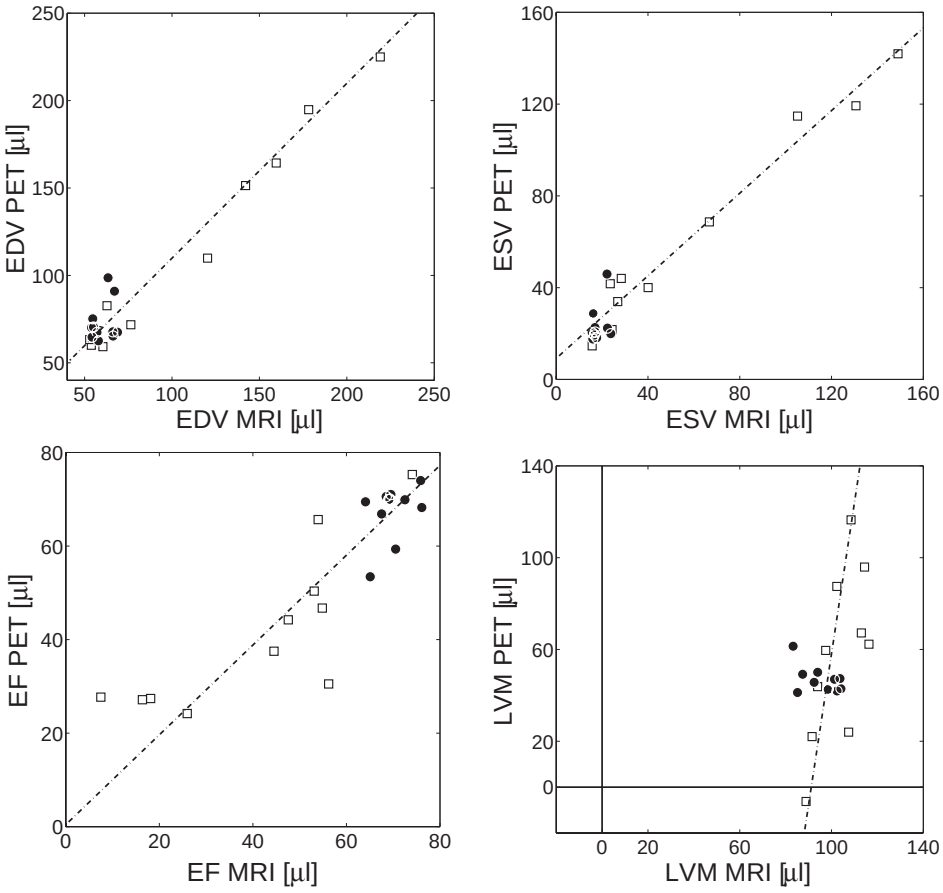

Figure 6.4: Orthogonal regression of the global functional parameters EDV, ESV, EF and LVM as determined by MRI and PET. A long-axis correction was applied to the MRI indices. The orthogonal regression results are listed in Table 6.3. •: the control group; □: the combined infarction groups.

As a preparation for the ISWT analysis the wall thickening of the control group was also measured. The mean wall thickening in the control group was 58 ± 27% (mean ± SD) of all hearts and segments according to the American Heart Association model [215]. Comparable wall thickening has also been found for healthy mice [10, 38]. The threshold was set on 15%, which was decided on the basis of our data and the results of the study from Yang *et al.* [10] and Ross *et al.* [38]. During the analysis of the ISWT we used an extra filter for excluding slices which had no visible infarcted regions in the contrast enhanced images to reduce the amount of false positives.

No linear correlations were found between the PET infarct size and the MRI infarct size measures: ISV, ISS and ISTW (see Table 6.4). A low R^2 (0.18) was also found for the correlation between PET infarct size and the PET determined EF. The MRI determined infarct size measures had a high linear relation with the MRI determined EF (see Table 6.4). Very small differences were found when comparing the linear regressions of the EF

Table 6.4: The results of linear regression between the different MRI determined infarct measures compared to PET infarct size values and the EF with and without long-axis correction (n = 8).

y-value x-value	PET infarct size surface [%]	EF (long-axis corrected) [%]	EF [%]
ISV [%]	0.53x+18.29 (0.05)	-1.96x+80.55 (0.91)	-1.79x+72.74 (0.93)
ISS [%]	0.34x+18.32 (0.07)	-1.01x+72.52 (0.82)	-0.95x+66.11 (0.87)
ISWT [%]	0.41x+16.35 (0.08)	-1.08x+74.69 (0.83)	-1.01x+68.02 (0.88)

Data are linear regression (R^2)
ISV: infarct size volume ratio based on the CE-MRI method
ISS: infarct size surface ratio based on the CE-MRI method
ISWT: infarct size ratio based on an infarct surface with a decreased wall thickening

with and without long-axis correction. The linear relation between EF and infarct size in MRI has been reported before [69]. The offset components of the orthogonal regressions (EF value of a heart without infarct) are close to the EF values in Table 6.1 of the control group without and with long-axis correction.

Discussion

The time between MRI and PET acquisitions and the transportation of the mice carried the risk of changing the (patho-)physiology in those small animals. However, every effort was made to obtain comparable conditions before and during the MRI and PET scanning. The weight of the mice changed significantly during the short period between scans, for which we have no explanation.

The hypothesis: "PET is not capable of measuring global functional parameters based on volume measurements" can be rejected. Overall, measurements for EDV, ESV and EF are in very good agreement with MRI. It is true that some global functional parameters measured by MRI and PET were statistically significantly different. However, correlations between them were high and the standard deviations within the control group were comparable between MRI and PET values. The methods' intrinsic capabilities to differentiate between mouse groups with normal and abnormal function were demonstrated for both MRI and PET in this study. As is often the case with biomedical measurements, normal values depend on the specific method and longitudinal studies should be performed using the same methodology. Although MRI is often used as the gold standard for measuring global functional parameters of the mouse heart, the deviation found between MRI and PET is attributable not only to the PET methodology and physiological shifts between different measurements but also to the MRI measurement. Like in PET, MRI-derived

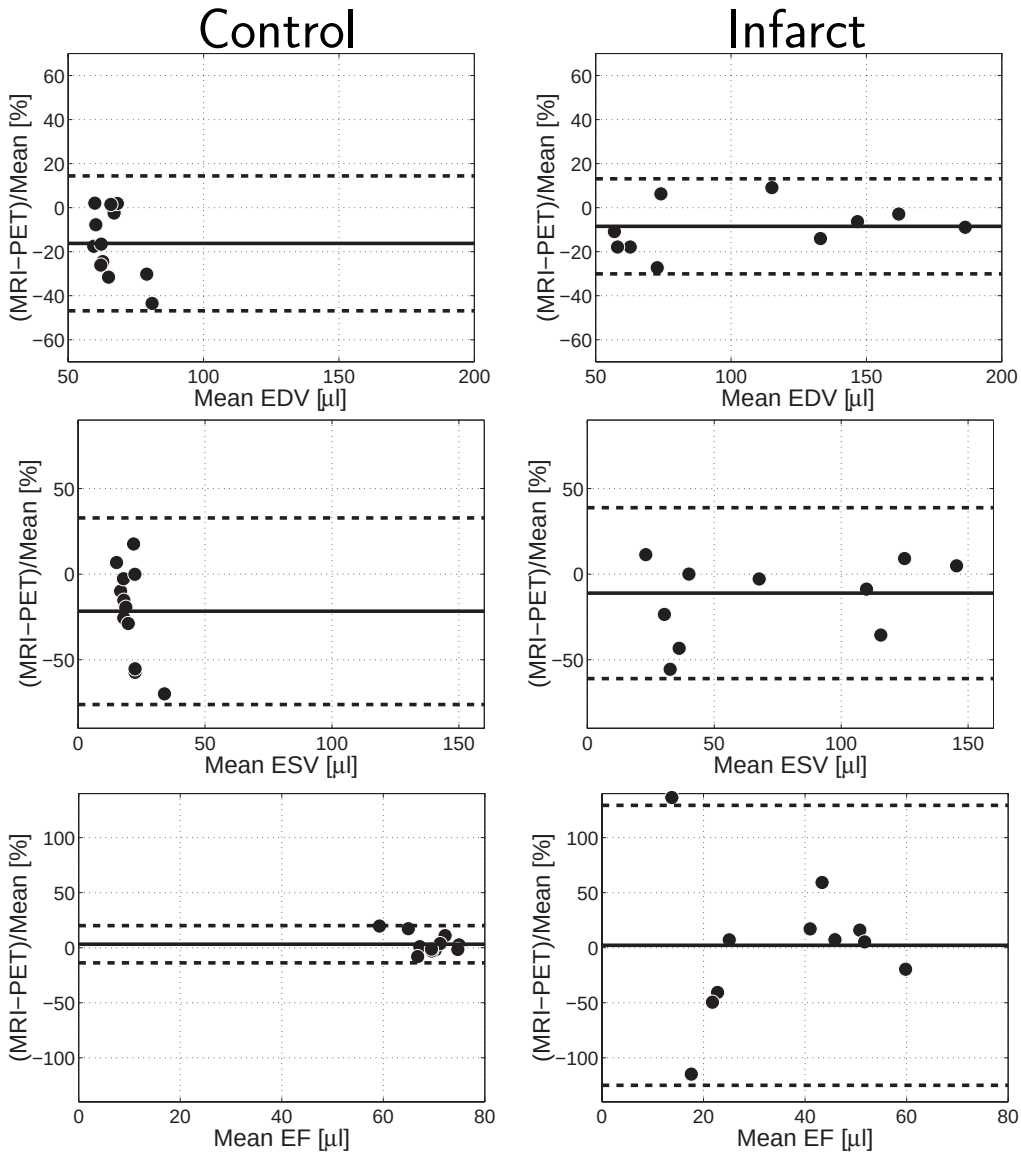

Figure 6.5: Blandt-Altman plots of the comparison between MRI and PET measured global functional parameters EDV, ESV and EF of the control group (left column) and the infarcted group (right column). A long-axis correction was applied to the MRI determined global functional parameters. Data is represented as mean variability ± 2 times the SD.

values depend on the details of assessment. We found that long-axis correction had a considerable effect and reduced the gap between the global functional parameters EDV, EF and SV of the 2D (MRI) and the 3D (PET) measurement technique. From all global functional parameters the LVM was considerably underestimated for the PET measurements compared to MRI, which is likely related to image resolution differences and the PET normalization towards endocardial volumes. This is why PET (and SPECT) as primarily molecular imaging modality is frequently used for the additional assessment of

global functional parameters. PET does not provide detailed anatomical information as such and this is where MRI is particularly strong.
A lot of MRI datasets suffered from unbalanced k-space noise behavior, which was never visible in the retrospective CINE acquisitions (see Chapter 2). This may have been caused by the high temporal correlation between certain k-lines and the respiratory motion due to interference of the respiratory motion on the ECG signal. In future studies this artefact should be investigated, because most retrospectively gated images showed better defined texture.
Although the locations of the myocardial infarctions were clearly visible with PET as well as with contrast-enhanced MRI, infarct size measurements did not correlate well between MRI and PET. The principle of detecting the infarct is totally different between the two techniques. MRI highlights the infarct region, while PET highlights the viable tissue. Delayed enhanced MR imaging correlates well with decreased flow and metabolism in PET in human cardiac infarction [216]. This is especially true when comparing transmural infarction without relevant residual viability. However, the situation can be expected to be different in myocardial regions with a mixture of viable cells and fibrosis. PET shows glucose uptake of viable cells, whereas MRI shows fibrosis. Since resolution is far away from being able to separate individual cells, the signal within the MR images shows presence of significant fibrosis (interpreted as scar) whereas PET images show glucose consumption (interpreted as a sign of viability). Also, a study with young animals which had been healthy before the intervention is strictly different from human research where most patients have suffered a long development of coronary artery disease before infarction. When measured a longer time after myocardial infarction, viable area at risk and living cells within infarcted regions will have become non-viable so that timing of MRI and PET measurements is critical. A possible reason why PET showed a larger proportion of viable tissue in comparison to MRI can be found in the higher spatial resolution of MRI. The used PET methodology has shown excellent correlation with histomorphometry for mouse models of permanent ligation developing transmural infarctions [211]. For non-transmural infarctions the 50% threshold may not be adequate. Small non-transmural infarctions are likely to be missed by PET completely. Wall segments without glucose uptake cannot be detected by the PET segmentation algorithm (see Figure 6.3). So there is a limit to the applicability of PET for determining functional parameters in severely infarcted hearts. These limitations must be respected and modalities that are independent of molecular uptake such as MRI are to be used instead. Although MRI is very sensitive in detecting damaged regions, it is not easy to quantify the damage from these images which can be seen directly on the PET images (see Figure 6.3). One should also consider the presence of inflammation within the damaged area, because this will lead to a higher metabolic rate [217]. To quantify the damage with MRI a contrast enhanced first passage of a bolus of contrast agent can be used which is frequently used in humans [218],

but due to the fast blood circulation time and the dimensions of the heart, this is very difficult in mice. A large difference in contrast enhancement was found between hearts where the wall thickness was strongly reduced by the infarction and the hearts where this had not occurred. In the latter hearts the myocardial wall showed strong contrast enhancement with a small not enhanced rim at the endocardium. This rim probably contained myocytes which had survived the ischemia period and were not damaged. The hearts with strongly thinned myocardial wall had almost no visible enhancement within this part of the myocardium. An explanation can be that the thinned wall had a fully repaired vascular structure. Another possible explanation is that the image resolution is sufficient to visualize the contrast enhancement resulting in a partial volume effect from the blood pool and surrounding tissue.
For MRI the EF correlated very well with infarct size, which as expected shows that the infarct size determined with MRI is functionally related to the global performance of the heart. This was also reported by Schneider *et al.* [70].

Conclusion

We have shown that global functional parameters EDV, ESV and EF as determined by MRI and PET are highly correlated. LVM was systematically lower for PET than for MRI. The transmurality of infarcts and the assessment of areas at risk with mixed viable and non-viable regions are likely to influence the comparison of infarct sizes between MRI and PET. The long-axis correction caused no significant improvement for the comparison between MRI and PET. The global functional parameters measured by MRI are closely correlated to the infarct size.
Future studies should clarify the origin of the differences in MRI and PET outcomes of infarct size. Detailed histological analyses are key to a better understanding of the intrinsic differences between the use of ^{18}F-FDG and Gd-DTPA for differentiating viable from non-viable issue in mice. Whereas in humans higher correlations were found [216] between MRI and PET determined infarct size measurements.
Extensive studies are also needed to explore the added value of hybrid MRI and PET scanning for research on cardiovascular diseases, or whether two separate scanners is a better practical solution in terms of PET sensitivity. The potential benefits of such multi-modality approaches strongly depend on the availability of effective image fusion software.

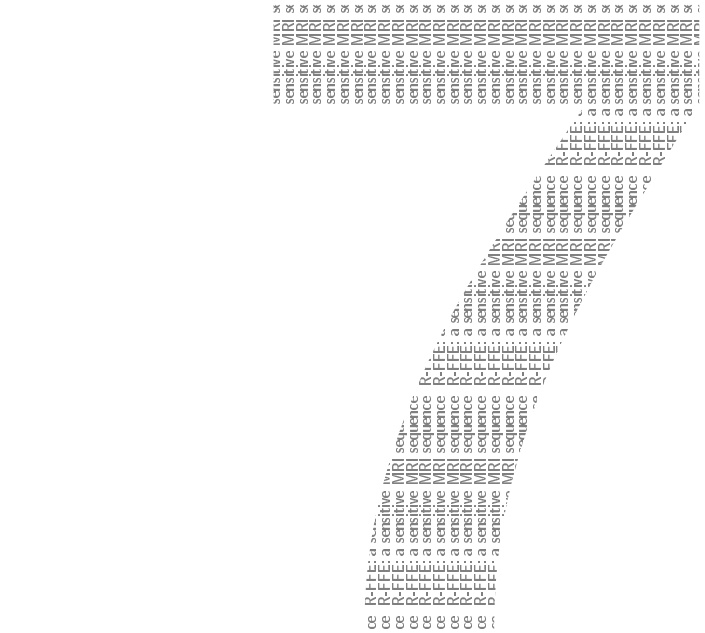

R-FFE: a sensitive MRI sequence

Edwin Heijman[1], Jacques den Boer[1], Rolf Lamerichs[2], Walter H. Backes[3], Klaas Nicolay[1], and Gustav J. Strijkers[1]

[1] Biomedical NMR, Department of Biomedical Engineering, Eindhoven University of Technology, Eindhoven, the Netherlands.

[2] Philips Research, Eindhoven, the Netherlands.

[3] Department of Radiology, Maastricht University Hospital, Maastricht, the Netherlands.

Abstract

Contrast-enhanced Magnetic Resonance Imaging (MRI), in particular molecular MRI, will benefit not only from improvements in the contrast agents but also from pulse sequences with improved contrast agent sensitivity. In this study we evaluate the Rephased-FFE (R-FFE) sequence for its contrast agent sensitivity. The R-FFE sequence is a steady state free precession (SSFP) MR sequence, which lacks the 180° phase advance between successive RF pulses, usually employed in other balanced SSFP sequences. Calculations were performed to understand the signal behavior of the R-FFE sequence. To study the real behavior of the R-FFE sequence *in vitro* experiments in phantoms with varying contrast agent concentrations were done and the sequence was evaluated *in vivo* in human volunteers at 1.5 and 3T.

It was shown with the calculations as well as with the *in vitro* experiments that the R-FFE sequence offers a more than six fold increase in sensitivity for the detection of low concentrations of paramagnetic contrast agents as the T_1-FFE sequence and has at least the same sensitivity as Balanced-FFE (B-FFE). The sequence has the additional advantage over other SSFP sequences that maximum signal intensity and sensitivity are obtained at very low flip angles, leading to a low specific energy absorption rate (SAR), important especially at high magnetic field strengths. *In vivo* applicability of the sequence was demonstrated in brains of human volunteers, resulting in fair quality images in regions that were appropriately shimmed. We concluded that the R-FFE sequence is an attractive candidate for the *in vivo* detection of low concentrations of contrast agents.

Introduction

There is a growing need for MRI as a means to detect low concentrations of contrast agents. The prime example of this need is in molecular imaging, the rapidly growing métier in which sparse molecular epitopes are traced *in vivo* by imaging, based on the use of targeted probes labeled with a contrast agent. Within the class of whole-body imaging modalities used for molecular imaging, MRI provides a high spatial resolution and an excellent soft tissue contrast, but has a limited probe detection sensitivity, often described as its main restriction for molecular imaging [25]. MRI can be used with either ferromagnetic or paramagnetic contrast agents.

Accordingly, there are two major pathways to improve the MRI probe detection sensitivity. Firstly, the number of contrast generating entities in the probe can be strongly increased, *e.g.* by the use of large ferromagnetic iron oxide particles [219–221] or paramagnetic nanoparticles with a high molecular weight [84, 89, 222, 223]. However, this approach leads to large probes for which the desired pharmacokinetic behavior cannot always be realized. The alternative is improvement of the detection sensitivity per unit concentration of the contrast agent. In that case, paramagnetic atoms such as Gadolinium are preferred because they can be built into small molecular constructs. Next to increase in field strength and in relaxivity of the molecular structure [224], the most important step in this approach is the use of an appropriate MR sequence.

Carr [225], long before MR imaging was conceived, observed the phenomenon of steady state free precession (often abbreviated as SSFP). He coined the term free precession to indicate absence of the RF field during signal observation. In his experiment no gradients were used. Soon after the first attempts of MR imaging the same phenomenon was used by Hinshaw [226, 227] for his sensitive point sequence and by Oppelt *et al.* [228] for a gradient echo sequence which was named "Fast Imaging with Steady state Precession" (FISP). SSFP imaging sequences allow the use of short TRs to create strong dispersion-free echoes in which (except for T_2-decay) all magnetization is refocused. In comparison with all other gradient echo sequences (characterized by echoes with partially dispersed magnetization) as well as with spin echo sequences (requiring much longer TR), the SSFP sequences offer a high signal to noise ratio per unit of scan time.

SSFP sequences however have two inherent difficulties. Firstly, the remaining inhomogeneity of the static magnetic field causes a position-dependent phase advance per TR, resulting in bands of signal loss within the field of view [229]. In the work of Zur *et al.* [229] and in other early publications (*e.g.* Hawkes and Patz [230]), the banding problem was tackled by using gradient waveforms of which the net surface area per TR is not equal to zero. However, this went at the cost of signal to noise ratio because of partial dispersion of the magnetization in the echo (and the resulting sequences in fact can no longer truly be called SSFP sequences). True-SSFP was maintained in proposals that used compound

images by summation of two [231] or more [232] elementary SSFP images, each with a controlled phase advance that differs per elementary image. Although in some of the elementary images the signals per voxel were high, this was not always the case and the resulting signal to noise ratio per unit time remained less than optimal. The early proposals for SSFP sequences of Hinshaw [227] and Oppelt *et al.* [228] included the use of a controlled phase advance of 180° per TR, and Haacke *et al.* [231] noted that this results in an outward shift of the bands of signal loss. He suggested renaming Oppelt's sequence as "true-FISP". This sequence regained interest when the performance of the clinical MR systems was boosted by the introduction of strong gradients. In these systems, imaging with much shorter TR became possible and the true-FISP sequence became much more clinically practicable [233, 234]. Several vendors introduced worked-out versions of this sequence for clinical use under trade names such as Balanced-FFE (Philips), trueFISP (Siemens), and Fiesta (General Electric).

The second difficulty inherent to the SSFP sequence is the strong contrast, in which most of the soft tissue is much darker than the body liquids. This has led to addition of magnetization preparation pulses, combined with collection of data from short echo trains and segmented coverage of the k space per segment [235, 236]. In this approach, the magnetization is in a transient state during the echo train and the signal strength varies per echo, while at the same time the control of signal oscillation in k-space could be addressed with sufficient care such that ghosting is avoided. As a result, SSFP imaging has shown promising results in a variety of clinical problems. Relevant for this article is its use for assessment of contrast enhancement [237, 238]. Perrin *et al.* [238] for instance demonstrated that balanced turbo field echo (B-TFE, the transient state alternative of B-FFE) offers sensitivity for detection of paramagnetic contrast agents that is much higher than obtainable by other sequences.

In this study, we will show that the SSFP condition without incorporation of a controlled 180° phase advance may offer a number of distinct advantages as compared to B-FFE. More specifically, the sequence combines a high sensitivity for the detection of low concentrations of T_1 lowering contrast agents with a low specific energy absorption rate (SAR). To distinguish the sequence from the usual SSFP sequences the sequence is denoted as "Rephased-FFE" (R-FFE), stressing the (nearly) equal phase of the magnetization of each successive echo [111].

We will first provide the theoretical framework for the signal behavior of R-FFE. Next, we report on *in vitro* measurements of a concentration series of Gd-DTPA in an aqueous $MnCl^2$ solution to verify the signal and contrast characteristics of the R-FFE sequences in comparison with B-FFE and with T_1-FFE (a spoiled gradient echo sequence). The latter sequence was included because it is used frequently for contrast studies. Finally, images of the brains of human volunteers at magnetic field strengths of 1.5 and 3T are presented to illustrate practical applicability of the R- FFE sequence.

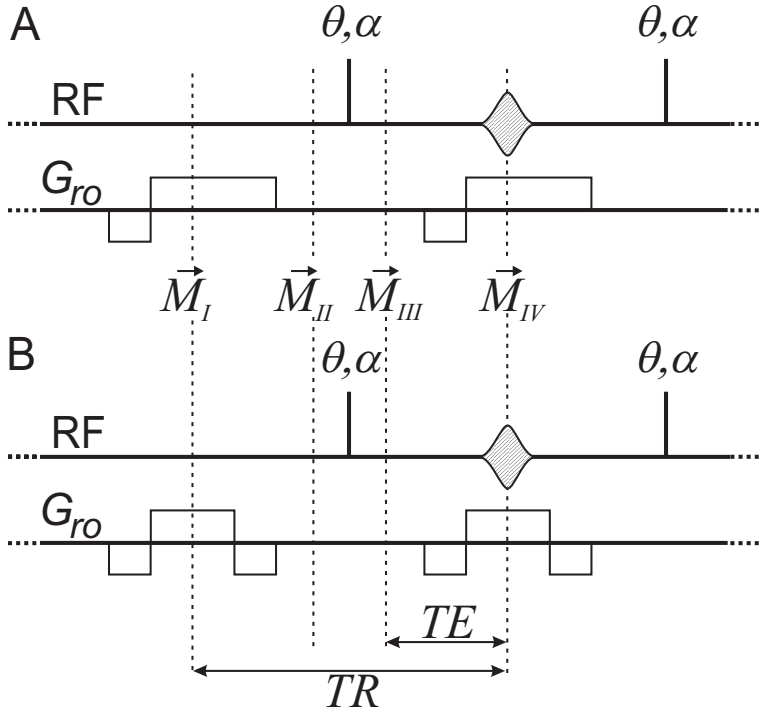

Figure 7.1: Graphical presentation of the magnetization calculation for (A) the T_1-FFE and (B) SSFP (R-FFE and B-FFE) sequences. Magnetization $\vec{M}_I$, $\vec{M}_{II}$, $\vec{M}_{III}$ and $\vec{M}_{IV}$ are indicated by the dashed lines at different time points. For simplification, only the RF channel (RF) and the read-out gradient (G_{ro}) are illustrated here. Further assumption was that the RF pulse width was infinitely small as well as the time period between RF pulse and the magnetization $\vec{M}_{II}$, $\vec{M}_{III}$. TR: repetition time; TE: echo time; θ: flip angle; α: RF phase.

Theory

The theoretical framework of this study was based on the article from Carr [225], which has been expanded for fast gradient echo imaging sequences by Haacke *et al.* [178] and Hargreaves *et al.* [239]. In short, the SSFP sequence is described by matrix transformations which are solutions of the Bloch equation [240].

The theoretical signal intensity was calculated from the transformations of a spin-vector $\vec{M}$ by the local magnetic field ($\vec{B}_{local}$), $\vec{B}_1$ field (RF pulse) and relaxation (T_1 and T_2). The local magnetic field was the summation of $\vec{B}_0$, local field inhomogeneity and the local magnetic field caused by a constant gradient field for image encoding. To simplify the calculations, we preferred to do our calculations within the rotating frame of reference [178]. This frame rotates with the MRI scanner's reference frequency (f_{ref}) around the B_0-axis. The angular frequency (ω) within this rotating frame of reference was defined as

$$\omega = \gamma \|\vec{B}_{local}\| - 2\pi f_{ref} \tag{7.1}$$

The Larmor frequency [178] was $f_l = \frac{\gamma}{2\pi}\|\vec{B}_{local}\|$. The transversal rotation ($\mathbf{P}$) during a period τ within the rotating frame of reference is:

$$\mathbf{P}(\omega,\tau) = \begin{bmatrix} \cos(\omega\tau) & -\sin(\omega\tau) & 0 \\ \sin(\omega\tau) & \cos(\omega\tau) & 0 \\ 0 & 0 & 1 \end{bmatrix} \tag{7.2}$$

The description of the RF pulse was restricted to a simple rotation matrix ($\mathbf{Q}$) around a transverse axis (*e.g.* y-axis) at a given time point [111] in the rotating frame of reference with

$$\mathbf{Q}(\theta) = \begin{bmatrix} \cos(\theta) & 0 & -\sin(\theta) \\ 0 & 1 & 0 \\ \sin(\theta) & 0 & \cos(\theta) \end{bmatrix} \tag{7.3}$$

The rotation angle of this infinite small RF pulse was defined as the flip angle (θ). The relaxation matrixes ($\mathbf{R}$ and $\mathbf{Z}$) with the relaxation times T_1 and T_2 were

$$\mathbf{R}(T_1,T_2,\tau) = \begin{bmatrix} e^{-\frac{\tau}{T_2}} & 0 & 0 \\ 0 & e^{-\frac{\tau}{T_2}} & 0 \\ 0 & 0 & e^{-\frac{\tau}{T_1}} \end{bmatrix} \quad \text{and} \tag{7.4}$$

$$\mathbf{Z}(T_1,\tau) = \begin{bmatrix} 0 \\ 0 \\ \left(1 - e^{-\frac{\tau}{T_1}}\right) M_0 \end{bmatrix}. \tag{7.5}$$

In the SSFP sequences as well as in the T_1-FFE four different time points (see dashed lines in Figure 7.1) were defined. The magnetization of the second time point and third time point were close in time located before and after, respectively, to the infinitely short RF pulse. The magnetization was calculated in each of the four time points. The magnetization is defined as a vector $\vec{M}$

$$\vec{M} = \begin{bmatrix} M_x \\ M_y \\ M_z \end{bmatrix}. \tag{7.6}$$

The evaluation of the magnetization during a SSFP sequence $\vec{M_{II}}$, $\vec{M_{III}}$ and $\vec{M_{IV}}$ can be written as function of the magnetization [239]:

$$\vec{M}_{II} = \mathbf{R}(T_1,T_2,TR-TE)\mathbf{P}(\omega,TR-TE)\vec{M}_I + \mathbf{Z}(T_1,T_2,TR-TE) \tag{7.7}$$

$$\vec{M}_{III} = \mathbf{Q}(\theta)\vec{M}_{II} \tag{7.8}$$

$$\vec{M}_{IV} = \mathbf{R}(T_1,T_2,TE)\mathbf{P}(\omega,TE)\vec{M}_{III} + \mathbf{Z}(T_1,T_2,TE) \tag{7.9}$$

These equations can be combined to a single equation for magnetization at the readout echo for a SSFP sequences:

$$\vec{M}_{k+1} = \mathbf{A}\vec{M}_k + \mathbf{B} \tag{7.10}$$

with

$$\mathbf{A}_{SSFP} = \mathbf{R}(T_1, T_2, TE)\mathbf{P}(\omega, TE)\mathbf{Q}(\theta)\mathbf{R}(T_1, T_2, TR - TE)\mathbf{P}(\omega, TR - TE) \tag{7.11}$$

$$\mathbf{B}_{SSFP} = \mathbf{R}(T_1, T_2, TE)\mathbf{P}(\omega, TE)\mathbf{Q}(\theta)\mathbf{Z}(T_1, T_2, TR - TE) + \mathbf{Z}(T_1, T_2, TE) \tag{7.12}$$

For the T_1-FFE sequence the magnetization before the RF pulse ($\vec{M}_{II}$) could be replaced by:

$$\begin{aligned} \vec{M}_{II} = {} & \mathbf{R}(T_1, T_2, TR - TE)\mathbf{P}(\omega, TR - TE) \begin{bmatrix} 0 & 0 & 0 \\ 0 & 0 & 0 \\ 0 & 0 & 1 \end{bmatrix} \vec{M}_I \\ & + \mathbf{Z}(T_1, T_2, TR - TE) \end{aligned} \tag{7.13}$$

This is only true when the magnetization is fully spoiled in the transversal plane by phase cycling of the RF pulse or by gradient spoiling. The matrixes $\mathbf{A}_{T_1}$ and $\mathbf{B}_{T_1}$ of the T_1-FFE sequence then becomes:

$$\begin{aligned} \mathbf{A}_{T_1} = {} & \mathbf{R}(T_1, T_2, TE)\mathbf{P}(\omega, TE)\mathbf{Q}(\theta)\mathbf{R}(T_1, T_2, TR - TE)... \\ & \mathbf{P}(\omega, TR - TE) \begin{bmatrix} 0 & 0 & 0 \\ 0 & 0 & 0 \\ 0 & 0 & 1 \end{bmatrix} \end{aligned} \tag{7.14}$$

$$\mathbf{B}_{T_1} = \mathbf{R}(T_1, T_2, TE)\mathbf{P}(\omega, TE)\mathbf{Q}(\theta)\mathbf{Z}(T_1, T_2, TR - TE) + \mathbf{Z}(T_1, T_2, TE) \tag{7.15}$$

Most fast gradient echo sequences are repetitive, except for the phase-encoding gradients, and can therefore be described by a discrete time system from which the steady-state magnetization ($\vec{M}_{ss} = \vec{M}_k = \vec{M}_{k+1}$)) can be derived for the T_1-FFE and SSFP sequences. The $\vec{M}_{ss}$ can be solved by the equation for the T_1-FFE [178] and the SSFP sequences [239]:

$$\vec{M}_{ss} = (I - \mathbf{A})^{-1}\mathbf{B} \tag{7.16}$$

The solutions of equation 7.16 for the T_1-FFE and SSFP sequences were calculated and further analyzed in Mathematica 5.1 (Wolfram Research, Inc., Champaign, IL). To calculate the signal intensity we assumed that a linear relation exists between the magnetization of a single spin and the signal intensity within an image.
Signal intensity calculations were performed for the combinations of T_1 and T_2 that represented the samples used in our experiments (aqueous $MnCl^2$ solution with up to 0.2

mM Gd-DTPA, see Methods). Signal intensities were converted to signal to noise ratios (SNRs) by assuming a noise level of 2% of the equilibrium magnetization M_0, creating approximately the same parameter space as in the measurements. The enhancement of the contrast to noise ratio induced by Gd-DTPA (CNR enhancement) was calculated by the subtraction of the SNRs of the reference and the Gd-DTPA containing samples.
The Gd-DTPA sensitivity S of the different sequences was defined as the CNR enhancement per mM Gd-DTPA. For a fair comparison with respect to signal to noise efficiency, the calculations were done keeping the product of TR and the number of averages constant. This definition can be used only as long as the enhancement increases linearly with concentration. In reality, this may not be true and therefore, as operational provision in the calculations, we obtained the Gd-DTPA sensitivity from the enhancement at 0.2 mM Gd-DTPA, a choice that includes the maximal Gd-DTPA concentrations expected in molecular imaging. This sensitivity at 0.2 mM Gd-DTPA is denoted as $S_{0.2}$. It was calculated as function of TR, flip angle θ and phase advance ϕ, *i.e.* the difference in phase between the transverse magnetization vector immediately after an RF pulse and that after the next pulse. The TR was varied from 4 to 100 ms for the T_1-FFE sequence and from 4 to 25 ms for the SSFP sequences. For each TR, θ was varied until the highest sensitivity was obtained. To reduce the number of variables, the echo time in the calculations was kept constant for the T_1-FFE calculations (TE = 2 ms) and was set to TR/2 for the R-FFE and B-FFE sequences.
The SNR and CNR enhancements of the SSFP sequences not only depend on the sequence parameters TR and the flip angle θ, as for the T_1-FFE, but also on the phase advance ϕ. For treatment of its effect, we distinguished two contributions of the phase advance

$$\phi = \alpha + \beta. \tag{7.17}$$

α is the controlled position-independent phase difference between the successive RF pulses, and β the position dependent difference, *e.g.* caused by field inhomogeneities. By definition, the B-FFE sequence alternates the RF phase for successive RF pulses, *i.e.* α=180°, and R-FFE has the same phase for all RF pulses, *i.e.* α=0°. Signal characteristics were calculated for the full range of ϕ between 0° and 180°. The phase advance is incorporated in the equations by replacing $\omega\tau$ in Equation 7.2 by ϕ.
When using short TRs, high SAR can become a concern. A simple model was used for calculating the SAR [241]. For ease of comparison between T_1-FFE, B-FFE and R-FFE, the SAR was normalized using the T_1-FFE sequence with TR = 4 ms as a reference.

Methods

In vitro

Six sample tubes (diameter = 22 mm) each containing a $MnCl^2$ solution (13 mg/l) with increasing concentrations of 0, 0.04, 0.08, 0.12, 0.16, and 0.20 mM of Gd-DTPA (Magnevist, Berlex Inc., Montville, NJ) were bundled. In Figure 7.4 the samples are referred to in this order as sample 1 to 6. Relaxation times of the samples were determined with a 1.5T MRI scanner (Philips Medical Systems, Best) in spectroscopy mode using a PRESS sequence with variable echo times or variable inversion recovery times for T_2 and T_1, respectively. The observed T_2/T_1 values of the six solutions at 1.5T were 215/1406, 209/1197, 203/1007, 193/852, 181/729, and 175/663 ms/ms. The samples were put in a head-coil and imaged with the 1.5T MRI scanner. The position of the samples in the bundle was as shown in Figure 7.5A. For TR, we aimed at a value of 4 ms in accordance with calculations. The MRI system however was not capable of reaching this low value for high flip angles and therefore somewhat higher values were used experimentally instead, as summarized in Table 7.1. Other imaging parameters were: matrix = 128x128, NSA = 8, slice thickness = 5 mm and FOV = 16x16 cm^2. To reach steady state, a run-in period of 0.5 s was used. Prior to the measurements, the B_0 field was shimmed locally and the scan preparation parameters were fixed. Single slice scans using T_1-FFE (RF-spoiled gradient echo), B-FFE and R-FFE sequences were carried out at a range of flip angles and the images were recorded. The phase advance in the SSFP sequences had its nominal values of $\alpha = 0°$ for R-FFE and $\alpha = 180°$ for B-FFE.
The images were analyzed by calculating the mean values of the signal in regions of interest (ROIs) in the 6 samples. The SNRs were determined by dividing these mean signal intensities by the standard deviation of the noise in an ROI outside the samples (see Fig. 7.5A) for each flip angle. The CNR enhancements of the Gd-DTPA containing samples were calculated at each flip angle by subtracting the SNR of the reference sample (sample

Table 7.1: TR, TE, and receiver bandwidth (BW) for the T_1-FFE, B-FFE, and R-FFE used in the *in vitro* and *in vivo* measurements.

	1.5T *in vitro*			1.5T *in vivo*			3T *in vivo*		
	TR [ms]	TE [ms]	BW [kHz]	TR [ms]	TE [ms]	BW [kHz]	TR [ms]	TE [ms]	BW [kHz]
T_1-FFE	3.6-7.4	1.7-1.9	63.9	3.5-4.2	1.6	63.9	3.8	1.5	127.8
B-FFE	3.6-6.2	1.9	63.9	3.5-5.5	1.7	63.9	3.8	1.9	127.8
R-FFE	3.6-6.2	1.9	63.9	3.5	1.7	63.9	3.8	1.9	127.8

with [Gd-DTPA] = 0) from their SNRs. The Gd-DTPA sensitivity S (see also Theory) was then obtained by a linear fit of the CNR enhancements as function of the Gd-DTPA concentration.

In vivo

For the *in vivo* measurements a head-coil was used to scan a transversal slice in the brain of a healthy volunteer in a 1.5 and a 3T MRI scanner (Philips Medical Systems, Best, the Netherlands). Survey scans were used to position the transversal slice in the frontal and parietal lobe parallel to the lateral ventricles. For the 1.5T measurements, a volume was selected inside the cranium for local B_0 shimming and determination of the local resonance frequency. This volume had a thickness of 1 cm and width and height as indicated by the white rectangle in Fig. 7.7C. TR, TE, and bandwidth are summarized in Table 7.1. Other imaging parameters used were: matrix = 128x128, NSA = 1, slice thickness = 5 mm and FOV = 23x23 cm^2. To approach steady state, a run in period of 0.5 s was used. The 3T measurements differed in comparison to the 1.5T measurements in the following parameters: matrix = 224x179, NSA = 2, slice thickness = 4 mm and FOV = 25x20 cm^2. No special local B_0 shimming was performed, but standard B_0 shimming and resonance frequency determination procedures were used. The TRs and TEs of the T_1-FFE, B-FFE and R-FFE sequences were comparable to the 1.5T measurements (see Table 7.1). Images with a range of different flip angles were acquired with the T_1-FFE, B-FFE and R-FFE sequences. The total scan time was approximately one second in all cases.
For analysis of the SNR of these *in vivo* images one ROI was chosen outside the cranium for determination of the noise-level and two ROIs were symmetrically selected in the left and right hemispheres. The analysis method was identical to that described above for the *in vitro* images. To test the degree of in-plane SNR homogeneity, the mean SNR in the two cerebral ROIs as well as the difference of the SNR in the two cerebral ROIs were calculated.

Data analysis

The analyses of the *in vitro* and *in vivo* measurements were done using Matlab 6.1 (The Mathworks, Inc., Natick, MA).

Results

Calculations

Figure 7.2 shows a surface plot of the SNR of the SSFP sequences as a function of flip angle θ and phase advance ϕ, calculated using TR = 4 ms, T_1 = 1406 ms and T_2 = 215 ms, corresponding to values of the reference sample at 1.5T. The range of ϕ was chosen between 0° and 180°. R-FFE and B-FFE constitute the extremes of this range, when the phase accumulation β due to local field inhomogeneities is omitted. The surface has a ridge (solid bold line), where the signal intensity has a constant maximum value. For R-FFE the flip angle at which this maximum occurs is $\theta = 0.5°$, much lower as the value $\theta = 43°$ for the B-FFE. The figure furthermore shows that the signal of R-FFE is very sensitive to phase advance differences, since its narrow peak indicates rapid changes in the signal as function of the phase advance. Consequently, the requirement for field homogeneity is considerably more stringent for R-FFE than for B-FFE.
Figure 7.3A shows $S_{0.2}$ as function of TR of the T_1-FFE sequence when (for each TR) θ is optimized to maximize its value. $S_{0.2}$ displays a small decrease with increasing TR. The saw tooth pattern at higher TR is due to the constant TR times the number of averages and the fact that we have allowed only integer number of averages. In contrast, both SSFP sequences (Fig. 7.3B) benefit strongly from short TR and the highest $S_{0.2}$ occurs at the shortest TR shown (TR = 4 ms). R-FFE has a higher $S_{0.2}$ than B-FFE. Figure 7.3C shows the CNR enhancements as a function of the Gd-DTPA concentration for the optimal flip angles, which for TR = 4 ms were 9°, 76° and 1° for T_1-FFE, B-FFE and

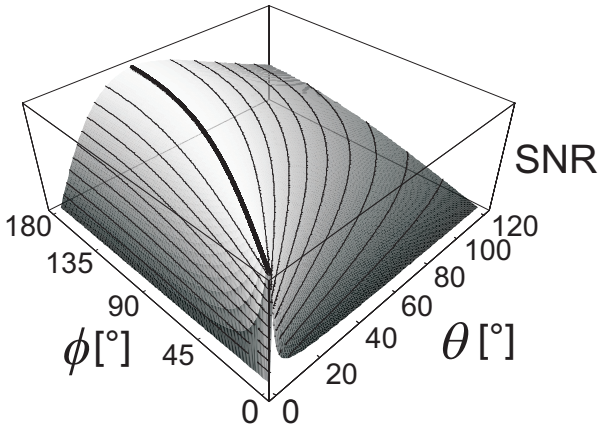

Figure 7.2: Calculated steady state signal of the SSFP sequences as function of the flip angle θ and phase advance ϕ. The lines on the surface are contour lines and the solid bold line represents the contour line at maximum signal.

R-FFE, respectively. The resulting Gd-DTPA sensitivities $S_{0.2}$ were 61, 220, and 276 mM^{-1} for T_1-FFE, B-FFE, and R-FFE. The linearity of the CNR enhancement curve for the R-FFE curve is shown to be better than that of the other curves. This is caused by the fact that in that method the sharp dependence of flip angle on enhancement plays a role, so that for concentrations below 0.2 mM, the flip angle no longer corresponds to maximum CNR enhancement. Using the same set of calculation parameters, Figure 7.3D depicts the effect of phase advance on the flip angle that yields maximal SNR and $S_{0.2}$. The figure illustrates two important points concerning SNR and sensitivity: (a) B-FFE is less sensitive to phase advance than R-FFE; (b) the flip angles for optimal SNR and sensitivity are essentially identical for R-FFE, while differing by more than 20° for B-FFE.

Figure 7.4 shows the normalized SAR as function of TR using the same parameters as in Figs. 7.3A and B. It is evident that large differences in SAR exist between the sequences. B-FFE generates a SAR that is 10 times higher than that of T_1-FFE and 100 times higher than that of R-FFE.

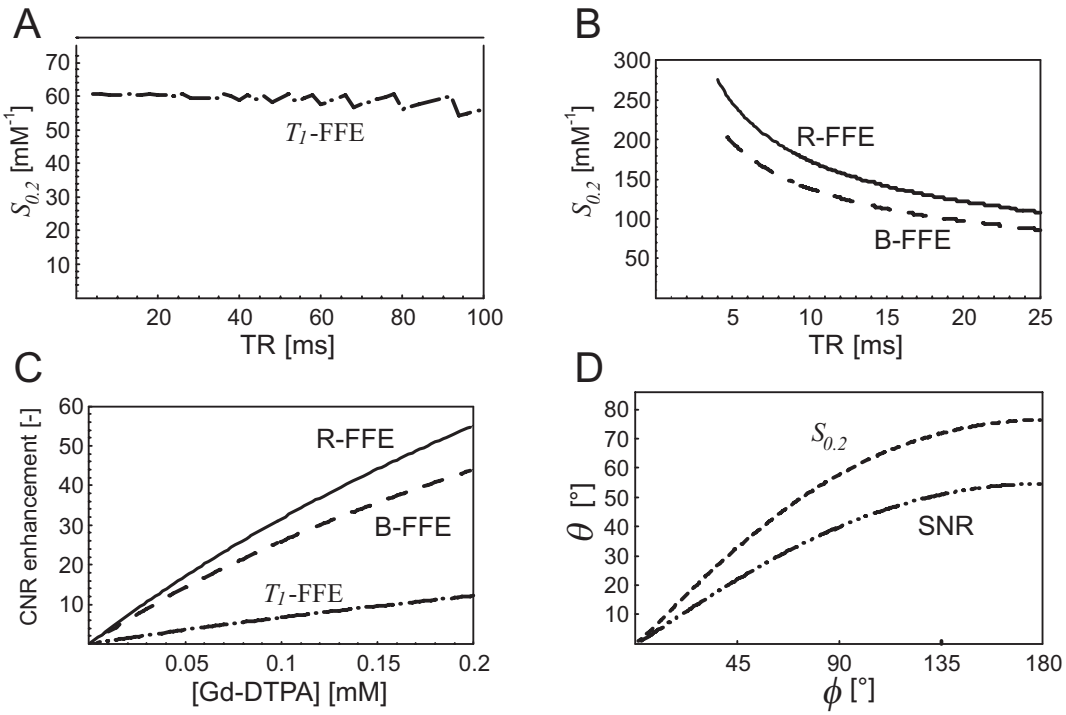

Figure 7.3: A, B: Calculated Gd-DTPA sensitivity for a 0.2 mM Gd-DTPA solution ($S_{0.2}$) at optimal flip angle as a function of TR for (A) T_1-FFE (dash dotted), (B) B-FFE (dashed, $\phi = 180°$) and R-FFE (solid, $\phi = 0°$). (C) Calculated CNR enhancement at optimal flip angle as function of the Gd-DTPA concentration for T_1-FFE (dash dotted), B-FFE (dashed) and R-FFE (solid). D: Calculated optimal flip angle θ for the SSFP sequences as function of the phase advance ϕ for maximal SNR (dashed) and maximal $S_{0.2}$ (dash dotted).

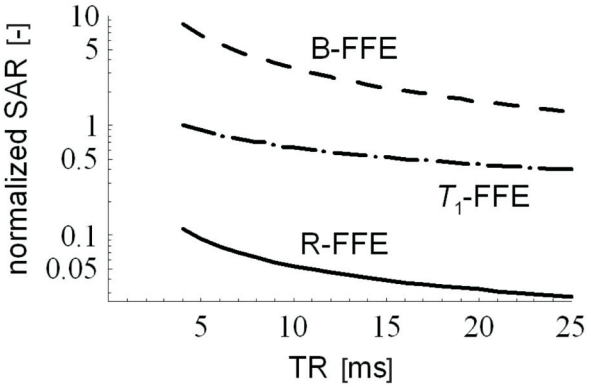

Figure 7.4: Normalized SAR for T_1-FFE (dash dotted), B-FFE (dashed) and R-FFE (solid) with the same parameters as used in Figs. 7.3A and B. The calculated SARs were normalized to the SAR value for the T_1-FFE sequence at TR = 4 ms.

In vitro measurements

The reference sample had a $T_1 = 1406$ ms and $T_2 = 215$ ms at 1.5 Tesla, which is comparable to $T_1 = 1434 \pm 48$ ms and $T_2 = 254 \pm 26$ ms at 23 °C reported for arterial blood at 1.5T [242]. The relaxivities r_1 and r_2 of the Gd-DTPA solutions at 1.5T were 4.1 ($R^2 = 0.996$) and 5.5 mM 1s 1 ($R^2 = 0.979$), respectively.

Figure 7.5A shows the R-FFE image of the 6 sample tubes recorded with a flip angle $\theta = 30°$. Although the B_0 magnetic field was shimmed locally, the R-FFE images displayed a so-called banding artifact, most clearly visible in sample 1 and 3. This effect was absent in the images collected with T_1-FFE and B-FFE (not shown). A detailed analysis of this banding artifact was carried out in order to make sure that R-FFE behaved like a true SSFP sequence. We argued that for R-FFE, even in the presence of additional phase advance due to field inhomogeneities ($\beta \neq 0$), the same maximum signal intensity should be reached for each pixel, be it at another optimal flip angle in accordance with the ridge seen in Fig. 7.3. This was indeed observed experimentally. Figure 7.5B demonstrates that the banding artifact changed appearance, when the flip angle was changed to 60°. Figure 7.5C shows a composite image in which per pixel from the signals at all observed flip angles the maximum signal intensity is displayed. Figure 7.5D is the corresponding map of flip angles. Indeed Fig. 7.5C shows that the maximum signal is almost constant throughout the phantom; the banding artifact is almost invisible. The dark rim in Fig. 7.5B corresponds to very small flip angles ($< 3°$) in Fig. 7.5D.

The SNR of the 6 samples with different Gd-DTPA concentrations as function of the RF pulse flip angle θ is shown in Figs. 7.6A, B and C for T_1-FFE, B-FFE, and R-FFE, respectively. R-FFE and B-FFE have a maximum SNR that is approximately the same and considerably higher than for T_1-FFE, in agreement with the calculations. The optimum flip angle at which this maximum in SNR occurs is higher than theoretically predicted for

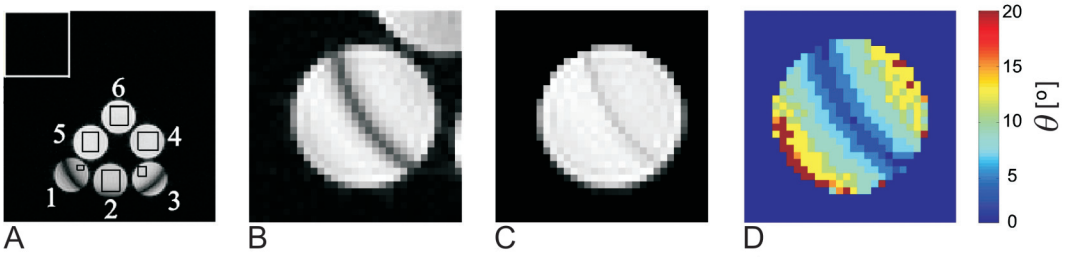

Figure 7.5: A: R-FFE image (TR = 4 ms, TE = 2 ms, $\theta = 30°$) of the 6 sample tubes. The black rectangles in the tubes are the ROIs used for data analysis. The white rectangle in the upper left corner is the ROI used to determine the noise level. The ROIs in tube 1 and 3 were placed outside the banding artifact. B: R-FFE image of sample 1 ($\theta = 65°$), showing a different shape of the banding artifact at a higher flip angle. C: Composite image in which per pixel from the signals at all measured flip angles the maximum signal is displayed. D: Map of optimal flip angles corresponding to image (C), color coded according to the scale on the right.

R-FFE as well as B-FFE (Fig. 7.3D). For both SSFP sequences the optimum flip angle shifts to higher values in a linear fashion with Gd-DTPA concentration (not shown). The CNR enhancement of the different samples as a function of the Gd-DTPA concentration is plotted in Fig. 7.6D. The optimum flip angles for maximum sensitivity were 15°, 125° and 65° for T_1-FFE, B-FFE and R-FFE, respectively. The Gd-DTPA sensitivities for the three sequences were essentially constant in the range of concentrations measured, although the calculations predicted a decreasing sensitivity at higher concentrations (Fig. 7.3C). The Gd-DTPA sensitivities S were 49, 184, and 305 mM^{-1} for T_1-FFE, B-FFE, and R-FFE, respectively. Because these values depend on the noise level in the measurements it is more useful to consider the relative sensitivities here, which are 1, 3.8, and 6.2 for T_1-FFE, B-FFE, and R-FFE. These numbers are in good agreement with the calculations presented in Fig. 7.3C and show that R-FFE has a more than six fold improved sensitivity at 1.5T for the detection of low concentrations of T_1 lowering contrast agent as compared to traditional T_1-FFE.

In vivo measurements

To demonstrate practical *in vivo* feasibility and applicability, MR images at 1.5 and 3T of the cerebrum of a healthy volunteer using the three sequences at maximum SNR are presented in Figure 7.7. The images were scaled to their noise level such that image brightness is a direct measure for SNR. Flip angles that resulted in maximum SNR were 15°, 70° and 10° at 1.5T and 10°, 80° and 1.5° at 3T for T_1-FFE, B-FFE and R-FFE, respectively. Banding artifacts for R-FFE such as in Fig. 7.5 were not observed, although the signal intensity in the frontal and occipital cortex was lower which could be a manifestation

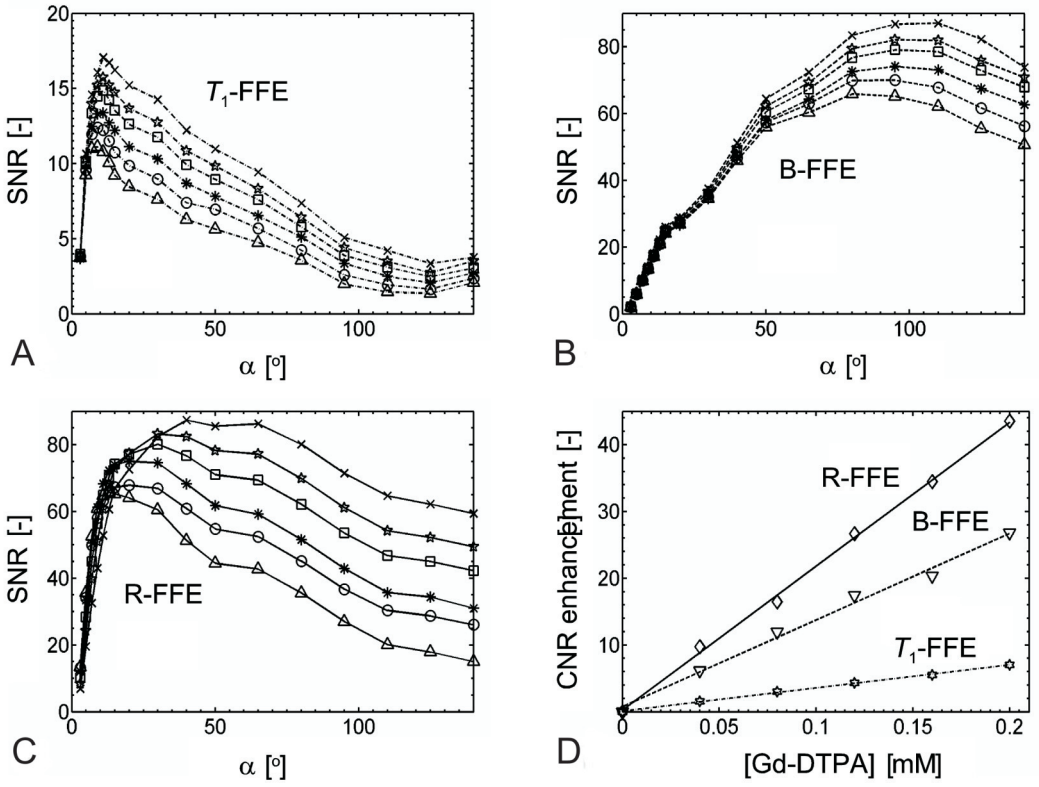

Figure 7.6: Experimental SNR of (A) T_1-FFE, (B) B-FFE and (C) R-FFE sequences for the 6 samples with Gd-DTPA concentrations of (triangle) 0, (circle) 0.04, (asterix) 0.08, (square) 0.12, (star) 0.16, and (cross) 0.20 mM. D: CNR enhancement as a function of Gd-DTPA for (star) T_1-FE, (triangle down) B-FFE and (lozenge) R-FFE. Optimum flip angles were 15°, 125° and 65° for T_1-FFE, B-FFE and R-FFE, respectively. The lines are linear fits with $R^2 = 0.998$, 0.992 and 0.998 for T_1-FFE, B-FFE and R-FFE, respectively.

of that artifact. Signal intensity throughout the brain was in general less homogeneous in the R-FFE images as compared to the T_1-FFE and B-FFE images. Nevertheless, fair image quality was obtained in the volume that was shimmed. The images acquired with B-FFE and R-FFE (Figs. 7.7B, C, F and G) had a much higher SNR than those obtained with the T_1-FFE (Figs. 7.7A and E).

The mean SNR measured within the ROIs are plotted as function of the flip angle in Fig. 7.7D (1.5T) and Fig. 7.7H (3T) for the three sequences. The R-FFE image had the highest maximum SNR. The peak in the SNR as function of flip angle for this sequence was very narrow in comparison with the *in vitro* measurements and at 3T this peak was narrower than at 1.5T. As a measure of the homogeneity of the images, the difference in the mean SNR between the ROIs (upper error bars) and the standard deviation of the pixel values in each ROI (lower error bars) were calculated. The standard deviation of the pixel values in each ROI was higher for R-FFE than for T_1-FFE and B-FFE, indicating

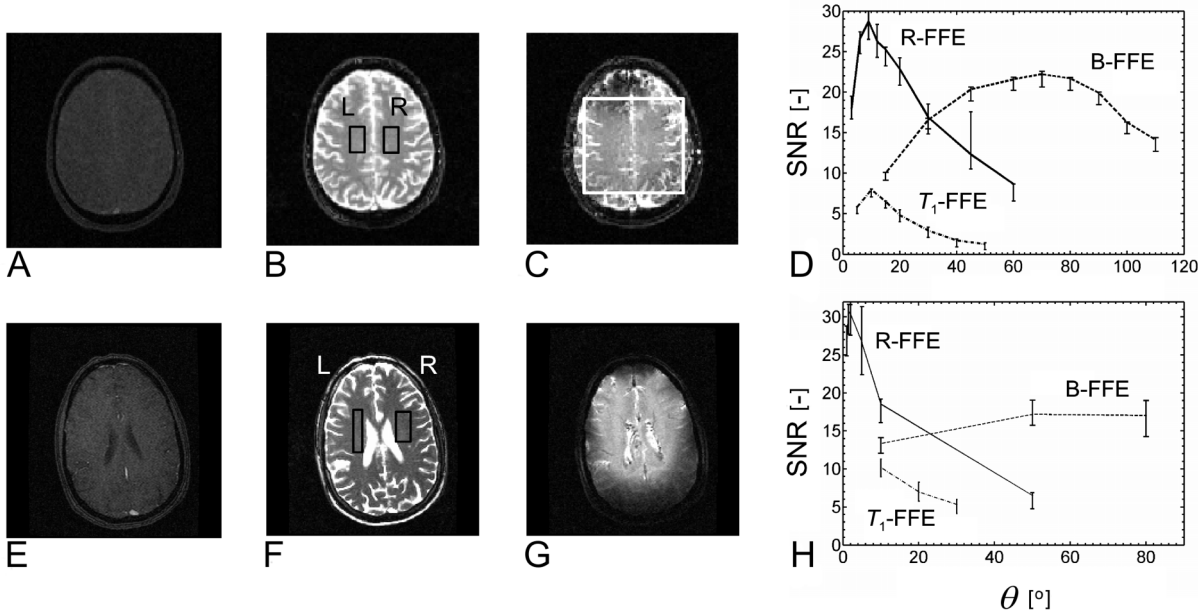

Figure 7.7: Transverse MR images of the brain of human volunteers measured at 1.5T (A, B, C) and 3T (E, F,G), with (A, E) T_1-FFE, (B,F) B-FFE and (C, G) R-FFE. The black rectangles (L, R) in (B, F) were used for calculating the SNR (D, H). The white rectangle in (C) denotes the local shimming area. (D, H) SNR as function of the flip angle for T_1-FFE (dash dotted), B-FFE (dashed) and R-FFE (solid). The upper errorbar is the difference in the mean SNR between the left and right ROIs, whereas the lower errorbar represents the mean of the standard deviation of the pixel values in both ROIs.

more inhomogeneity for the R-FFE images.

Discussion

CNR enhancement

For molecular imaging applications not only the improved sensitivity to low concentrations of contrast agent of the R-FFE sequence is important. Also, linearity between the detected signal and the local label concentration is essential for analysis and quantification. The CNR enhancement of the commonly used T_1-FFE increases linearly with the concentration of the T_1 lowering contrast agent. The *in vitro* measurements showed that the CNR enhancements of the R-FFE and B-FFE sequences depend almost linearly on the Gd-DTPA concentration as well, even though Haacke *et al.* [178] have predicted a linear relationship between the SNR and the square root of T_2/T_1 for SSFP sequences. This relationship was confirmed by our calculations although there is a clear difference between B-FFE and R-FFE. The concentration range of Gd-DTPA used in our experiments was

likely not large enough to detect substantial deviations from linearity. A high linearity for T_1-FFE and B-TFE was recently also found by Perrin *et al.* [238]. These authors found a sensitivity for T_1-FFE, that is in good agreement with our findings, but a substantially lower sensitivity for B-TFE. This is probably caused by a combination of the facts that Perrin and coworkers used different flip angles and TRs for the determination of the sensitivities and a different reference sample that had other T_1 and T_2 values.
Experimental data on the relation between SNR and flip angle as well as the flip angle at which the SNR and sensitivity are maximal seem not in agreement with the calculations. However, a direct comparison between data and calculations is probably not valid since we did not account for the slice profile of our 2D slice selective images. For a typical slice profile, the experimental effective flip angle will be lower than the nominal flip angle, which probably implies better agreement between experiment and calculations than the figures suggest.

R-FFE versus B-FFE and T_1-FFE

R-FFE is a less well-known SSFP sequence. The sequence is characterized by the continuous rephasing of magnetization by the gradients during the readout and the RF pulse, while keeping the transversal phase difference between rephasing spins and RF pulse constant ($\alpha = 0°$). The steady state echo of R-FFE and B-FFE is the result of the cumulative spin configurations of all the previous RF pulses. Due to this partial recycling of the magnetization the sequences are very prone to artifacts. SNR homogeneity within a slice for SSFP sequences is therefore typically less than for T_1-FFE, which involves RF- or gradient-based procedures for spoiling the echoes generated by preceding RF pulses. Moreover, R-FFE is more susceptible to these artifacts than B-FFE, due to the narrow optimal range of flip angles and high sensitivity to the phase advance (Fig. 7.2). At the same time, this narrow maximum has the advantage that a higher Gd-DTPA sensitivity is generated by the R-FFE sequence, because a small change in the position of the maximum due to the contrast agent leads to a large change in SNR.
Since the R-FFE sequence is very demanding in terms of B_1 and B_0 field homogeneity, which become more difficult to control at high field strengths, B-FFE might seem preferable at higher fields, despite its somewhat lower sensitivity for the detection of paramagnetic contrast agents. Nevertheless, in particular at high fields, the short TR used with the SSFP sequences leads to an extremely high SAR for B-FFE. R-FFE offers a solution to this problem since high SNR and sensitivity can be obtained at very low flip angles, reducing the SAR by a factor on the order of 100 (Fig. 7.4).
The flip angle dependency of the SNR of T_1-FFE and B-FFE agree to a large extent with the calculations. For R-FFE, however, there seems to be a discrepancy. Most notably, the sharp peak in the SNR as function of flip angle (Fig. 7.2) is not reproduced experimen-

tally (Fig. 7.6). On closer inspection, however, the experimental flip angle dependency of the SNR resembles the calculations with a finite phase advance ϕ shown in Fig. 7.2. Therefore we think that there was an offset between the RF pulse frequency and the local resonance frequency, resulting in a small phase advance ϕ between successive RF pulses. Probably the only area in the phantom in which $\phi = 0$ was inside the banding artifact itself, where the flip angle for maximum SNR was extremely low (approximately 1°) in agreement with the theoretical predictions. One can note that much of the advantages of R-FFE remain existent when a phase advance is present. With increasing phase advance there will be a gradual shift in SAR level as well as Gd-DTPA sensitivity towards the B-FFE situation. As long as the phase advance is small, the optimal flip angle will remain much smaller than for B-FFE so that SAR problems still are avoided. The tolerance of the R-FFE scan to field inhomogeneities at a small phase shift is increased compared to that in zero phase shift R-FFE.

In vivo applicability of R-FFE

Numerous publications on SSFP sequences have emphasized the need of phase alternation to obtain sufficient stability for imaging. In this work we have demonstrated the feasibility of SSFP imaging without phase alternation. The images do not have perfect signal homogeneity. Figures 7.7D and H showed that the standard deviation of the pixel values in each ROI was higher for R-FFE than for T_1-FFE and B-FFE, and that effect points to signal inhomogeneity in the image. It probably is a sign of the sensitivity of the R-FFE scan to field inhomogeneity. The images in Figure 7.7 support that proposition. The shimming apparently has led to a flat field in the centre of the slice and deviations near the edge of the brain (Figs. 7.7C and G) and in addition near the nasal cavity (Fig. 7.7C). Nevertheless, the accuracy and reproducibility of the shimming and the stability of the system during the scan was sufficient to produce R-FFE images at a range of flip angles, at two field strengths.

Maximum signal intensity *in vitro* (Figs. 7.6B and C) was reached at different flip angles as compared to *in vivo* (Figs. 7.7D and H), both for R-FFE as well as for B-FFE. Additionally, maximum intensities were not equal for R-FFE and B-FFE, in contrast to the calculations shown in Figure 7.2. A possible explanation for these differences can be found in the work of Bieri *et al.* [243]. They proposed that RF pulses with large flip angles in a sequence with short TR saturate macromolecules in the brain tissue. This on resonance magnetization transfer can lead to attenuation of the signal intensity up to a factor of 2. Indeed, when comparing the *in vivo* R-FFE (low flip angle) with the B-FFE (large flip angle) we observe a factor of 1.3 and 2 intensity difference in the brain at 1.5 and 3T, respectively, while for the *in vitro* measurements maximum signal intensities are almost equal, in agreement with the findings of Bieri *et al.* [243]. The difference between

1.5 and 3T might be explained by the fact that the T_1 in the brain at 3T is longer as compared to 1.5T, leading to a higher magnetization transfer attenuation [244], as well as the fact that maximum signal intensity for R-FFE at 3T is reached at lower flip angles. The possible clinical use of R-FFE scans is as yet difficult to indicate. Its low SAR suggests potential use at high field strength, at short TR (< 4 ms) and for repeated dynamic scans. Its high Gd-DTPA sensitivity suggests potential use in molecular imaging. In our limited practice with R-FFE imaging, we found it impossible to shim the whole brain to such an extent that the R-FFE images were free from artifacts. Nevertheless, to benefit from the advantages of the R-FFE sequence for molecular imaging, the following workflow is suggested. The first step is to make an anatomical image with a conventional sequence in which a specific ROI is selected for local shimming. Within this ROI the local Larmor frequency is determined with optimal shimming parameters. A small difference between the Larmor frequency and the transmit frequency is applied inducing a small phase advance and a flip angle is selected to maximize the signal in the centre of the ROI at that particular phase advance, forcing the remaining banding artifacts out of the ROI. Pre contrast injection images are made with these settings. Dynamic post contrast images can then be collected. For analysis, the pre-images are subtracted from the post-images and with a segmentation algorithm the data can be presented as an overlay on the anatomical images.

Conclusion

The signal characteristics for the detection of low contrast agent concentrations were evaluated of the R-FFE sequence. In contrast to other balanced SSFP sequences, R-FFE does not involve a controlled 180° phase advance between successive RF pulses. Theoretically and experimentally it was shown that the pulse sequence combines a high sensitivity for the detection of T_1 lowering contrast agents with a low SAR. In vivo applicability of the sequence was demonstrated in brain scans of human volunteers at 1.5 and 3T.

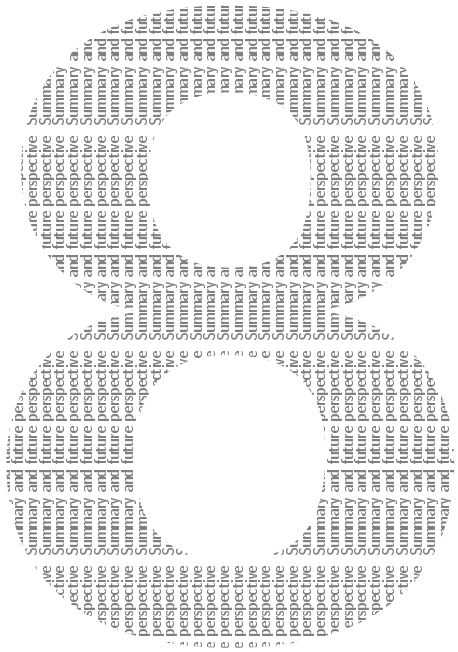

Summary and future perspective

Summary

The interest in *in vivo* imaging of the mouse heart has grown tremendously the last decade by developments in gene technology and molecular biology. Magnetic Resonance Imaging (MRI) is a non-invasive technique which not only acquires tomographic images but combines these with measurements of in vivo physiological parameters.
The size and the beating rate of a mouse heart challenge the MR technology. For motion artifact free images MRI scanning demands a setup which measures and controls the different physiological parameters of the mouse accurately. Motion artifact free images are made by synchronization of the cardiac cycle with the MR acquisition. The synchronization is traditionally done by prospective ECG triggering and respiratory gating. We introduced a navigator echo technique which makes the measurement of the ECG and respiration obsolete. The second advantage of the navigator echo technique is the steady-state signal acquisition which is important for obtaining robust contrast in the images. The steady-state comes at the cost of a lower signal to noise ratio leading to some differences in measuring the end-systolic volume of the mouse heart as compared to the prospective method.
The main disadvantage of a purely tomographic imaging technique is that the images only yield a qualitative classification of the mouse heart morphology. For making the images quantitative (*e.g.* to do volume measurements), segmentations should be performed to separate the mouse heart from surrounding tissue. It is very time consuming to do this manually, which will slow down the analysis speed of large mouse populations. In this thesis it was shown that automatic segmentation is capable to reduce the analysis time with comparable results as the inter-observer variability.
The navigator echo technique was also applied for measurements of the aorta diameter of two different (Smtn-$B^{+/+}$) mouse genotypes. Smtn-$B^{-/-}$ mice had an impaired atrial contractility and higher mean atrial pressure. The aorta diameter of Smtn-$B^{-/-}$ mice expanded two times more during the cardiac cycle and Smtn-$B^{-/-}$ group had a higher left ventricle mass and higher ejection fraction compared to the Smtn-$B^{+/+}$ mice. The smoothelin-B study demonstrated that small differences in global functional parameters between different genotypes can be characterized by mouse cardiac MRI.
MRI is not the only imaging modality that can be applied to determine global functional parameters of infarcted mouse hearts. Different studies of infarcted mice reported comparisons of global functional parameters between MRI and computed tomography, MRI and echocardiography and MRI, as well as pressure-volume conductance micro-catheters. New developments in nuclear imaging techniques (*e.g.* positron emission tomography (PET)) make them also applicable for small animal imaging. The advantage of nuclear techniques is the intrinsically high sensitivity for radioactive labels. This leads to that the toxicity of these labeled molecular structures becomes a minor issue. We compared

global functional parameters and infarct sizes between MRI and PET as determined by contrast enhanced MRI and FDG-PET, respectively, in a control and an infarcted mouse group. The global functional parameters: end-diastolic volume, end-systolic volume and ejection fraction correlated very well between PET and MRI. The infarct size measures were significantly different between MRI and PET. We concluded that both techniques are capable of measuring global functional parameters in different mouse groups. Furthermore, a very high correlation was found between MRI determined ejection fraction and three different MR infarct size measures.
Imaging of disease processes at the cellular or molecular level with MRI is only possible with the aid of an amplification strategy using targeted contrast agents. MRI has a relatively low sensitivity to detect these contrast agents. A novel fast imaging sequence, called Rephased-FFE, was used for an in vitro study and a 6 fold sensitivity enhancement was found for Gd-DTPA compared to a conventional MRI sequence when run on a 1.5 Tesla MRI scanner.

Future perspective

In the preceding chapters it was shown that mouse cardiac MRI is moving towards a one-button measurement for global functional parameters. MRI triggering and segmentation can be performed almost automatically, but stabilization of the physiology of the anaesthetized animal and the planning of the short-axis orientation is still work of an expert. We found that great care should be taken to create well-controlled conditions inside the scanner to maintain a constant heart rate during the experiments. Nowadays mouse cardiac MRI is less well-developed than human cardiac MRI. But the gap between both disciplines is slowly closed by manufacturers and academic groups around the globe. Although mice and men have their specific requirements, developments in mouse cardiac MRI could be potentially translated to the human situation. Presently, this is far from common practice. First mouse cardiac MRI should make the step towards multiple coil arrays, to have the full benefit of measuring more MRI signals simultaneously and increasing the examination speed for a higher throughput. We examined SSFP imaging of the mouse heart to benefit from the higher signal or contrast to noise ratio as well as the higher sensitivity for detecting paramagnetic contrast agent Gd-DTPA (see Chapter 7). Important is to use a navigator echo to maintain the steady state magnetization and use the retrospective triggering and gating technique, developed in Chapter 2, for reconstruction of motion artifact free CINE MR images. The problem we encountered was to suppress the magnetization of the blood within the SSFP sequence [245] which led to large phase artifacts in the image when blood moved out of the slice.
The next step to the one-button measurement for global functional parameters will be an automatic planning procedure based on a navigator echo or image interpretation algo-

rithm. This has already been developed for human MRI scanners [246]. The analysis of data from more sophisticated mouse cardiac MRI techniques, like MR tagging, velocity encoding, contrast enhanced MRI or perfusion MRI is so complicated that for the near future an expert remains needed to deal with the information and interpretation.
Another trend is to combine different imaging modalities within the same device or to use software to overlay the separately acquired images. This was explored in Chapter 6 for the combination of MRI and PET, but a large effort is needed to develop software which is capable of handling the information density and to analyses the images. In the coming decade it will become clear which development is the best: one single machine combining the different image modalities or developing software to combine digitally the different images from separate dedicated machines. Mouse cardiac MRI is a challenging field that has a bright future.

References

[1] W Einthoven and JH Wieringa. Ungleichartige Vaguswirkungen auf das Herz, elektrokardiographisch untersucht. *Pfluegers Archiv European Journal of Physiology*, 149(1):48–64, 1912.

[2] AC Guyton and JE Hall. *Textbook of medical physiology.*

[3] HL Koek, DE Grobbee, and ML Bots. [Trends in cardiovascular morbidity and mortality in the Netherlands, 1980-2000]. *Ned Tijdschr Geneeskd*, 148(1):27–32, January 2004.

[4] WS Post, MG Larson, and D Levy. Impact of left ventricular structure on the incidence of hypertension. The Framingham Heart Study. *Circulation*, 90(1):179–185, July 1994.

[5] WB Kannel and DL McGee. Diabetes and cardiovascular disease. The Framingham study. *JAMA: The Journal of the American Medical Association*, 241(19):2035–2038, May 1979.

[6] JW Magnani and GW Dec. Myocarditis: Current Trends in Diagnosis and Treatment. *Circulation*, 113(6):876–890, February 2006.

[7] S Wild, G Roglic, A Green, R Sicree, and H King. Global Prevalence of Diabetes: Estimates for the year 2000 and projections for 2030. *Diabetes Care*, 27(5):1047–1053, May 2004.

[8] JP Cleutjens, WM Blankesteijn, MJ Daemen, and JF Smits. The infarcted myocardium: simply dead tissue, or a lively target for therapeutic interventions. *Cardiovasc Res*, 44(2):232–241, November 1999.

[9] WM Blankesteijn, E Creemers, E Lutgens, JP Cleutjens, MJ Daemen, and JF Smits. Dynamics of cardiac wound healing following myocardial infarction: observations in genetically altered mice. *Acta Physiol Scand*, 173(1):75–82, September 2001.

[10] Z Yang, SS Berr, WD Gilson, MC Toufektsian, and BA French. Simultaneous evaluation of infarct size and cardiac function in intact mice by contrast-enhanced cardiac

magnetic resonance imaging reveals contractile dysfunction in noninfarcted regions early after myocardial infarction. *Circulation*, 109(9):1161–1167, March 2004.

[11] T Celle De, JP Cleutjens, WM Blankesteijn, JJ Debets, JF Smits, and BJ Janssen. Long-term structural and functional consequences of cardiac ischaemia-reperfusion injury in vivo in mice. *Exp Physiol*, 89(5):605–615, September 2004.

[12] LH Michael, CM Ballantyne, JP Zachariah, KE Gould, JS Pocius, GE Taffet, CJ Hartley, TT Pham, SL Daniel, E Funk, and ML Entman. Myocardial infarction and remodeling in mice: effect of reperfusion. *Am J Physiol*, 277(2).

[13] RY Man and A Bril. Effects of class I anti-arrhythmic drugs in infarcted tissue. *Clin Invest Med*, 14(5):466–475, October 1991.

[14] AL Wit and MR Rosen. Pathophysiologic mechanisms of cardiac arrhythmias. *Am Heart J*, 106(4).

[15] A Wessels and D Sedmera. Developmental anatomy of the heart: a tale of mice and man. *Physiol Genomics*, 15(3):165–176, November 2003.

[16] RE Henson, SK Song, JS Pastorek, JJ Ackerman, and CH Lorenz. Left ventricular torsion is equal in mice and humans. *Am J Physiol Heart Circ Physiol*, 278(4):H1117–H1123, April 2000.

[17] R Zhou, S Pickup, JD Glickson, CH Scott, and VA Ferrari. Assessment of global and regional myocardial function in the mouse using cine and tagged MRI. *Magn Reson Med*, 49(4):760–764, April 2003.

[18] W Liu, MW Ashford, J Chen, MP Watkins, TA Williams, SA Wickline, and X Yu. MR tagging demonstrates quantitative differences in regional ventricular wall motion in mice, rats, and men. *Am J Physiol Heart Circ Physiol*, 291(5):H2515–H2521, November 2006.

[19] ME Stoker, AM Gerdes, and JF May. Regional differences in capillary density and myocyte size in the normal human heart. *Anat Rec*, 202(2):187–191, February 1982.

[20] K Rakusan and J Nagai. Morphometry of arterioles and capillaries in hearts of senescent mice. *Cardiovasc Res*, 28(7):969–972, July 1994.

[21] PA Doevendans, MJ Daemen, ED Muinck de, and JF Smits. Cardiovascular phenotyping in mice. *Cardiovasc Res*, 39(1):34–49, July 1998.

[22] B Swynghedauw. Developmental and functional adaptation of contractile proteins in cardiac and skeletal muscles. *Physiol Rev*, 66(3):710–771, July 1986.

[23] SG Gregory, M Sekhon, J Schein, S Zhao, K Osoegawa, CE Scott, RS Evans, PW Burridge, TV Cox, CA Fox, RD Hutton, IR Mullenger, KJ Phillips, J Smith, J Stalker, GJ Threadgold, E Birney, K Wylie, A Chinwalla, J Wallis, L Hillier, J Carter, T Gaige, S Jaeger, C Kremitzki, D Layman, J Maas, R McGrane, K Mead, R Walker, S Jones, M Smith, J Asano, I Bosdet, S Chan, S Chittaranjan, R Chiu, C Fjell, D Fuhrmann, N Girn, C Gray, R Guin, L Hsiao, M Krzywinski, R Kutsche, SS Lee, C Mathewson, C McLeavy, S Messervier, S Ness, P Pandoh, AL Prabhu, P Saeedi, D Smailus, L Spence, J Stott, S Taylor, W Terpstra, M Tsai, J Vardy, N Wye, G Yang, S Shatsman, B Ayodeji, K Geer, G Tsegaye, A Shvartsbeyn, E Gebregeorgis, M Krol, D Russell, L Overton, JA Malek, M Holmes, M Heaney, J Shetty, T Feldblyum, WC Nierman, JJ Catanese, T Hubbard, RH Waterston, J Rogers, PJ Jong de, CM Fraser, M Marra, JD McPherson, and DR Bentley. A physical map of the mouse genome. *Nature*, 418(6899):743–750, August 2002.

[24] G Chu, K Haghighi, and EG Kranias. From mouse to man: understanding heart failure through genetically altered mouse models. *J Card Fail*, 8(6).

[25] R Weissleder and U Mahmood. Molecular imaging. *Radiology*, 219(2):316–333, May 2001.

[26] FM Siri, LA Jelicks, LA Leinwand, and JM Gardin. Gated magnetic resonance imaging of normal and hypertrophied murine hearts. *Am J Physiol*, 272(5).

[27] JF James, TE Hewett, and J Robbins. Cardiac physiology in transgenic mice. *Circ Res*, 82(4):407–415, March 1998.

[28] D Bryant, L Becker, J Richardson, J Shelton, F Franco, R Peshock, M Thompson, and B Giroir. Cardiac failure in transgenic mice with myocardial expression of tumor necrosis factor-alpha. *Circulation*, 97(14):1375–1381, April 1998.

[29] F Franco, SK Dubois, RM Peshock, and RV Shohet. Magnetic resonance imaging accurately estimates LV mass in a transgenic mouse model of cardiac hypertrophy. *Am J Physiol*, 274(2):H679–H683, February 1998.

[30] F Franco, GD Thomas, B Giroir, D Bryant, MC Bullock, MC Chwialkowski, RG Victor, and RM Peshock. Magnetic resonance imaging and invasive evaluation of development of heart failure in transgenic mice with myocardial expression of tumor necrosis factor-alpha. *Circulation*, 99(3):448–454, January 1999.

[31] SE Slawson, BB Roman, DS Williams, and AP Koretsky. Cardiac MRI of the normal and hypertrophied mouse heart. *Magn Reson Med*, 39(6):980–987, June 1998.

[32] J Ruff, F Wiesmann, KH Hiller, S Voll, M Kienlin von, WR Bauer, E Rommel, S Neubauer, and A Haase. Magnetic resonance microimaging for noninvasive quan-

tification of myocardial function and mass in the mouse. *Magn Reson Med*, 40(1):43–48, July 1998.

[33] F Wiesmann, J Ruff, and A Haase. High-resolution MR imaging in mice. *MAGMA*, 6(2).

[34] P Lanzer, EH Botvinick, NB Schiller, LE Crooks, M Arakawa, L Kaufman, PL Davis, R Herfkens, MJ Lipton, and CB Higgins. Cardiac imaging using gated magnetic resonance. *Radiology*, 150(1):121–127, January 1984.

[35] CB Higgins, BF Byrd, DW Farmer, L Osaki, NH Silverman, and MD Cheitlin. Magnetic resonance imaging in patients with congenital heart disease. *Circulation*, 70(5):851–860, November 1984.

[36] M Brede, K Hadamek, L Meinel, F Wiesmann, J Peters, S Engelhardt, A Simm, A Haase, MJ Lohse, and L Hein. Vascular hypertrophy and increased P70S6 kinase in mice lacking the angiotensin II AT(2) receptor. *Circulation*, 104(21):2602–2607, November 2001.

[37] JR Wilding, JE Schneider, AE Sang, KE Davies, S Neubauer, and K Clarke. Dystrophin- and MLP-deficient mouse hearts: marked differences in morphology and function, but similar accumulation of cytoskeletal proteins. *FASEB J*, 19(1):79–81, January 2005.

[38] AJ Ross, Z Yang, SS Berr, WD Gilson, WC Petersen, JN Oshinski, and BA French. Serial MRI evaluation of cardiac structure and function in mice after reperfused myocardial infarction. *Magn Reson Med*, 47(6):1158–1168, June 2002.

[39] F Wiesmann, A Frydrychowicz, J Rautenberg, R Illinger, E Rommel, A Haase, and S Neubauer. Analysis of right ventricular function in healthy mice and a murine model of heart failure by in vivo MRI. *Am J Physiol Heart Circ Physiol*, 283(3):H1065–H1071, September 2002.

[40] TC Hu, W Bao, SC Lenhard, TR Schaeffer, TL Yue, RN Willette, and BM Jucker. Simultaneous assessment of left-ventricular infarction size, function and tissue viability in a murine model of myocardial infarction by cardiac manganese-enhanced magnetic resonance imaging (MEMRI). *NMR Biomed*, 17(8):620–626, December 2004.

[41] Z Yang, CM Bove, BA French, FH Epstein, SS Berr, JM Dimaria, JJ Gibson, RM Carey, and CM Kramer. Angiotensin II type 2 receptor overexpression preserves left ventricular function after myocardial infarction. *Circulation*, 106(1):106–111, July 2002.

[42] D Engel, R Peshock, RC Armstong, N Sivasubramanian, and DL Mann. Cardiac myocyte apoptosis provokes adverse cardiac remodeling in transgenic mice with targeted TNF overexpression. *Am J Physiol Heart Circ Physiol*, 287(3):H1303–H1311, September 2004.

[43] EA Ashley, J Powers, M Chen, R Kundu, T Finsterbach, A Caffarelli, A Deng, J Eichhorn, R Mahajan, R Agrawal, J Greve, R Robbins, AJ Patterson, D Bernstein, and T Quertermous. The endogenous peptide apelin potently improves cardiac contractility and reduces cardiac loading in vivo. *Cardiovasc Res*, 65(1):73–82, January 2005.

[44] M Nahrendorf, M Spindler, K Hu, L Bauer, O Ritter, P Nordbeck, T Quaschning, KH Hiller, J Wallis, G Ertl, WR Bauer, and S Neubauer. Creatine kinase knockout mice show left ventricular hypertrophy and dilatation, but unaltered remodeling post-myocardial infarction. *Cardiovasc Res*, 65(2):419–427, February 2005.

[45] AV Naumova, VP Chacko, R Ouwerkerk, L Stull, E Marban, and RG Weiss. Xanthine oxidase inhibitors improve energetics and function after infarction in failing mouse hearts. *Am J Physiol Heart Circ Physiol*, 290(2):H837–H843, February 2006.

[46] MC Toufektsian, Z Yang, KM Prasad, L Overbergh, SI Ramos, C Mathieu, J Linden, and BA French. Stimulation of A2A-adenosine receptors after myocardial infarction suppresses inflammatory activation and attenuates contractile dysfunction in the remote left ventricle. *Am J Physiol Heart Circ Physiol*, 290(4):H1410–H1418, April 2006.

[47] T Kofidis, DR Lebl, RJ Swijnenburg, JM Greeve, U Klima, J Gold, C Xu, and RC Robbins. Allopurinol/uricase and ibuprofen enhance engraftment of cardiomyocyte-enriched human embryonic stem cells and improve cardiac function following myocardial injury. *Eur J Cardiothorac Surg*, 29(1):50–55, January 2006.

[48] F Wiesmann, J Ruff, C Dienesch, A Leupold, E Rommel, A Haase, and S Neubauer. Cardiovascular phenotype characterization in mice by high resolution magnetic resonance imaging. *MAGMA*, 11(1).

[49] J Ruff, F Wiesmann, T Lanz, and A Haase. Magnetic resonance imaging of coronary arteries and heart valves in a living mouse: techniques and preliminary results. *J Magn Reson*, 146(2):290–296, October 2000.

[50] F Wiesmann, S Neubauer, A Haase, and L Hein. Can we use vertical bore magnetic resonance scanners for murine cardiovascular phenotype characterization? Influence of upright body position on left ventricular hemodynamics in mice. *J Cardiovasc Magn Reson*, 3(4):311–315, 2001.

[51] FP Rugge van, EE Wall der van, and AV Bruschke. New developments in pharmacologic stress imaging. *Am Heart J*, 124(2):468–485, August 1992.

[52] SP Williams, HP Gerber, FJ Giordano, FV Peale, LJ Bernstein, S Bunting, KR Chien, N Ferrara, and N Bruggen van. Dobutamine stress cine-MRI of cardiac function in the hearts of adult cardiomyocyte-specific VEGF knockout mice. *J Magn Reson Imaging*, 14(4):374–382, October 2001.

[53] TC Hu, RG Pautler, GA MacGowan, and AP Koretsky. Manganese-enhanced MRI of mouse heart during changes in inotropy. *Magn Reson Med*, 46(5):884–890, November 2001.

[54] GE Wesbey, CB Higgins, MT McNamara, BL Engelstad, MJ Lipton, R Sievers, RL Ehman, J Lovin, and RC Brasch. Effect of gadolinium-DTPA on the magnetic relaxation times of normal and infarcted myocardium. *Radiology*, 153(1):165–169, October 1984.

[55] RD White, MM Cassidy, MD Cheitlin, B Emilson, TA Ports, AD Lim, EH Botvinick, NB Schiller, and CB Higgins. Segmental evaluation of left ventricular wall motion after myocardial infarction: magnetic resonance imaging versus echocardiography. *Am Heart J*, 115(1).

[56] EX Wu, CW Towe, and H Tang. MRI cardiac tagging using a sinc-modulated RF pulse train. *Magn Reson Med*, 48(2):389–393, August 2002.

[57] TJ Mosher and MB Smith. A DANTE tagging sequence for the evaluation of translational sample motion. *Magn Reson Med*, 15(2):334–339, August 1990.

[58] AA Young and L Axel. Three-dimensional motion and deformation of the heart wall: estimation with spatial modulation of magnetization–a model-based approach. *Radiology*, 185(1):241–247, October 1992.

[59] FH Epstein, Z Yang, WD Gilson, SS Berr, CM Kramer, and BA French. MR tagging early after myocardial infarction in mice demonstrates contractile dysfunction in adjacent and remote regions. *Magn Reson Med*, 48(2):399–403, August 2002.

[60] AA Young, H Imai, CN Chang, and L Axel. Two-dimensional left ventricular deformation during systole using magnetic resonance imaging with spatial modulation of magnetization. *Circulation*, 89(2):740–752, February 1994.

[61] WD Gilson, Z Yang, BA French, and FH Epstein. Complementary displacement-encoded MRI for contrast-enhanced infarct detection and quantification of myocardial function in mice. *Magn Reson Med*, 51(4):744–752, April 2004.

[62] AH Aletras, RS Balaban, and H Wen. High-resolution strain analysis of the human heart with fast-DENSE. *J Magn Reson*, 140(1):41–57, September 1999.

[63] WD Gilson, Z Yang, BA French, and FH Epstein. Measurement of myocardial mechanics in mice before and after infarction using multislice displacement-encoded MRI with 3D motion encoding. *Am J Physiol Heart Circ Physiol*, 288(3):H1491–H1497, March 2005.

[64] JU Streif, V Herold, M Szimtenings, TE Lanz, M Nahrendorf, F Wiesmann, E Rommel, and A Haase. In vivo time-resolved quantitative motion mapping of the murine myocardium with phase contrast MRI. *Magn Reson Med*, 49(2):315–321, February 2003.

[65] EX Wu, H Tang, KK Wong, and J Wang. Mapping cyclic change of regional myocardial blood volume using steady-state susceptibility effect of iron oxide nanoparticles. *J Magn Reson Imaging*, 19(1):50–58, January 2004.

[66] V Belle, E Kahler, C Waller, E Rommel, S Voll, KH Hiller, WR Bauer, and A Haase. In vivo quantitative mapping of cardiac perfusion in rats using a noninvasive MR spin-labeling method. *J Magn Reson Imaging*, 8(6):1240–1245, November 1998.

[67] F Kober, I Iltis, PJ Cozzone, and M Bernard. Myocardial blood flow mapping in mice using high-resolution spin labeling magnetic resonance imaging: influence of ketamine/xylazine and isoflurane anesthesia. *Magn Reson Med*, 53(3):601–606, March 2005.

[68] JU Streif, M Nahrendorf, KH Hiller, C Waller, F Wiesmann, E Rommel, A Haase, and WR Bauer. In vivo assessment of absolute perfusion and intracapillary blood volume in the murine myocardium by spin labeling magnetic resonance imaging. *Magn Reson Med*, 53(3):584–592, March 2005.

[69] JE Schneider, PJ Cassidy, C Lygate, DJ Tyler, F Wiesmann, SM Grieve, K Hulbert, K Clarke, and S Neubauer. Fast, high-resolution in vivo cine magnetic resonance imaging in normal and failing mouse hearts on a vertical 11.7 T system. *J Magn Reson Imaging*, 18(6):691–701, December 2003.

[70] JE Schneider, KJ Hulbert, CA Lygate, M Hove ten, PJ Cassidy, K Clarke, and S Neubauer. Long-term stability of cardiac function in normal and chronically failing mouse hearts in a vertical-bore MR system. *MAGMA*, 17(3).

[71] U Flogel, T Laussmann, A Godecke, N Abanador, M Schafers, CD Fingas, S Metzger, B Levkau, C Jacoby, and J Schrader. Lack of myoglobin causes a switch in cardiac substrate selection. *Circ Res*, 96(8):e68–e75, April 2005.

[72] PA Bottomley, TH Foster, RE Argersinger, and LM Pfeifer. A review of normal tissue hydrogen NMR relaxation times and relaxation mechanisms from 1-100 MHz:

Dependence on tissue type, NMR frequency, temperature, species, excision and age. *Med Phys*, 11(4):425–448, 1984.

[73] PA Bottomley. Spatial localization in NMR spectroscopy in vivo. *Ann N Y Acad Sci*, 508:333–348, 1987.

[74] VP Chacko, F Aresta, SM Chacko, and RG Weiss. MRI/MRS assessment of in vivo murine cardiac metabolism, morphology, and function at physiological heart rates. *Am J Physiol Heart Circ Physiol*, 279(5):H2218–H2224, November 2000.

[75] RG Weiss, JC Chatham, D Georgakopolous, MJ Charron, T Wallimann, L Kay, B Walzel, Y Wang, DA Kass, G Gerstenblith, and VP Chacko. An increase in the myocardial PCr/ATP ratio in GLUT4 null mice. *FASEB J*, 16(6):613–615, April 2002.

[76] U Flogel, C Jacoby, A Godecke, and J Schrader. In vivo 2D mapping of impaired murine cardiac energetics in NO-induced heart failure. *Magn Reson Med*, 57(1):50–58, January 2007.

[77] T Neuberger, A Greiser, M Nahrendorf, PM Jakob, C Faber, and AG Webb. 23Na microscopy of the mouse heart in vivo using density-weighted chemical shift imaging. *MAGMA*, 17(3).

[78] GA Johnson, GP Cofer, SL Gewalt, and LW Hedlund. Morphologic Phenotyping with MR Microscopy: The Visible Mouse. *Radiology*, 222(3):789–793, March 2002.

[79] PJ Basser, J Mattiello, and D LeBihan. MR diffusion tensor spectroscopy and imaging. *Biophys J*, 66(1):259–267, January 1994.

[80] Y Jiang, K Pandya, O Smithies, and EW Hsu. Three-dimensional diffusion tensor microscopy of fixed mouse hearts. *Magn Reson Med*, 52(3):453–460, September 2004.

[81] D Artemov. Molecular magnetic resonance imaging with targeted contrast agents. *J Cell Biochem*, 90(3):518–524, October 2003.

[82] JR Allport and R Weissleder. In vivo imaging of gene and cell therapies. *Exp Hematol*, 29(11):1237–1246, November 2001.

[83] DH Carr, J Brown, GM Bydder, RE Steiner, HJ Weinmann, U Speck, AS Hall, and IR Young. Gadolinium-DTPA as a contrast agent in MRI: initial clinical experience in 20 patients. *AJR Am J Roentgenol*, 143(2):215–224, August 1984.

[84] GM Lanza, CH Lorenz, SE Fischer, MJ Scott, WP Cacheris, RJ Kaufmann, PJ Gaffney, and SA Wickline. Enhanced detection of thrombi with a novel fibrin-targeted magnetic resonance imaging agent. *Acad Radiol*, 5.

[85] AM Neubauer and SD Caruthers amd FD Hockett. Fluorine cardiovascular magnetic resonance angiography in vivo at 1.5 T with perfluorocarbon nanoparticle contrast agents. *J.Cardiovasc.Magn Reson*, 9.

[86] S Aime, CD Delli, F Fedeli, and E Terreno. A paramagnetic MRI-CEST agent responsive to lactate concentration. *J Am Chem Soc*, 124(32):9364–9365, August 2002.

[87] S Aime, A Barge, CD Delli, F Fedeli, A Mortillaro, FU Nielsen, and E Terreno. Paramagnetic lanthanide(III) complexes as pH-sensitive chemical exchange saturation transfer (CEST) contrast agents for MRI applications. *Magn Reson Med*, 47(4):639–648, April 2002.

[88] V Sharma, GD Luker, and D Piwnica-Worms. Molecular imaging of gene expression and protein function in vivo with PET and SPECT. *J Magn Reson Imaging*, 16(4):336–351, October 2002.

[89] WJ Mulder, GJ Strijkers, AW Griffioen, L Bloois van, G Molema, G Storm, GA Koning, and K Nicolay. A liposomal system for contrast-enhanced magnetic resonance imaging of molecular targets. *Bioconjug Chem*, 15(4):799–806, July 2004.

[90] E Heijman, GJ Strijkers, J Habets, B Janssen, and K Nicolay. Magnetic resonance imaging of regional cardiac function in the mouse. *MAGMA*, 17(3).

[91] BJ Pichler, MS Judenhofer, C Catana, JH Walton, M Kneilling, RE Nutt, SB Siegel, CD Claussen, and SR Cherry. Performance test of an LSO-APD detector in a 7-T MRI scanner for simultaneous PET/MRI. *J Nucl Med*, 47(4):639–647, April 2006.

[92] MS Judenhofer, HF Wehrl, DF Newport, C Catana, SB Siegel, M Becker, A Thielscher, M Kneilling, MP Lichy, M Eichner, K Klingel, G Reischl, S Widmaier, M Rocken, RE Nutt, HJ Machulla, K Uludag, SR Cherry, CD Claussen, and BJ Pichler. Simultaneous PET-MRI: a new approach for functional and morphological imaging. *Nat Med*, 14(4):459–465, April 2008.

[93] AR Hsu, W Cai, A Veeravagu, KA Mohamedali, K Chen, S Kim, H Vogel, LC Hou, V Tse, MG Rosenblum, and X Chen. Multimodality molecular imaging of glioblastoma growth inhibition with vasculature-targeting fusion toxin VEGF121/rGel. *J Nucl Med*, 48(3):445–454, March 2007.

[94] JL Humm, D Ballon, YC Hu, S Ruan, C Chui, PK Tulipano, A Erdi, J Koutcher, K Zakian, M Urano, P Zanzonico, C Mattis, J Dyke, Y Chen, P Harrington, JA O'Donoghue, and CC Ling. A stereotactic method for the three-dimensional registration of multi-modality biologic images in animals: NMR, PET, histology, and autoradiography. *Med Phys*, 30(9):2303–2314, September 2003.

[95] RL Ehman, MT McNamara, M Pallack, H Hricak, and CB Higgins. Magnetic resonance imaging with respiratory gating: techniques and advantages. *AJR Am J Roentgenol*, 143(6):1175–1182, December 1984.

[96] M Nahrendorf, F Wiesmann, KH Hiller, H Han, K Hu, C Waller, J Ruff, A Haase, G Ertl, and WR Bauer. In vivo assessment of cardiac remodeling after myocardial infarction in rats by cine-magnetic resonance imaging. *J Cardiovasc Magn Reson*, 2(3):171–180, 2000.

[97] PJ Cassidy, JE Schneider, SM Grieve, C Lygate, S Neubauer, and K Clarke. Assessment of motion gating strategies for mouse magnetic resonance at high magnetic fields. *J Magn Reson Imaging*, 19(2):229–237, February 2004.

[98] Y Liu, SJ Riederer, and RL Ehman. Magnetization-prepared cardiac imaging using gradient echo acquisition. *Magn Reson Med*, 30(2):271–275, August 1993.

[99] SE Rose, SJ Wilson, FO Zelaya, S Crozier, and DM Doddrell. High resolution high field rodent cardiac imaging with flow enhancement suppression. *Magn Reson Imaging*, 12(8):1183–1190, 1994.

[100] J Bishop, A Feintuch, NA Bock, B Nieman, J Dazai, L Davidson, and RM Henkelman. Retrospective gating for mouse cardiac MRI. *Magn Reson Med*, 55(3):472–477, March 2006.

[101] TA Spraggins. Wireless retrospective gating: application to cine cardiac imaging. *Magn Reson Imaging*, 8(6):675–681, 1990.

[102] RD White, CB Paschal, ME Clampitt, TA Spraggins, and GW Lenz. Electrocardiograph-independent, 'wireless' cardiovascular cine MR imaging. *J Magn Reson Imaging*, 1(3):347–355, May 1991.

[103] A Shankaranarayanan, A Brau, M McConnell, and J Brittain. Self-Navigated 2D SSFP Sequence for Simultaneous Respiratory and Cardiac Motion Detection. *Proc Intl Soc Mag Reson Med*, 14:–, 2006.

[104] ME Crowe, AC Larson, Q Zhang, J Carr, RD White, D Li, and OP Simonetti. Automated rectilinear self-gated cardiac cine imaging. *Magn Reson Med*, 52(4):782–788, October 2004.

[105] B Hiba, N Richard, M Janier, and P Croisille. Cardiac and respiratory double self-gated cine MRI in the mouse at 7 T. *Magn Reson Med*, 55(3):506–513, March 2006.

[106] CJ Echteld Van, MG Nederhoff, BC Boekhorst Te, CW Kolk de Van, MA Jansen, and A Nauerth. Self-gated, wireless cine-MRI allows accurate and time-efficient

analysis of mouse heart function when conventional ECG-and respiratory gated cine MRI fails. *Proc Intl Soc Mag Reson Med*, 14:–, 2006.

[107] A Nauerth, E Heijman, and C Diekmann. Slice refocusing signal for retrospective reconstruction of CINE cardiac MR images. *Proc Intl Soc Mag Reson Med*, 14:–, 2006.

[108] J Frahm, A Haase, and D Matthaei. Rapid NMR imaging of dynamic processes using the FLASH technique. *Magn Reson Med*, 3(2):321–327, April 1986.

[109] Y Wang, PJ Rossman, RC Grimm, SJ Riederer, and RL Ehman. Navigator-echo-based real-time respiratory gating and triggering for reduction of respiration effects in three-dimensional coronary MR angiography. *Radiology*, 198(1):55–60, January 1996.

[110] F Kober, I Iltis, PJ Cozzone, and M Bernard. Cine-MRI assessment of cardiac function in mice anesthetized with ketamine/xylazine and isoflurane. *MAGMA*, 17(3).

[111] MT Vlaardingerbroek and JA Boer den. *Magnetic Resonance Imaging : Theory and practice*. 1999.

[112] SS Berr, RJ Roy, BA French, Z Yang, W Gilson, CM Kramer, and FH Epstein. Black blood gradient echo cine magnetic resonance imaging of the mouse heart. *Magn Reson Med*, 53(5):1074–1079, May 2005.

[113] AC Brau and JH Brittain. Generalized self-navigated motion detection technique: Preliminary investigation in abdominal imaging. *Magn Reson Med*, 55(2):263–270, February 2006.

[114] M Watanabe, Y Hosoda, and DB Longmore. [Left and right ventricular dimensions and functions measured by ECG-gated NMR cardiac imaging]. *J Cardiogr*, 16(2):343–352, June 1986.

[115] H Just, C Holubarsch, and H Friedburg. Estimation of left ventricular volume and mass by magnetic resonance imaging: comparison with quantitative biplane angiocardiography. *Cardiovasc Intervent Radiol*, 10(1):1–4, 1987.

[116] L Stegger, KP Schafers, U Flogel, L Livieratos, S Hermann, C Jacoby, P Keul, EM Conway, O Schober, J Schrader, B Levkau, and M Schafers. Monitoring left ventricular dilation in mice with PET. *J Nucl Med*, 46(9):1516–1521, September 2005.

[117] C Jacoby, A Molojavyi, U Flogel, MW Merx, Z Ding, and J Schrader. Direct comparison of magnetic resonance imaging and conductance microcatheter in the

evaluation of left ventricular function in mice. *Basic Res Cardiol*, 101(1):87–95, January 2006.

[118] NA Bock, NB Konyer, and RM Henkelman. Multiple-mouse MRI. *Magn Reson Med*, 49(1):158–167, January 2003.

[119] PP Wyatt and JA Noble. MAP MRF joint segmentation and registration of medical images. *Med Image Anal*, 7(4):539–552, December 2003.

[120] SS Rensen, VL Thijssen, CJ Vries De, PA Doevendans, SD Detera-Wadleigh, and GJ Eys van. Expression of the smoothelin gene is mediated by alternative promoters. *Cardiovasc Res*, 55(4):850–863, September 2002.

[121] L Maes, B Bijnens, P Suetens, and F Werf de Van. Automated contour detection of the left ventricle in short axis view in 2D echocardiograms. *Machine Vision and Applications*, 6(1):1–9, 1993.

[122] T Simpson. The Invention of a General Method for Determining the Sum of Every 2d, 3d, 4th, or 5th, &c. Term of a Series, Taken in Order; The Sum of the Whole Series Being Known. By Thomas Simpson, FRS. *Philosophical Transactions (1683-1775)*, 50:757–769, 1757.

[123] DL Streiner and GR Norman. 'Precision' and 'accuracy': two terms that are neither. *J Clin Epidemiol*, 59(4):327–330, April 2006.

[124] JM Bland and DJ Altman. Regression analysis. *Lancet*, 1(8486):908–909, April 1986.

[125] RJ Geuns van, T Baks, EH Gronenschild, JP Aben, PA Wielopolski, F Cademartiri, and PJ Feyter de. Automatic quantitative left ventricular analysis of cine MR images by using three-dimensional information for contour detection. *Radiology*, 240(1):215–221, July 2006.

[126] K Wolf-Maier, RS Cooper, JR Banegas, S Giampaoli, HW Hense, M Joffres, M Kastarinen, N Poulter, P Primatesta, F Rodriguez-Artalejo, B Stegmayr, M Thamm, J Tuomilehto, D Vanuzzo, and F Vescio. Hypertension prevalence and blood pressure levels in 6 European countries, Canada, and the United States. *JAMA: The Journal of the American Medical Association*, 289(18):2363–2369, May 2003.

[127] RB Shekelle, AM Ostfeld, and HL Klawans. Hypertension and risk of stroke in an elderly population. *Stroke*, 5(1):71–75, January 1974.

[128] AW Haider, MG Larson, SS Franklin, and D Levy. Systolic blood pressure, diastolic blood pressure, and pulse pressure as predictors of risk for congestive heart failure in the Framingham Heart Study. *Ann Intern Med*, 138(1):10–16, January 2003.

[129] K Svardsudd and G Tibblin. Mortality and morbidity during 13.5 years' follow-up in relation to blood pressure. The study of men born in 1913. *Acta Med Scand*, 205(6):483–92, 1979.

[130] G Heinemann and D Wallrabe. Determinants of left ventricular hypertrophy in arterial hypertension. *Cor Vasa*, 32(1):19–25, 1990.

[131] FT Loop der van, G Schaart, ED Timmer, FC Ramaekers, and GJ Eys van. Smoothelin, a novel cytoskeletal protein specific for smooth muscle cells. *J Cell Biol*, 134(2):401–411, July 1996.

[132] FT Loop der van, G Gabbiani, G Kohnen, FC Ramaekers, and GJ Eys van. Differentiation of smooth muscle cells in human blood vessels as defined by smoothelin, a novel marker for the contractile phenotype. *Arterioscler Thromb Vasc Biol*, 17(4):665–671, April 1997.

[133] JL Johnson, GJ Eys van, GD Angelini, and SJ George. Injury induces dedifferentiation of smooth muscle cells and increased matrix-degrading metalloproteinase activity in human saphenous vein. *Arterioscler Thromb Vasc Biol*, 21(7):1146–1151, July 2001.

[134] T Christen, V Verin, M Bochaton-Piallat, Y Popowski, F Ramaekers, P Debruyne, E Camenzind, G Eys van, and G Gabbiani. Mechanisms of neointima formation and remodeling in the porcine coronary artery. *Circulation*, 103(6):882–888, February 2001.

[135] P Niessen, S Rensen, J Deursen van, J Man De, A Laet De, JM Vanderwinden, T Wedel, D Baker, P Doevendans, M Hofker, M Gijbels, and G Eys van. Smoothelin-a is essential for functional intestinal smooth muscle contractility in mice. *Gastroenterology*, 129(5):1592–1601, November 2005.

[136] HA Rockman, RS Ross, AN Harris, KU Knowlton, ME Steinhelper, LJ Field, J Ross, and KR Chien. Segregation of atrial-specific and inducible expression of an atrial natriuretic factor transgene in an in vivo murine model of cardiac hypertrophy. *Proc Natl Acad Sci U S A*, 88(18):8277–8281, September 1991.

[137] HA Rockman, SP Wachhorst, L Mao, and J Ross. ANG II receptor blockade prevents ventricular hypertrophy and ANF gene expression with pressure overload in mice. *Am J Physiol*, 266(6).

[138] B Ding, RL Price, TK Borg, EO Weinberg, PF Halloran, and BH Lorell. Pressure overload induces severe hypertrophy in mice treated with cyclosporine, an inhibitor of calcineurin. *Circ Res*, 84(6):729–734, April 1999.

[139] K Harada, I Komuro, I Shiojima, D Hayashi, S Kudoh, T Mizuno, K Kijima, H Matsubara, T Sugaya, K Murakami, and Y Yazaki. Pressure overload induces cardiac hypertrophy in angiotensin II type 1A receptor knockout mice. *Circulation*, 97(19):1952–1959, May 1998.

[140] JA Byrne, DJ Grieve, JK Bendall, JM Li, C Gove, JD Lambeth, AC Cave, and AM Shah. Contrasting roles of NADPH oxidase isoforms in pressure-overload versus angiotensin II-induced cardiac hypertrophy. *Circ Res*, 93(9):802–805, October 2003.

[141] JE Wagenseil, NL Nerurkar, RH Knutsen, RJ Okamoto, DY Li, and RP Mecham. Effects of elastin haploinsufficiency on the mechanical behavior of mouse arteries. *Am J Physiol Heart Circ Physiol*, 289(3):H1209–H1217, September 2005.

[142] N Nishijo, S Takamine, F Sugiyama, K Kimoto, K Taniguchi, H Horiguchi, T Ogata, K Murakami, A Fukamizu, and K Yagami. Vascular remodeling in hypertensive transgenic mice. *Exp Anim*, 48(3):203–208, July 1999.

[143] E Heijman, W Graaf de, C Diekmann, A Nauerth, GJ Strijkers, and K Nicolay. Retrospective CINE MRI of the mouse heart. *Proc Intl Soc Mag Reson Med*, 14:–, 2006.

[144] Y Ogawa, H Itoh, and K Nakao. Molecular biology and biochemistry of natriuretic peptide family. *Clin Exp Pharmacol Physiol*, 22(1):49–53, January 1995.

[145] YP Du, DL Parker, WL Davis, and G Cao. Reduction of partial-volume artifacts with zero-filled interpolation in three-dimensional MR angiography. *J Magn Reson Imaging*, 4(5):733–741, September 1994.

[146] DL Parker, YP Du, and WL Davis. The voxel sensitivity function in Fourier transform imaging: applications to magnetic resonance angiography. *Magn Reson Med*, 33(2):156–162, February 1995.

[147] B Janssen, J Debets, P Leenders, and J Smits. Chronic measurement of cardiac output in conscious mice. *Am J Physiol Regul Integr Comp Physiol*, 282(3):R928–R935, March 2002.

[148] BJ Janssen, T Celle De, JJ Debets, AE Brouns, MF Callahan, and TL Smith. Effects of anesthetics on systemic hemodynamics in mice. *Am J Physiol Heart Circ Physiol*, 287(4):H1618–H1624, October 2004.

[149] TD Williams, JB Chambers, RP Henderson, ME Rashotte, and JM Overton. Cardiovascular responses to caloric restriction and thermoneutrality in C57BL/6J mice. *Am J Physiol Regul Integr Comp Physiol*, 282(5):R1459–R1467, May 2002.

[150] R Ross. The pathogenesis of atherosclerosis: a perspective for the 1990s. *Nature*, 362:801–809, April 1993.

[151] K.Glass Christopher and L.Witztum Joseph. Atherosclerosis: The Road Ahead. *Cell*, 104:503–516, February 2001.

[152] A Roos de, P Kunz, H Lamb, L Kroft, S Langerak, J Doornbos, and WE der van. Magnetic resonance imaging of ischemic heart disease: why cardiac magnetic resonance imaging will play a significant role in the management of patients with coronary artery disease. *J Comput Assist Tomogr*, 23:S135–S141, November 1999.

[153] RC Semelka, E Tomei, S Wagner, J Mayo, C Kondo, J Suzuki, GR Caputo, and CB Higgins. Normal left ventricular dimensions and function: interstudy reproducibility of measurements with cine MR imaging. *Radiology*, 174(3):763–768, March 1990.

[154] MS Florentine, CL Grosskreutz, W Chang, JA Hartnett, VD Dunn, JC Ehrhardt, SR Fleagle, SM Collins, ML Marcus, and DJ Skorton. Measurement of left ventricular mass in vivo using gated nuclear magnetic resonance imaging. *J Am Coll Cardiol*, 8(1):107–112, July 1986.

[155] RJ Geest der van and JH Reiber. Quantification in cardiac MRI. *J Magn Reson Imaging*, 10(5):602–608, November 1999.

[156] RC Semelka, E Tomei, S Wagner, J Mayo, G Caputo, M O'Sullivan, WW Parmley, K Chatterjee, C Wolfe, and CB Higgins. Interstudy reproducibility of dimensional and functional measurements between cine magnetic resonance studies in the morphologically abnormal left ventricle. *Am Heart J*, 119(6):1367–1373, June 1990.

[157] SB Reeder, AA Holmes, ER McVeigh, and JR Forder. Simultaneous noninvasive determination of regional myocardial perfusion and oxygen content in rabbits: Toward direct measurement of myocardial oxygen consumption at MR imaging. *Radiology*, 212(3):739–747, September 1999.

[158] LJ Kroft and A Roos de. Blood pool contrast agents for cardiovascular MR imaging. *J Magn Reson Imaging*, 10(3):395–403, September 1999.

[159] E Castillo, JA Lima, and DA Bluemke. Regional myocardial function: advances in MR imaging and analysis. *Radiographics*, 23:S127–S140, October 2003.

[160] E Omerovic, M Basetti, E Bollano, M Bohlooly, J Tornell, J Isgaard, A Hjalmarson, B Soussi, and F Waagstein. In vivo metabolic imaging of cardiac bioenergetics in transgenic mice. *Biochem Biophys Res Commun*, 271(1):222–228, April 2000.

[161] S Schaefer and RS Balaban. *Cardiovascular magnetic resonance spectroscopy.*

[162] F Wiesmann, M Szimtenings, A Frydrychowicz, R Illinger, A Hunecke, E Rommel, S Neubauer, and A Haase. High-resolution MRI with cardiac and respiratory gating

allows for accurate in vivo atherosclerotic plaque visualization in the murine aortic arch. *Magn Reson Med*, 50(1):69–74, July 2003.

[163] RP Choudhury, JG Aguinaldo, JX Rong, JL Kulak, AR Kulak, ED Reis, JT Fallon, V Fuster, EA Fisher, and ZA Fayad. Atherosclerotic lesions in genetically modified mice quantified in vivo by non-invasive high-resolution magnetic resonance microscopy. *Atherosclerosis*, 162(2):315–321, June 2002.

[164] RP Choudhury, ZA Fayad, JG Aguinaldo, VV Itskovich, JX Rong, JT Fallon, and EA Fisher. Serial, noninvasive, in vivo magnetic resonance microscopy detects the development of atherosclerosis in apolipoprotein E-deficient mice and its progression by arterial wall remodeling. *J Magn Reson Imaging*, 17(2):184–189, February 2003.

[165] ZA Fayad, JT Fallon, M Shinnar, S Wehrli, HM Dansky, M Poon, JJ Badimon, SA Charlton, EA Fisher, JL Breslow, and V Fuster. Noninvasive In vivo high-resolution magnetic resonance imaging of atherosclerotic lesions in genetically engineered mice. *Circulation*, 98(15):1541–1547, October 1998.

[166] VV Itskovich, RP Choudhury, JG Aguinaldo, JT Fallon, S Omerhodzic, EA Fisher, and ZA Fayad. Characterization of aortic root atherosclerosis in ApoE knockout mice: high-resolution in vivo and ex vivo MRM with histological correlation. *Magn Reson Med*, 49(2):381–385, February 2003.

[167] M Nahrendorf, F Wiesmann, KH Hiller, K Hu, C Waller, J Ruff, TE Lanz, S Neubauer, A Haase, G Ertl, and WR Bauer. Serial cine-magnetic resonance imaging of left ventricular remodeling after myocardial infarction in rats. *J Magn Reson Imaging*, 14(5):547–555, November 2001.

[168] M Nahrendorf, KH Hiller, K Hu, G Ertl, A Haase, and WR Bauer. Cardiac magnetic resonance imaging in small animal models of human heart failure. *Med Image Anal*, 7(3):369–375, September 2003.

[169] C Waller, KH Hiller, E Kahler, K Hu, M Nahrendorf, S Voll, A Haase, G Ertl, and WR Bauer. Serial magnetic resonance imaging of microvascular remodeling in the infarcted rat heart. *Circulation*, 103(11):1564–1569, March 2001.

[170] MM Markl, FP Chan, MT Alley, KL Wedding, MT Draney, CJ Elkins, DW Parker, R Wicker, CA Taylor, RJ Herfkens, and NJ Pelc. Time resolved three-dimensional phase-contrast MRI. *J Magn Reson Imaging*, 17:499–506, 2003.

[171] KL Wedding, MT Draney, RJ Herfkens, CK Zarins, CA Taylor, and NJ Pelc. Measurement of vessel wall strain using cine phase contrast MRI. *J Magn Reson Imaging*, 15:418–428, 2002.

[172] AE Arai, CC Gaither, FH Epstein, RS Balaban, SD Wolff, and al. et. Myocardial velocity gradient imaging by phase contrast MRI with application to regional function in myocardial ischemia. *Magn Reson Med*, 42:98–109, 1999.

[173] S Ryf, MA Spiegel, M Gerber, and P Boesiger. Myocardial tagging with 3D-SPAMM. *J Magn Reson*, 16:320–325, 2002.

[174] JPA Kuijer, E Jansen, JT Marcus, AC Rossum van, and RM Heethaar. Improved harmonic phase myocardial strain maps. *Magn Reson Med*, 46(5):993–999, November 2001.

[175] E Lutgens, MJ Daemen, ED Muinck de, J Debets, P Leenders, and JF Smits. Chronic myocardial infarction in the mouse: cardiac structural and functional changes. *Cardiovasc Res*, 41(3):586–593, 1999.

[176] SE Fischer, GC McKinnon, SE Maier, and P Boesiger. Improved myocardial tagging contrast. *Magn Reson Med*, 30:191–200, 1993.

[177] NF Osman, WS Kerwin, ER McVeigh, and JL Prince. Cardiac motion tracking using CINE harmonic phase (HARP) magnetic resonance imaging ,. *Magn Reson Med*, 42:1048–1060, 1999.

[178] FM Haacke, RW Brown, MR Thompson, and R Venkatesan. *Magnetic Resonance Imaging : Physical principles and sequence design*.

[179] E Atalar and ER McVeigh. Optimization of tag thickness for measuring position with magnetic resonance imaging. *IEEE Trans Med Im*, 13(1):152–160, March 1994.

[180] JP Kuijer, MB Hofman, JJ Zwanenburg, JT Marcus, AC Rossum van, and RM Heethaar. DENSE and HARP: two views on the same technique of phase-based strain imaging. *J Magn Reson Imaging*, 24(6):1432–1438, December 2006.

[181] M Nieminen and J Heikkila. Echoventriculography in acute myocardial infarction. III. Clinical correlations and implication of the noninfarcted myocardium. *Am J Cardiol*, 38(1):1–8, July 1976.

[182] M Rigaud, P Rocha, J Boschat, JC Farcot, J Bardet, and JP Bourdarias. Regional left ventricular function assessed by contrast angiography in acute myocardial infarction. *Circulation*, 60(1):130–139, July 1979.

[183] WY Lew, ZY Chen, B Guth, and JW Covell. Mechanisms of augmented segment shortening in nonischemic areas during acute ischemia of the canine left ventricle. *Circ Res*, 56(3):351–358, March 1985.

[184] EJ Somer, NA Benatar, MJ O'Doherty, MA Smith, and PK Marsden. Use of the CT component of PET-CT to improve PET-MR registration: demonstration in soft-tissue sarcoma. *Phys Med Biol*, 52(23):6991–7006, December 2007.

[185] D Utsunomiya, S Tomiguchi, S Shiraishi, K Yamada, T Honda, K Kawanaka, A Kojima, K Awai, and Y Yamashita. Initial experience with X-ray CT based attenuation correction in myocardial perfusion SPECT imaging using a combined SPECT/CT system. *Ann Nucl Med*, 19(6):485–489, September 2005.

[186] H Liang, Y Yang, K Yang, Y Wu, JM Boone, and SR Cherry. A microPET/CT system for in vivo small animal imaging. *Phys Med Biol*, 52(13):3881–3894, July 2007.

[187] S Sharma and M Ebadi. SPECT neuroimaging in translational research of CNS disorders. *Neurochem Int*, 52(3):352–362, February 2008.

[188] C Goetz, E Breton, P Choquet, V Israel-Jost, and A Constantinesco. SPECT low-field MRI system for small-animal imaging. *J Nucl Med*, 49(1):88–93, January 2008.

[189] PK Marsden, D Strul, SF Keevil, SC Williams, and D Cash. Simultaneous PET and NMR. *Br J Radiol*, 75.

[190] M Nahrendorf, C Badea, LW Hedlund, JL Figueiredo, DE Sosnovik, GA Johnson, and R Weissleder. High-resolution imaging of murine myocardial infarction with delayed-enhancement cine micro-CT. *Am J Physiol Heart Circ Physiol*, 292(6):H3172–H3178, June 2007.

[191] M Drangova, NL Ford, SA Detombe, AR Wheatley, and DW Holdsworth. Fast retrospectively gated quantitative four-dimensional (4D) cardiac micro computed tomography imaging of free-breathing mice. *Invest Radiol*, 42(2):85–94, February 2007.

[192] C Badea, LW Hedlund, and GA Johnson. Micro-CT with respiratory and cardiac gating. *Med Phys*, 31(12):3324–3329, December 2004.

[193] D Dawson, CA Lygate, J Saunders, JE Schneider, X Ye, K Hulbert, JA Noble, and S Neubauer. Quantitative 3-dimensional echocardiography for accurate and rapid cardiac phenotype characterization in mice. *Circulation*, 110(12):1632–1637, September 2004.

[194] R Zhou, S Pickup, TE Yankeelov, CS Springer, and JD Glickson. Simultaneous measurement of arterial input function and tumor pharmacokinetics in mice by dynamic contrast enhanced imaging: effects of transcytolemmal water exchange. *Magn Reson Med*, 52(2):248–257, August 2004.

[195] Y Li, CD Garson, Y Xu, RJ Beyers, FH Epstein, BA French, and JA Hossack. Quantification and MRI validation of regional contractile dysfunction in mice post myocardial infarction using high resolution ultrasound. *Ultrasound Med Biol*, 33(6):894–904, June 2007.

[196] KP Schafers, L Stegger, C Barnard, M Kriens, S Hermann, O Schober, and M Schafers. ECG-triggered high-resolution positron emission tomography: a breakthrough in cardiac molecular imaging of mice. *Eur J Nucl Med Mol Imaging*, 32(3):383–, March 2005.

[197] BB Chin, SD Metzler, A Lemaire, A Curcio, S Vemulapalli, KL Greer, NA Petry, TG Turkington, RE Coleman, H Rockman, and RJ Jaszczak. Left ventricular functional assessment in mice: feasibility of high spatial and temporal resolution ECG-gated blood pool SPECT. *Radiology*, 245(2):440–448, November 2007.

[198] KM Shioura, DL Geenen, and PH Goldspink. Assessment of cardiac function with the pressure-volume conductance system following myocardial infarction in mice. *Am J Physiol Heart Circ Physiol*, 293(5):H2870–H2877, November 2007.

[199] JM Nielsen, SB Kristiansen, S Ringgaard, TT Nielsen, A Flyvbjerg, AN Redington, and HE Botker. Left ventricular volume measurement in mice by conductance catheter: evaluation and optimization of calibration. *Am J Physiol Heart Circ Physiol*, 293(1):H534–H540, July 2007.

[200] JM Nielsen, AN Redington, and SB Kristiansen. Commentary on 'Direct comparison of magnetic resonance imaging and conductance microcatheter in the evaluation of left ventricular function in mice' by Jacoby *et al.*. *Basic Research in Cardiology*, (1):96–97, January 2006.

[201] K Rajappan, L Livieratos, PG Camici, and DJ Pennell. Measurement of ventricular volumes and function: a comparison of gated PET and cardiovascular magnetic resonance. *J Nucl Med*, 43(6):806–810, June 2002.

[202] RH Slart, JJ Bax, RM Jong de, J Boer de, HJ Lamb, PH Mook, AT Willemsen, W Vaalburg, DJ Veldhuisen van, and PL Jager. Comparison of gated PET with MRI for evaluation of left ventricular function in patients with coronary artery disease. *J Nucl Med*, 45(2):176–182, February 2004.

[203] D Thomas, H Bal, J Arkles, J Horowitz, L Araujo, PD Acton, and VA Ferrari. Noninvasive assessment of myocardial viability in a small animal model: Comparison of MRI, SPECT, and PET. *Magn Reson Med*, 59(2):252–259, January 2008.

[204] TR Miller, JW Wallis, BR Landy, RJ Gropler, and CL Sabharwal. Measurement of global and regional left ventricular function by cardiac PET. *J Nucl Med*, 35(6):999–1005, June 1994.

[205] E Heijman, W Graaf de, P Niessen, A Nauerth, G Eys van, L Graaf de, K Nicolay, and GJ Strijkers. Comparison between prospective and retrospective triggering for mouse cardiac MRI. *NMR Biomed*, 20(4):439–447, June 2007.

[206] AP Jeavons, AP Jeavons, RA Chandler, and CAR Dettmar. A 3D HIDAC-PET camera with sub-millimetre resolution for imaging small animals. *Nuclear Science, IEEE Transactions on*, 46(3):468–473, 1999.

[207] KP Schafers, N Lang, L Stegger, O Schober, and M Schafers. Gated listmode acquisition with the quadHIDAC animal PET to image mouse hearts. *Z Med Phys*, 16(1):60–66, 2006.

[208] AJ Reader, S Ally, F Bakatselos, R Manavaki, RJ Walledge, AP Jeavons, PJ Julyan, S Zhao, DL Hastings, and J Zweit. One-Pass List-Mode EM Algorithm for High-Resolution 3-D PET Image Reconstruction Into Large Arrays. *IEEE TRANSACTIONS ON NUCLEAR SCIENCE*, 49(3):693–, 2002.

[209] E Heijman, JP Aben, C Penners, P Niessen, R Guillaume, G Eys van, K Nicolay, and GJ Strijkers. Evaluation of manual and automatic segmentation of the mouse heart from CINE MR images. *J Magn Reson Imaging*, 27(1):86–93, January 2008.

[210] L Stegger, S Biedenstein, KP Schafers, O Schober, and MA Schafers. Elastic surface contour detection for the measurement of ejection fraction in myocardial perfusion SPET. *Eur J Nucl Med*, 28(1):48–55, January 2001.

[211] L Stegger, AN Hoffmeier, KP Schafers, S Hermann, O Schober, MA Schafers, and G Theilmeier. Accurate Noninvasive Measurement of Infarct Size in Mice with High-Resolution PET. *J Nucl Med*, 47(11):1837–1844, November 2006.

[212] M Hove ten, CA Lygate, A Fischer, JE Schneider, AE Sang, K Hulbert, L Sebag-Montefiore, H Watkins, K Clarke, D Isbrandt, J Wallis, and S Neubauer. Reduced inotropic reserve and increased susceptibility to cardiac ischemia/reperfusion injury in phosphocreatine-deficient guanidinoacetate-N-methyltransferase-knockout mice. *Circulation*, 111(19):2477–2485, May 2005.

[213] MC Kreissl, HM Wu, DB Stout, W Ladno, TH Schindler, X Zhang, JO Prior, ML Prins, AF Chatziioannou, SC Huang, and HR Schelbert. Noninvasive Measurement of Cardiovascular Function in Mice with High-Temporal-Resolution Small-Animal PET. *J Nucl Med*, 47(6):974–980, June 2006.

[214] Y Yang, S Rendig, S Siegel, DF Newport, and SR Cherry. Cardiac PET imaging in mice with simultaneous cardiac and respiratory gating. *Phys Med Biol*, 50(13):2979–2989, July 2005.

[215] MD Cerqueira, NJ Weissman, V Dilsizian, AK Jacobs, S Kaul, WK Laskey, DJ Pennell, JA Rumberger, T Ryan, and MS Verani. Standardized myocardial segmentation and nomenclature for tomographic imaging of the heart: a statement for healthcare professionals from the Cardiac Imaging Committee of the Council on Clinical Cardiology of the American Heart Association. *Circulation*, 105(4):539–542, January 2002.

[216] C Klein, SG Nekolla, FM Bengel, M Momose, A Sammer, F Haas, B Schnackenburg, W Delius, H Mudra, D Wolfram, and M Schwaiger. Assessment of myocardial viability with contrast-enhanced magnetic resonance imaging: comparison with positron emission tomography. *Circulation*, 105(2):162–167, January 2002.

[217] H Zhuang, M Pourdehnad, ES Lambright, AJ Yamamoto, M Lanuti, P Li, PD Mozley, MD Rossman, SM Albelda, and A Alavi. Dual time point 18F-FDG PET imaging for differentiating malignant from inflammatory processes. *J Nucl Med*, 42(9):1412–1417, September 2001.

[218] WJ Manning, DJ Atkinson, W Grossman, S Paulin, and RR Edelman. First-pass nuclear magnetic resonance imaging studies using gadolinium-DTPA in patients with coronary artery disease. *J Am Coll Cardiol*, 18(4):959–965, October 1991.

[219] MH Mendonca Dias and PC Lauterbur. Ferromagnetic particles as contrast agents for magnetic resonance imaging of liver and spleen. *Magn Reson Med*, 3(2):328–330, April 1986.

[220] PF Renshaw, CS Owen, AC McLaughlin, TG Frey, and JS Leigh. Ferromagnetic contrast agents: a new approach. *Magn Reson Med*, 3(2):217–225, April 1986.

[221] JW Bulte and DL Kraitchman. Iron oxide MR contrast agents for molecular and cellular imaging. *NMR Biomed*, 17(7):484–499, November 2004.

[222] WJ Mulder, K Douma, GA Koning, MA Zandvoort van, E Lutgens, MJ Daemen, K Nicolay, and GJ Strijkers. Liposome-enhanced MRI of neointimal lesions in the ApoE-KO mouse. *Magn Reson Med*, 55(5):1170–1174, May 2006.

[223] DA Sipkins, DA Cheresh, MR Kazemi, LM Nevin, MD Bednarski, and KC Li. Detection of tumor angiogenesis in vivo by alphaVbeta3-targeted magnetic resonance imaging. *Nat Med*, 4(5):623–626, May 1998.

[224] KN Raymond and VC Pierre. Next generation, high relaxivity gadolinium MRI agents. *Bioconjug Chem*, 16(1):3–8, January 2005.

[225] HY Carr. Steady-State Free Precession in Nuclear Magnetic Resonance. *Phys Rev*, 112:1693–1701, January 1958.

[226] WA Hinshaw. Spin mapping: the application of moving gradients to NMR. *Physics Letters*, 48:87–88, 1974.

[227] WA Hinshaw. Image formation by nuclear magnetic resonance: the sensitive point method. *Journal of Applied Physics*, 47:3709–3721, 1976.

[228] A Oppelt, R Graumann, H Barfuss, H Fisher, W Hartl, and W Schajor. FISP: eine neue schnelle pulssequenz fr die kernspintomografie. *Electromedica*, 54:15–18, 1986.

[229] Y Zur, S Stokar, and P Bendel. An analysis of fast imaging sequences with steady-state transverse magnetization refocusing. *Magn Reson Med*, 6(2):175–193, February 1988.

[230] RC Hawkes and S Patz. Rapid Fourier imaging using steady-state free precession. *Magn Reson Med*, 4(1):9–23, January 1987.

[231] EM Haacke, PA Wielopolski, JA Tkach, and MT Modic. Steady-state free precession imaging in the presence of motion: application for improved visualization of the cerebrospinal fluid. *Radiology*, 175(2):545–552, May 1990.

[232] Y Zur, ML Wood, and LJ Neuringer. Motion-insensitive, steady-state free precession imaging. *Magn Reson Med*, 16(3):444–459, December 1990.

[233] JL Duerk, JS Lewin, M Wendt, and C Petersilge. Remember true FISP? A high SNR, near 1-second imaging method for T2-like contrast in interventional MRI at .2 T. *J Magn Reson Imaging*, 8(1):203–208, January 1998.

[234] VS Deshpande, SM Shea, G Laub, OP Simonetti, JP Finn, and D Li. 3D magnetization-prepared true-FISP: a new technique for imaging coronary arteries. *Magn Reson Med*, 46(3):494–502, September 2001.

[235] M Deimling and O Heid. Magnetization prepared true FISP imaging. *In: Proceedings of the 2nd annual meeting of the ISMRM, San Francisco.*

[236] K Scheffler, O Heid, and J Hennig. Magnetization preparation during the steady state: fat-saturated 3D TrueFISP. *Magn Reson Med*, 45(6):1075–1080, June 2001.

[237] WG Schreiber, M Schmitt, P Kalden, OK Mohrs, KF Kreitner, and M Thelen. Dynamic contrast-enhanced myocardial perfusion imaging using saturation-prepared TrueFISP. *J Magn Reson Imaging*, 16(6):641–652, December 2002.

[238] RL Perrin, MK Ivancevic, S Kozerke, and JP Vallee. Comparative study of FAST gradient echo MRI sequences: phantom study. *J Magn Reson Imaging*, 20(6):1030–1038, December 2004.

[239] BA Hargreaves, SS Vasanawala, JM Pauly, and DG Nishimura. Characterization and reduction of the transient response in steady-state MR imaging. *Magn Reson Med*, 46(1):149–158, July 2001.

[240] F Bloch. Nuclear induction. *Phys Rev*, 70(7):460–473, 1946.

[241] CJ Yeung, RC Susil, and E Atalar. RF safety of wires in interventional MRI: using a safety index. *Magn Reson Med*, 47(1):187–193, January 2002.

[242] M Barth and E Moser. Proton NMR relaxation times of human blood samples at 1.5 T and implications for functional MRI. *Cell Mol Biol (Noisy -le-grand)*, 43(5):783–791, July 1997.

[243] O Bieri and K Scheffler. On the origin of apparent low tissue signals in balanced SSFP. *Magn Reson Med*, 56(5):1067–1074, November 2006.

[244] SD Thomas, O Kwifi Al, DJ Emery, and AH Wilman. Application of magnetization transfer at 3.0 T in three-dimensional time-of-flight magnetic resonance angiography of the intracranial arteries. *J Magn Reson Imaging*, 15(4):479–483, April 2002.

[245] HY Lin, BM Dale, CA Flask, and JL Duerk. Blood attenuation with SSFP-compatible saturation (BASS). *J Magn Reson Imaging*, 24(3):701–707, September 2006.

[246] MG Danilouchkine, JJ Westenberg, BP Lelieveldt, and JH Reiber. Accuracy of short-axis cardiac MRI automatically derived from scout acquisitions in free-breathing and breath-holding modes. *MAGMA*, 18(1):7–18, March 2005.

Appendix: Planning of mouse cardiac MR images

The mouse heart is different in its geometry than the human heart. The largest difference is that the right ventricle of the mouse heart is positioned at the upper part of the left ventricle (see Figure A.1). In the human heart the right and left ventricles are almost positioned at the same height between base and apex. Also the shapes of the mouse heart atria are different compared to a human heart. For the mouse the atria seem not to be part of the heart. The atria have the shape of bags which are positioned on top of both ventricles.

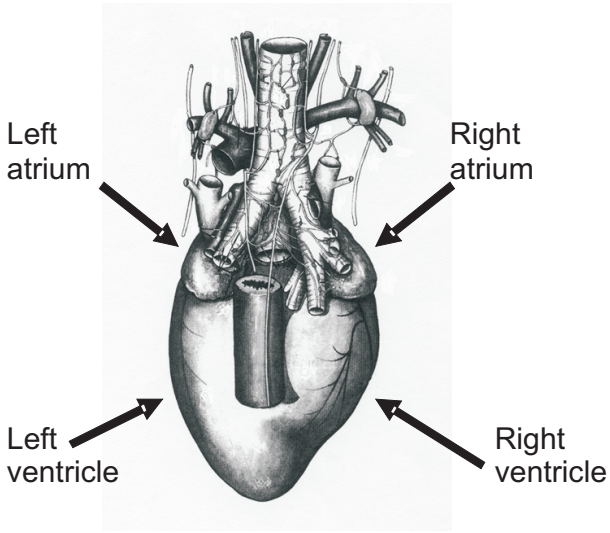

Figure A.1: Schematic drawing of the posterior view of a mouse heart, arteries, veins and the lower part of the trachea.

The human procedure for finding the different chamber views cannot be directly applied to the mouse heart because of the above mentioned differences in geometry. The planning of the long-axis of a mouse heart is visualized in Figure A.2. From this long-axis the short-axis as well as other long-axis orientations can be found easily. All MR images in Figure A.2 are part of a CINE protocol acquisition to find the end-diastolic and end-

systolic heart phases and identify the aorta. The planning of the different planes is always done on the basis of the image collected at the end-diastolic heart phase. Sometimes the orientations of the different planes are checked within the systolic period. Figure A.2 is split into two parts: in the left column the different views of the mouse heart are shown in the two columns at the right the corresponding plane was cut in a strawberry which represents the left ventricle of the mouse heart. In the first row we see at the left hand side the short-axis view of the mouse heart around the equator (SA), the goal of this planning procedure, and at the right two different views of the strawberry (A1,A2). The planning procedure starts with a transversal slice (TR) through the heart. A plane is selected perpendicular to the transversal plane dissecting both the end-points of the septum (TR: dotted yellow line). To find the next view this plane is shifted towards the aorta (TR: red line). This view is called the apparent long-axis view (AL). To find the long-axis view, a perpendicular plane is planned through the lowest point in the apical side of the heart and the highest point in the basal part of the heart (AL: red line). The first long-axis view is now found (LA). It can be seen from the strawberry (D1) that this orientation is the true long-axis view. One can now decide to image a second long-axis view (LA: dotted yellow line) or plan the short-axis view (SA) perpendicularly to both long-axis planes (LA: red line). It can be seen that the second long-axis orientation is not dissecting the apical point of the mouse heart (LA), but is placed symmetrically between both heart walls.

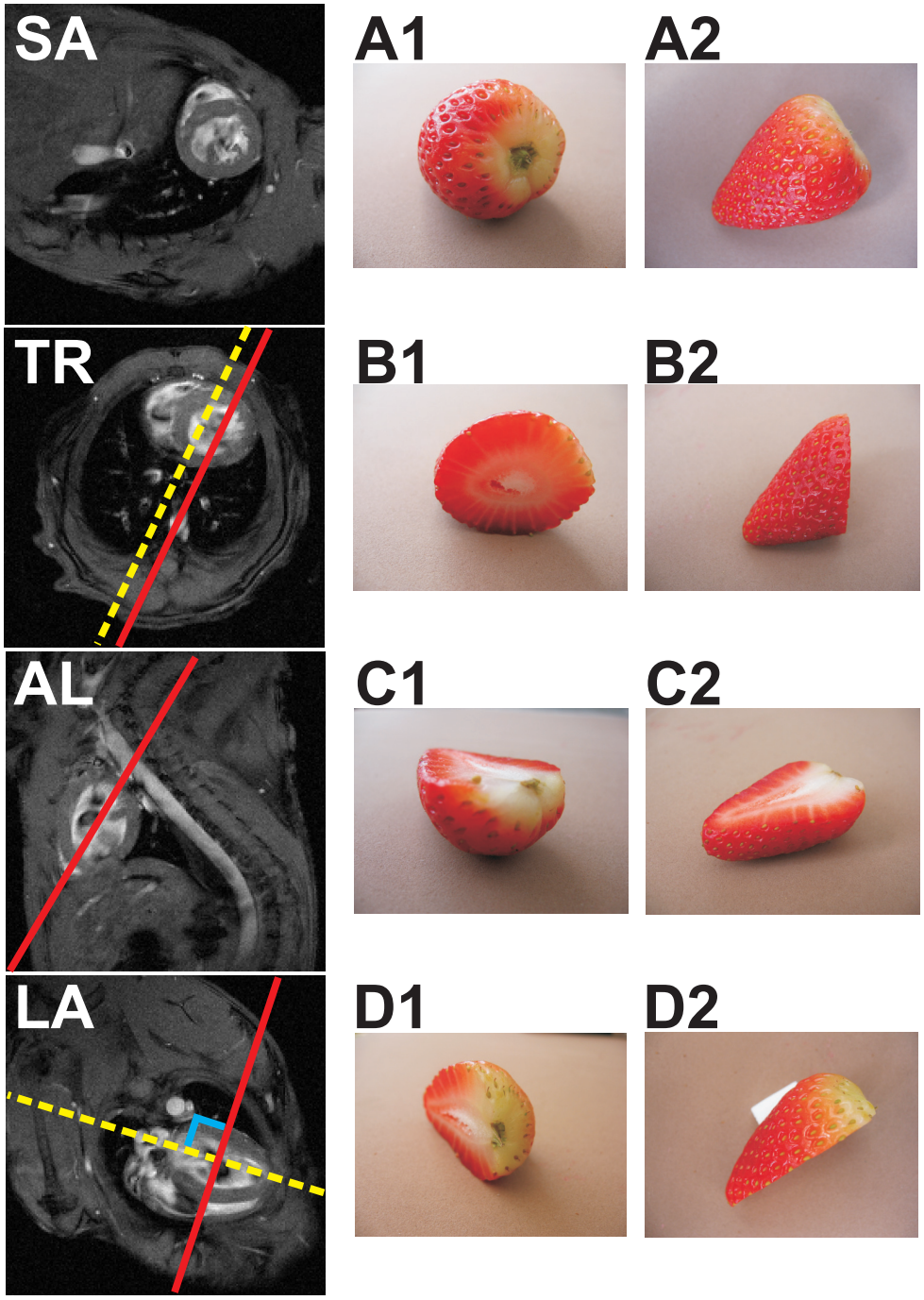

Figure A.2: Visualization of planning the different heart views during a mouse cardiac MRI experiment. At the left the different heart views are shown: short-axis (SA); transversal (TR); apparent long-axis (AL); long-axis (LA). In the right column, the different heart views are visualized by different dissections of a strawberry (A1 to D2). For further explanation see text.

Samenvatting

De laatste decennia is de interesse in het afbeelden van het hart in de levende muis enorm toegenomen. Deze interesse wordt voor een groot gedeelte gedragen door nieuwe ontwikkelingen in de gentechnologie en moleculaire biologie. Doel van het promotieonderzoek was een toolbox te ontwikkelen van verschillende MRI- (Magnetische Resonantie Imaging) en analysetechnieken, als ondersteuning van het huidige en toekomstige onderzoek op het gebied van muizenharten.
Het is met een MRI scanner moeilijk het muizenhart goed af te beelden vanwege de geringe afmetingen van het muizenhart en de hoge frequentie waarmee het muizenhart klopt. Om een goede afbeelding van het muizenhart te krijgen is het noodzakelijk gebruik te maken van een opstelling welke zorgt dat de verschillende fysiologische parameters van de muizen gemeten en gecontroleerd kunnen worden gedurende de acquisitie. Verder worden grote bewegingsfouten voorkomen door de acquisitie van het tomografische beeld te synchroniseren met de cyclische beweging van het hart. Deze synchronisatie wordt normaal gerealiseerd door het begin van de hartcyclus te bepalen aan de hand van een elektrocardiogram en te bepalen wanneer de muis geen ademhalingsbeweging uitvoert. In dit proefschrift wordt een 'draadloze' techniek beschreven waarbij het meten van de fase van de hartcyclus en de ademhalingscyclus bepaald wordt vanuit het magnetische resonantiesignaal zelf. Het asynchroon uitvoeren van de acquisitie, en deze na afloop van de meting te synchroniseren met de hartslag, heeft als bijkomend voordeel dat de sterkte van het magnetische resonantiesignaal hetzelfde blijft gedurende de volledige acquisitie. Dit zorgt ervoor dat contrastverschillen in het tomografische beeld gelijk blijven en niet afhankelijk zijn van de conditie van de muis. De constante signaalsterkte gaat ten koste van een lagere signaal-ruis-verhouding. De verlaging van de signaal-ruis-verhouding heeft er toe geleid dat de volumes van het werkende muizenhart enigszins verschillend werden beoordeeld.
MRI is niet alleen in staat om tomografische afbeeldingen te maken, maar kan ook fysiologische parameters te kwantificeren. Het grote nadeel van een tomografische afbeeldingtechniek is dat het alleen kwalitatieve informatie geeft, zoals de morfologie. Kwantitatieve informatie ,bijvoorbeeld een volumebepaling, kan alleen verkregen worden door het segmenteren van het muizenhart uit de verkregen tomografische afbeelding. Het seg-

menteren kost enorm veel tijd wanneer dit met de hand moet worden uitgevoerd. Bovendien kan handmatige segmentatie onnauwkeurig worden als het niet door gekwalificeerde personen wordt uitgevoerd. We laten in dit proefschrift zien dat een automatische segmentatie methode een even grote fout maakt als de fout die gemaakt wordt wanneer twee verschillende gekwalificeerde personen dezelfde segmentaties met de hand uitvoeren binnen een muizengroep.
De synchronisatietechniek zoals hierboven beschreven, gebaseerd op het magnetische resonantiesignaal, werd ook toegepast om de volledige bewegingscyclus van de aorta af te beelden in twee verschillende muisgenotypes (Smtn-$B^{+/+}$ and Smtn-$B^{-/-}$). Het genotype Smtn-$B^{-/-}$ heeft een afwijkende contractiekracht in de arteriën en een hogere gemiddelde arteriële bloeddruk. De aortadiametertoename in het genotype Smtn-$B^{-/-}$ was tweemaal groter gedurende de hartcyclus in vergelijking met muizen van het genotype Smtn-$B^{+/+}$. Verder hadden de muizenharten van de Smtn-$B^{-/-}$ genotype een grotere linkerventrikelmassa en een hogere ejectiefractie. Deze studie, waarin twee verschillende muizengroepen met elkaar werden vergeleken, laat zien dat de MRI-techniek zeer kleine verschillen in fysiologische parameters van het muizenhart kan detecteren.
MRI wordt naast phenotypering ook gebruikt om muizenharten met een infarct te karakteriseren. Verschillende publicaties vergelijken fysiologische parameters van muizenharten met infarcten gemeten tussen MRI enerzijds en anderzijds: computertomografie-, echocardiografie- of druk-volumemeting met een katheter. Nieuwe ontwikkelingen op het gebied van nucleaire scantechnieken ,zoals bijvoorbeeld positron emissie tomografie (PET), maken het mogelijk dat deze nucleaire technieken ook muizenharten kunnen karakteriseren. Het grote voordeel van deze nucleaire scantechnieken is hun hoge gevoeligheid voor radioactieve contrastmiddelen, die ervoor zorgt dat men bijna geen toxicologische reacties hoeft te verwachten. In een gecombineerd experiment werden fysiologische parameters vergeleken tussen MRI- en PET-metingen. Ook werd een vergelijking gemaakt tussen de infarctgroottes zoals bepaald met behulp van een MRI-contrastmiddel en een PET-contrastmiddel. Er werd een goede correlatie gevonden tussen beide imagingtechnieken m.b.t. de fysiologische parameters: einddiastole volume, eindsystole volume en ejectiefractie. Aanzienlijke verschillen werden gemeten in de infarctgrootte bepaald uit de MRI- en PET-beelden. Verder werden er hoge correlaties gevonden in de MRI-data tussen drie verschillende infarctgroottebepalingen en de ejectiefracties.
Het afbeelden van ziekteprocessen op het cellulaire en moleculaire niveau met MRI is mogelijk door gebruik te maken van krachtige en specifieke contrastmiddelen. MRI heeft een relatief lage detectiegevoeligheid voor contrastmiddelen. Om de gevoeligheid te vergroten, werd er een studie uitgevoerd naar een snelle MRI-sequentie, bekend onder de naam 'Rephased-FFE'. Deze sequentie liet een 6-maal hogere detectiegevoeligheid zien voor het contrastmiddel Gd-DTPA in een fantoomexperiment met een conventionele humane 1.5 Tesla MRI-scanner.

Dankwoord

Een groot nadeel van het schrijven van een dankwoord in het proefschrift is dat er gemakkelijk iemand vergeten kan worden. In dit dankwoord wil ik niettemin iedereen bedanken die een bijdrage geleverd heeft aan dit proefschrift, maar mijn excuses voor het feit als u niet bij naam genoemd wordt.
Als eerste zou ik de groepsleden van de groepen "Biomedical NMR" (faculteit Biomedische Technologie) en "Transport in Permeable Media" - (faculteit Technische Natuurkunde) willen bedanken voor de prettige sfeer en samenwerking in al die jaren. Vooral in het begin heb ik meerdere malen gebruik gemaakt van de expertise en apparatuur van de natuurkundegroep. Dit heb ik zeer gewaardeerd. Ook zou ik de faculteit BMT willen bedanken voor het creëren van de AIO-positie.
Het is verder onmogelijk om een onderzoek uit te voeren met een lege maag. De MRL-catering heeft er dan ook voor gezorgd dat de lange meetdagen enigszins verzacht werden met kebabbroodjes, worstenbroodjes, cola en snoepgoed. Daarom lof voor de mensen die de MRL-catering levend hebben gehouden: Larry, Laurens, Bart, Ward en Gijs bedankt. Ook mijn "roomies" Hans, Bart en in halve mate Geralda (transfereerde na enige tijd naar beneden), wil ik graag bedanken voor de gezellige sfeer. Hans vertroetelde de planten en zorgde ervoor dat we nauwkeurig bleven werken in het lab. Ik hoop dat Hans verder veel plezier zal hebben en de mogelijkheden weet te waarderen van de moderne software in de toekomst. De discussies met Bart op het gebied van MR fysica heb ik erg gewaardeerd. Ook de tripjes samen met Bart naar de Makro, voor het vullen van de MRL-catering koelkast, waren een mengeling van discussies en calculaties die ik zeer leuk heb gevonden.
Dit proefschrift zou niet tot stand zijn gekomen zonder de steun van studenten die hun stage- of afstudeerperiode deden in onze groep. Zij hebben vooral het voorwerk gedaan of zorgden voor reflectie. De stagiairs Renske, Wouter en Bert heb ik met plezier begeleid. Hun bijdragen hebben geresulteerd in een artikel en in een bijdrage aan een Europees congres. Het harde en goede werk van Jannie en Bram is helaas niet terug te vinden in mijn proefschrift. Echter, beide hebben een enorme inzet en talent getoond. Ik ben dan ook zeer blij, dat ze ingestemd hebben om mij tijdens de verdediging te ondersteunen als paranimf.
Het zijn niet alleen de beide vakgroepen waar ik veel aan te danken heb. Ik wil ook

de mogelijkheden noemen, die geboden werden door de mensen van de werkplaats en de bewaking die in het begin wat sceptisch waren. Later werden ze enthousiaster over het onderzoek dat wij deden als BMT-groep in het gebouw N-laag. Vooral de werkplaatscursus die Marius organiseerde was zeer geslaagd en heeft er toe bijgedragen dat er een goede meetopstelling voor mijn onderzoek gemaakt kon worden. De mensen van de werkplaats stonden altijd klaar om vragen te beantwoorden of van dienst te zijn als ik weer eens een beitel nodig had voor de draaibank. Ook Larry wil ik bedanken voor de goede zorg rondom de scanner. Het duurde soms even maar het loonde zich om geduld te hebben want het was altijd afgewerkt en zelfs 'sjiek'.
Verder ook wil ik Jo bedanken voor mijn introductie in de wereld van de proefdierkunde, en ik hoop dat de frustraties die jij en ik hadden tijdens het ontwikkelen van het muizenmodel een beetje naar de achtergrond zijn geraakt. Ik wil je bedanken dat je het voor mij mogelijk hebt gemaakt om vroegtijdig muizen te scannen. En natuurlijk voor de vele uren die we doorgebracht hebben in het lab van Ben op de Universiteit Maastricht.
Om een goede start te maken was de steun onmisbaar van de groep Farmacologie en Toxicologie van de Universiteit Maastricht. Via Mathijs, Ben, Agnieszka, Sjaak en Peter heb ik alles geleerd op het gebied van muizen en muizenharten. Zeker de mogelijkheid die Ben ons bood om regelmatig gebruik te maken van het lab en de privécolleges van Mathijs op het gebied van histologie heb ik zeer fijn gevonden. Ik wil dan ook alle groepsleden via deze weg bedanken voor jullie tijd en de bereidheid om ons iedere keer te helpen wanneer we weer helemaal waren vastgelopen of geen uitweg meer zagen. Super bedankt.
"Eens kwamen er twee heren bij prof. Kopinga": daarmee begon een lange en intensieve samenwerking met Jacques en Rolf. Jacques met de idee'"en en leuke discussies die me gestimuleerd hebben me verder te ontwikkelen op het gebied van de MR-fysica. Met Rolf heb ik vele uren achter de scanner doorgebracht. Het was een zeer aangename samenwerking die zelfs leidde tot een vroege zaterdagochtend scansessie op de 3T in het Academisch Ziekenhuis Maastricht, mogelijk gemaakt door Walter.
Gedurende mijn AIO-periode heb ik nauw met verschillende mensen samengewerkt in de verschillende onderzoeksprojecten. Zo was er de uitnodiging om bij Bruker BioSpin in Ettlingen op bezoek te komen, om uitleg te krijgen over hun zeer verrassende oplossing van één van mijn vele problemen. Ich möchte mich beim Arno und Claudia für die Einladung bedanken, die gute Zusammenarbeit sowie die gute Versorgung während meines Aufenthalts in Ettlingen. Es freut mich dass die Zusammenarbeit mit Bram weiter in seiner Dokterarbeit verwendet werden kann.
Een andere verrassing was een zeer specifieke vraag van Guillaume en Petra die vanuit Maastricht de weg naar Eindhoven hadden gevonden. Iets waar ik trots op ben, omdat het voor ons een blijk van waardering was. Vooral de altijd relativerende Guillaume en het organisatie talent van Petra zorgde voor een zeer fijne sfeer en gezelligheid en heeft geleid tot een zeer mooie publicatie waar ik mijn bijdrage aan heb kunnen leveren. Ps:

”Petra ik heb het toch gered ondanks mijn drukke bestaan, maar ik zou het niet nog een keer zo doen!”
Een andere leuke en vruchtbare samenwerking was met Jean-Paul ,Cindy en René van het bedrijf Pie Medical die naarstig opzoek waren naar een wetenschappelijke groep die MRI beelden maakte van muizenharten. Deze samenwerking heeft mij enorm veel werk uit handen genomen en gezorgd dat grootschalige muizenstudies snel geanalyseerd konden worden. MRI beelden maken is één ding, maar het succes van het onderzoek hangt voor een groot gedeelte af van de analyse. Ik wens jullie veel succes met de verkoop en het vernieuwen van het programma en tot ziens op de volgende ISMRM.
De laatste grote samenwerking vond plaats in het laatste jaar van mijn promotie samen met de universiteit van Münster. Lars and Michael: viel Zeit und Mühe hat es gekostet, um das Experiment planen und auszuführen, aber es hat mir sehr viel Spass gemacht. Ich bin sehr stolz, dass ich die Möglichkeit gehabt habe, mit euch zusammen gearbeitet zu haben. Und ich bedanke mich bei euch auch für die Unterstützung und Hilfe whrend meiner Erkrankung. Ich hoffe auch, dass Leonie und Tessa das Project erfolgreich nach vorne bringen werden.
Ook de sfeer tussen de AIO’s was zeer goed. Het grappige was dat Willem, Henk, Anneriet, Geralda, (later Maarten en Erik) en ik totaal verschillende persoonlijkheden zijn, die ook nog heel verschillend onderzoek deden. Maar het was wel heel bijzonder om te ervaren hoe iedereen gedreven was in zijn eigen domein en de onderlinge communicatie over en weer ook zeer stimulerend was. Het is dan ook heel fijn dat we nog altijd tijdens ontmoetingen even informeren hoe het met de ander gaat en daar heel open in zijn.
Tja, als jonge ouders moet je natuurlijk informatie uitwisselen. Jeanine, ik wil je bedanken voor de gesprekken die we af en toe hadden om mijn zorgen te uiten. Ik wens je verder veel succes met het zeer goede onderzoek, wat je toch maar zo doet als wetenschapper en moeder. Via deze weg wil ik ook mijn co-promoter (Gustav) en promoter (Klaas) bedanken voor de mogelijkheden die zij mij boden. Ik heb nooit gehoord tijdens een overleg, dat een voorstel of vraag van mij niet mogelijk was of financieel niet haalbaar was. Dit is hele luxe die ik ook goed gebruikt heb. Verder heb ik geleerd dat wanneer je je open stelt en niet je problemen voor je houdt dit zeer gewaardeerd wordt en ook stimuleert in je onderzoek. Dit heeft mij zeker gevormd en ik pluk daar nu de vruchten van. Ik heb zeer goede herinneringen aan onze discussies en gesprekken. Klaas en Gustav, bedankt hiervoor en voor het corrigeren van het teksten in het proefschrift natuurlijk.
De basis voor dit proefschrift is gelegd door ontslag te nemen bij Philips en te gaan studeren aan de universiteit. In de beslissing van deze grote stap en ook gedurende de studie hebben mijn ouders mij geholpen. Ook hebben ze later tijdens mij AIO periode de zorg gedeeltelijk voor hun rekening genomen eerst voor Aimée en daarna voor Yentl. Hierdoor was het voor mij mogelijk flexibel te werken, omdat Angelique ook haar eigen werkzaamheden heeft. Ik ben dan ook zeer trots op mijn ouders en dankbaar dat zij mij deze

kansen geboden hebben.
Als allerlaatste wil ik natuurlijk Angelique bedanken voor het feit dat ze me gestimuleerd heeft in het volbrengen van mijn promotie. Ik was altijd vroeg weg was en vaak laat weer thuis en het is regelmatig voorgekomen dat ik nog op een zaterdag of zondag doorwerkte. Met twee jonge kinderen, een huishouden en eigen praktijk was het niet gemakkelijk, zeker in de afronding van mijn proefschrift. Ik weet zeker dat je trots op me bent en nu "papa niet meer achter de computer hoeft te werken om z'n boekie te schrijven" (citaat Yentl), is het tijd om samen met Aimée en Yentl een eigen stekkie te maken van ons nieuwe huis.

Publications

International refereed journals

1. **Quantification of left ventricular volumes and ejection fraction in mice using positron emission tomography in comparison to magnetic resonance imaging**
   Lars Stegger*, Edwin Heijman*, Klaus P. Schäfers, Klaas Nicolay, Michael A. Schäfers, Gustav J. Strijkers
   Reviewed Journal of Nuclear Medicine
2. **Diffusion tensor imaging of left ventricular remodeling in response to myocardial infarction in the mouse**
   Gustav J. Strijkers, Annemiek Bouts, W. Matthijs Blankesteijn, Tim H. J. M. Peeters, Anna Vilanova, Mischa C. van Prooijen, Honorius M. H. F. Sanders, Edwin Heijman and Klaas Nicolay
   NMR Biomed. 2008; 22: 1-9
3. **Smoothelin-B deficiency results in reduced arterial contractility, hypertension, and cardiac hypertrophy in mice**
   Sander S Rensen, Petra M Niessen, Jan M van Deursen, Ben J Janssen, Edwin Heijman, Evelien Hermeling, Merlijn Meens, Natascha Lie, Marion J Gijbels, Gustav J Strijkers, Pieter A Doevendans, Marten H Hofker, Jo G R De Mey, Guillaume J van Eys
   Circulation. 2008 Aug 4
4. **Evaluation of manual and automatic segmentation of the mouse heart from CINE MR images**
   Edwin Heijman, Jean-Paul Aben, Cindy Penners, Petra Niessen, René Guillaume, Guillaume van Eys, Klaas Nicolay, and Gustav J. Strijkers
   Journal of magnetic resonance imaging 27 (1), 86-93 (2008)
5. **Comparison between prospective and retrospective triggering for mouse cardiac MRI**
   Edwin Heijman, Wolter de Graaf, Petra Niessen, Arno Nauerth, Guillaume van Eys, Larry de Graaf, Klaas Nicolay, and Gustav J. Strijkers
   NMR Biomed. 20(4), 439-47 (2007)
6. **Magnetic Resonance Imaging of global and local cardiac function in the mouse**
   Edwin Heijman, Gustav J. Strijkers, Jo Habets, Ben Janssen, and Klaas Nicolay
   MAGMA 17, 170-178 (2004)

Abstracts

1. **Combined functional MRI and PET measurements in a mouse model of cardiac infarction**
   Edwin Heijman, Lars Stegger, Michael Schäfers, Klaas Nicolay, and Gustav J. Strijkers
   ISMRM 16th Scientific Meeting & Exhibition, May 2008, Toronto, Canada
2. **On the use of steady-state equations to estimate signal intensities in 2D TrueFISP imaging**
   Bram F. Coolen, Edwin Heijman, Klaas Nicolay, and Gustav J. Strijkers
   ISMRM 16th Scientific Meeting & Exhibition, May 2008, Toronto, Canada
3. **Diffusion Tensor Imaging of Left Ventricular Remodeling in Response to Myocardial Infarction in the Mouse**
   Gustav J. Strijkers, Annemiek Bouts, Edwin Heijman, Matthijs Blankesteijn, Tim H.J. Peeters, Anna Vilanova, Klaas Nicolay
   Proc. of the joint ISMRM/ESMRMB 14 (2007)
4. **Smoothelin-B Deficiency in Mice Results in Increased Thoracic Aorta Circumferential Stretch and Mild Cardiac Hypertrophy**
   Edwin Heijman, Petra Niessen, Guillaume Van Eys, Klaas Nicolay, Gustav J. Strijkers
   Proc. of the joint ISMRM/ESMRMB 14 (2007)
5. **Principal component analysis of the navigator echo signal for retrospective mouse cardiac CINE MRI**
   Edwin Heijman, Wouter Koning, Arno Nauerth, Gustav Strijkers, Klaas Nicolay
   Proc. Eur. Soc. Mag. Reson. Med. Biol. (2006)
6. **Retrospective CINE MRI of the mouse heart**
   Edwin Heijman, Wolter de Graaf, Claudia Diekmann, Arno Nauerth, Gustav Strijkers, Klaas Nicolay
   Proc. Intl. Soc. Mag. Reson. Med. 13 (2006)
7. **Self-Gated Steady-State Cardiac MRI based on Magnetization and Phase of a Slice-Refocusing Signal for Retrospective Reconstruction**
   Arno Nauerth, Edwin Heijman, Claudia Diekmann
   Proc. Intl. Soc. Mag. Reson. Med. 13 (2006)
8. **High resolution diffusion tensor imaging of adult and neonatal mouse hearts**
   Gustav J. Strijkers, Peter R. Seevinck, Anneriet M. Heemskerk, Anna Vilanova, W.M. (Mathijs) Blankesteijn, Edwin Heijman, Klaas Nicolay
   Proc. Intl. Soc. Mag. Reson. Med. 12 (2005)

9. **Improved MRI detection of low concentration paramagnetic contrast agent using steady state fully coherent gradient echo sequences**
   Edwin Heijman, Jacques den Boer, Rolf Lamerichs, Gustav J. Strijkers, Klaas Nicolay
   Proc. Intl. Soc. Mag. Reson. Med. 11 (2004)
10. **Micro-MRI of the mouse anatomy**
    Gustav J. Strijkers, Anna Vilanova i Bartroli, Willem Mulder, Edwin Heijman, Bart M. ter Haar Romeny, Klaas Nicolay
    Proc. Eur. Soc. Mag. Reson. Med. Biol. (2003)

Curriculum vitae

Edwin Heijman studied Applied Physics at the Polytechnic in Eindhoven (NL), where he graduated in 1996. During this study he also completed a half-year project in Laser Physics in Mittweida (Germany). The following three years he worked as physics assistant in the Avalanche Cold Cathode project at the Philips Research Laboratories Eindhoven (NL). From 1999 to 2002 he studied Applied Physics at the Eindhoven University of Technology, specializing in Clinical Physics. He continued with a PhD-project, entitled Cardiac MRI of the mouse heart, from 2002 to 2007, the results of which were presented at international conferences and in peer-reviewed journals. While finishing his thesis he accepted a position at Philips Research to develop pre-clinical MRI tools for measuring the effect of newly developed CNS drugs on the rat brain. This project is a collaboration between Philips and Schering-Plough.